Pseudorapidity Dependence of Directed and Elliptic Flow in Au+Au Collisions at 19.6, 62.4, 130, and 200 GeV per Nucleon Pair

by

Joshua Brian Hamblen

Submitted in Partial Fulfillment

of the

Requirements for the Degree

Doctor of Philosophy

Supervised by

Professor Steven Manly

Department of Physics and Astronomy

The College

Arts and Sciences

University of Rochester

Rochester, New York

2006

Dedicated to my parents, David and Suzanne Hamblen,

and my grandparents, Olen and Sue Cockrell,

and the late Ed and Lil Hamblen.

Curriculum Vitae

The author was born in Russellville, Arkansas, on June 18, 1977. He attended the University of Arkansas from 1995 to 1999 and graduated with a Bachelor of Science degree in physics with a minor in mathematics in 1999. He came to the University of Rochester in the Fall of 1999 and began graduate studies in physics. He received a Department of Education Graduate Assistance In Areas Of National Need fellowship from 1999 to 2002. In 2000, he received an honorable mention citation as an excellent teaching assistant from the American Association of Physics Teachers. He pursued his research in relativistic heavy-ion physics under the direction of Steve Manly and received the Master of Arts degree from the University of Rochester in 2001.

Acknowledgments

Abstract

Quantum Chromodynamics predicts that nuclear matter under extreme temperatures and/or densities will undergo a phase change from matter exhibiting hadronic degrees of freedom to that best described with partonic degrees of freedom. This high energy density regime is sought through heavy-ion collisions at the Relativistic Heavy-Ion Collider. The PHOBOS experiment measures the produced particles from these collisions in order to discern properties of the state of matter created.

One useful tool to study these collisions is the anisotropic flow of the particles, i.e., the azimuthal anisotropy of particles produced. The collective motion, quantified by flow measurements, can give hints into the degree of thermalization of the fireball created, as well as the state of matter created early in the collision. The PHOBOS experiment possesses excellent azimuthal and longitudinal coverage to measure the produced particles, which allows for the measurement of the azimuthal anisotropy over an extended range along the beam direction of the collision.

The results presented in this thesis are shown for gold-ion collisions at four different energies, covering an order of magnitude in energy. A systematic study of the directed and elliptic flow signals as a function of energy and pseudorapidity

gives insight into the evolution of the collision system as the energy is increased and as one moves away from the midrapidity region. The flow signal is seen to evolve smoothly over pseudorapidity and exhibits an energy independence over the order of magnitude range in collision energy studied.

Contents

List of Tables

List of Figures

xxiv

List of Symbols

QCD : Quantum Chromodynamics

QGP : Quark-Gluon Plasma

$RHIC$: Relativistic Heavy-Ion Collider

$\sqrt{s_{NN}}$: center-of-mass collision energy per nucleon pair

b : impact parameter

y : rapidity

y_{beam} : beam rapidity

η : pseudorapidity

θ : polar angle with respect to the collision axis

ϕ : azimuthal angle about the collision axis

p_T : transverse momentum

Ψ_R : reaction plane angle

v_1 : magnitude of directed flow

v_2 : magnitude of elliptic flow

w : acceptance and/or occupancy probability weight

Ψ_n : n^{th} order event plane angle

MC : Monte Carlo simulation

η' : $\eta - y_{beam}$

Chapter 1

QCD and Heavy-Ion Collisions

1.1   Quantum Chromodynamics

The strong nuclear force mediates interactions between the quarks and gluons thought to compose hadronic matter. The theory that describes the strong interaction is known as Quantum Chromodynamics (QCD). According to QCD, normal hadronic matter is made up of configurations of two or three quarks. The gluons act as the gauge bosons that mediate the strong interaction. Quarks carry a color charge that determines the strength of the strong force, similar to the electrical charge in the electromagnetic interaction. Gluons also carry the color charge, which allows for interactions among gluons in addition to interactions with quarks. This behavior is quite unlike the photons involved in an electromagnetic interaction, which do not carry electric charge and consequently do not interact directly with other photons.

For quarks interacting at large distances, the square of the momentum transfer (q^2) between the quarks is small, resulting in a large coupling constant between

the quarks [1]. Hence, the coupling between two quarks increases with distance in such a way that if a quark and anti-quark pair is separated, it is more energetically favorable to create a new quark and anti-quark pair out of the vacuum such that two pairs result. This is the reason that no single quarks exist in nature. This phenomenon is known as confinement.

Alternately, if the distance between a quark and anti-quark pair is decreased (equivalent to large q^2), the coupling weakens, and the quarks effectively move freely. This phenomenon is know as asymptotic freedom. A consequence of asymptotic freedom is that normal nuclear matter (protons and neutrons) will deconfine into a sea of free quarks and gluons if the energy density or temperature of the system is increased sufficiently. This sea of free quarks and gluons is known as the Quark-Gluon Plasma (QGP), a previously unobserved phase of matter. Observing and characterizing this new phase of matter would constitute a testing ground for QCD and possibly shed light on the evolution of the universe since it is believed that the early universe existed in a QGP phase for a short time.

The energy density at which a phase transition occurs between strongly and weakly coupled nuclear matter is not known analytically. However, QCD calculations performed numerically with a lattice gauge theory have been done [2]. Assuming that the state of matter is near thermodynamic equilibrium, lattice QCD can be used to calculate thermodynamical variables such as temperature, pressure and energy density, and help in determining the equation of state. Fig. 1.1 shows how the energy density varies with temperature for current lattice QCD calculations using two quark flavors, three quark flavors, and two light and one heavy quark flavors. The energy density rises quickly at the critical temperature which is calculated to be around 175 MeV for the results shown. This is indicative of a

phase transition. The curve appears to follow the Stefan-Boltzmann law, meaning

that the QGP state should behave like an ideal gas.
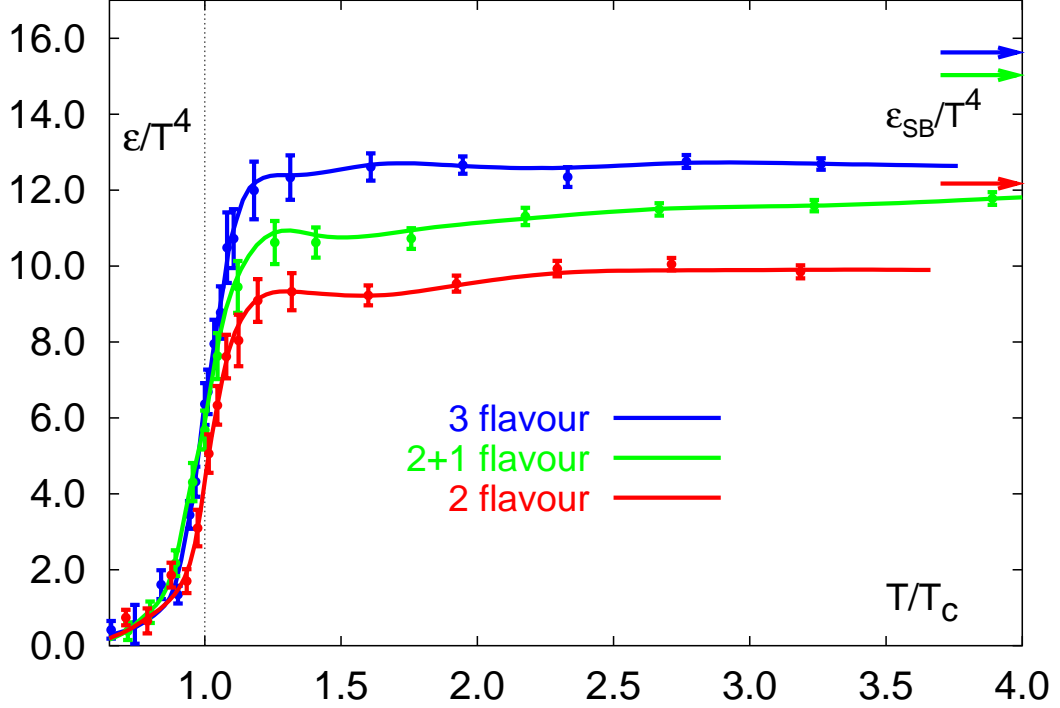
Figure 1.1: Energy density as a function of temperature for several lattice QCD calculations with differing quark flavor configurations, from reference [2].

Fig. 1.2 shows the phase diagram of nuclear matter as a function of temperature and baryon chemical potential, which varies with baryon density. The various phases of nuclear matter are illustrated qualitatively. At low temperatures and densities, quarks and gluons exist in bound states of hadrons. However, at high temperatures and densities, the hadronic matter undergoes the phase transition into partonic matter in the QGP state. This happens above some critical temperature, T_c, calculated to be about 175 MeV according to lattice QCD [2].

At the high density, low temperature extreme of the phase diagram, matter is
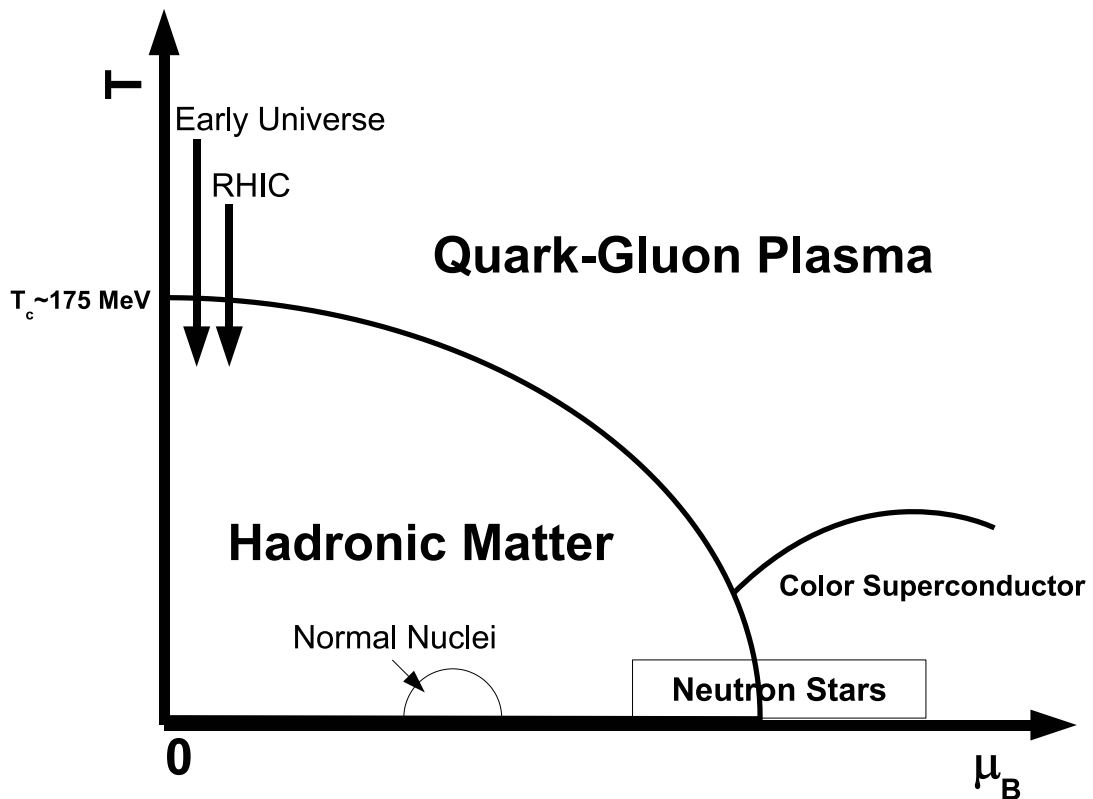
Figure 1.2: Phase diagram of nuclear matter. The arrows indicate the paths thought to be taken by the evolution of the early universe and nuclear collisions at RHIC.

thought to be in a color superconducting state [3]. The quarks form Cooper pairs due to their color charges much like electron pairs in a metallic superconductor. Due to the extreme densities necessary for its formation, this part of the phase space is out of reach of current collider experiments. However, this cold and ultra-dense state of matter may be present in the cores of neutron stars.

The QGP phase of matter may also provide insights into the role of chiral symmetry providing mass to quarks [3]. Under normal conditions, chiral symmetry is spontaneously broken through the presence of quark-antiquark condensates in

the QCD vacuum. A hadron traversing the vacuum gains much of its mass through interactions with these quark condensates. It is believed that in the QGP phase chiral symmetry is restored, meaning that the quarks interacting in the QGP phase are massless.

It is believed that the hot and dense conditions necessary to form a QGP can be created in a laboratory setting such as at the Relativistic Heavy-Ion Collider (RHIC) by colliding nuclei together at sufficient energies. A naive estimate of the energy density needed for deconfinement would be greater than the energy density of a nucleon, or around 1 GeV/fm^3.

1.2   The Relativistic Heavy-Ion Collider

The Relativistic Heavy-Ion Collider is located at Brookhaven National Laboratory (BNL) in Long Island, New York. It currently delivers the highest energy nuclear collisions in the world. The facility is capable of producing ions from A=1 (protons) to A=197 (gold) and colliding them at center-of-mass collision energies per nucleon pair ($\sqrt{s_{NN}}$) from 19.6 GeV through 200 GeV for gold-ion collisions, and up to 500 GeV for proton collisions. The 19.6 GeV lower bound energy provides a rough overlap with the top collision energy of 17.2 GeV at CERN's Super Proton Synchrotron (SPS) collider.

The collision process involves several stages of acceleration and ionization before the nuclei are fully ionized and reach the top collision energy [4]. Fig. 1.3 shows the RHIC collider and its accelerator components. In the case of Au+Au collisions, the ions are first created in a pulsed sputter ion source in the charge state -1 and then accelerated electrostatically via Tandem Van de Graaff acceler-

ators. The ions pass through stripping foils and leave the Tandem with a collision energy of 1 MeV/u and a charge state of +32. From there the ions enter the Booster synchrotron where they are accelerated to 95 MeV/u. As they exit the Booster a foil strips the ions of all but two of their remaining electrons.

The ions next enter the Alternating Gradient Synchrotron (AGS) where they are accelerated to 8.86 GeV/u. Upon exiting the AGS, the ions pass through a final foil and are stripped of their last two electrons to achieve the +79 charge state. The ions travel down the AGS to RHIC (AtR) beam line where they are injected into the RHIC accelerator. RHIC consists of two countercirculating superconducting magnet rings, 3.8 km in circumference, that intersect in 6 places to provide for collisions. The magnets are ramped up to their top currents over a period of about two minutes during which the ions are accelerated to the top collision energy. The ions travel in bunches within the rings. Typically 56 bunches are present in each ring during RHIC running. Each bunch carries $\sim 10^9$ ions, and the expected luminosity for an average running period of 10 hours at 100 GeV/u is $\sim 2 \times 10^{26} cm^{-2} s^{-1}$ [4].

The first collisions at RHIC occurred in 2000, and since then, RHIC has produced collisions over a wide variety of systems and energies. The PHOBOS experiment took data from 2000 to 2005 and recorded collisions of Au+Au at $\sqrt{s_{NN}}$=19.6, 56, 62.4, 130, and 200 GeV. There were also data sets taken of deuteron-gold collisions (d+Au) at $\sqrt{s_{NN}}$= 200 GeV, copper-copper collisions (Cu+Cu) at $\sqrt{s_{NN}}$= 22.4, 62.4, and 200 GeV, and polarized proton (p+p) collisions at 200 and 410 GeV.
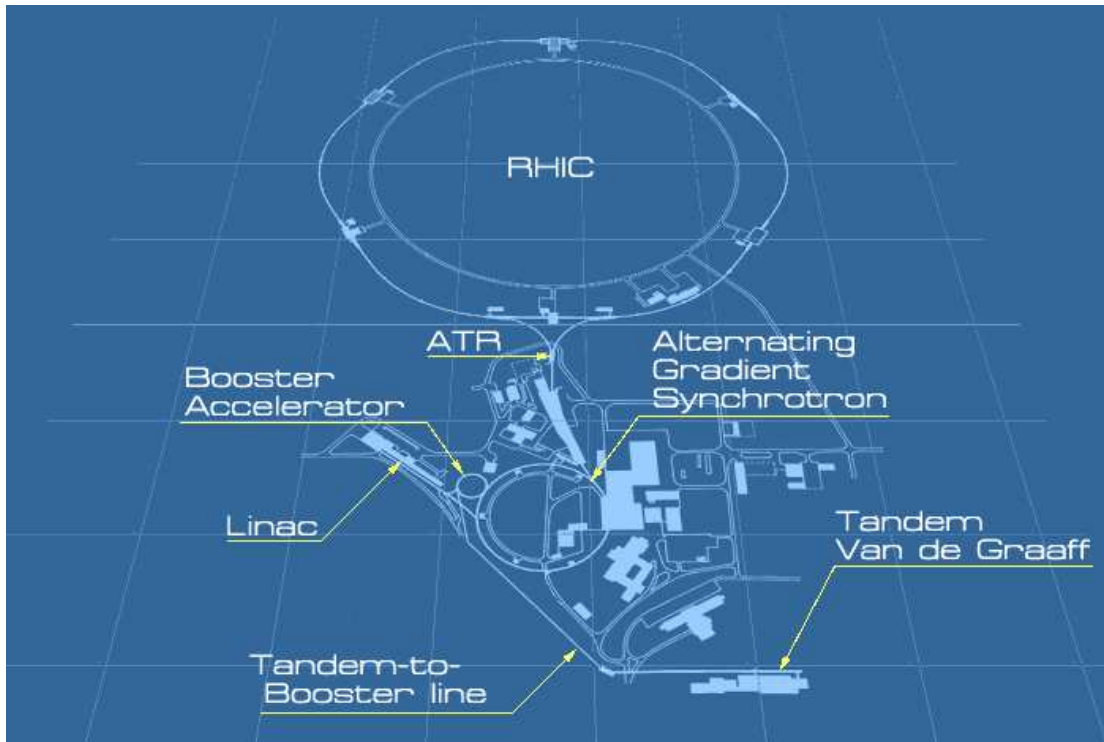
Figure 1.3: The RHIC accelerator complex at Brookhaven National Laboratory. From reference [5].

1.3 RHIC Experiments

The RHIC facility features four experiments that study the heavy-ion collisions: PHOBOS, BRAHMS, STAR, and PHENIX. All four detectors possess unique capabilities to measure specific aspects of the collision while at the same time providing complimentary measurements of several variables. Fig. 1.4 shows the locations of the experiments on the RHIC ring. The ring is often viewed as a clock face, with the topmost point of Fig. 1.4 being at the 12 o'clock position. Accordingly, Brahms is at 2 o'clock, STAR at 6 o'clock, PHENIX at 8 o'clock, and PHOBOS is at 10 o'clock.
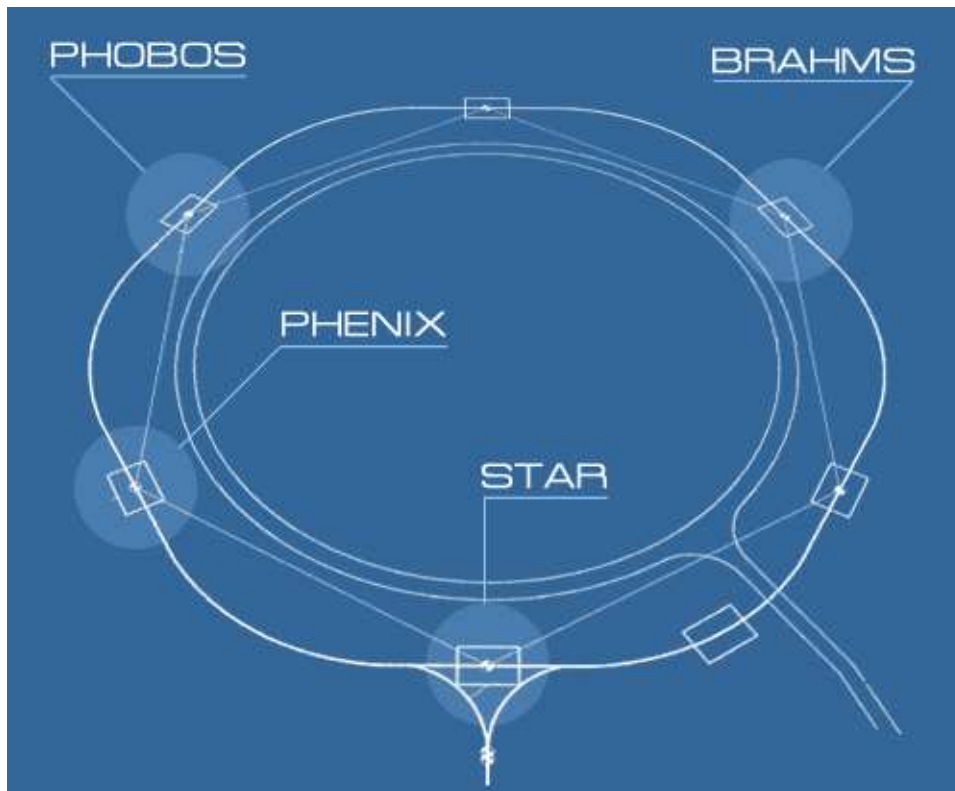
Figure 1.4: The locations of the four experiments on the RHIC ring. From reference [5].

1.3.1 PHOBOS

PHOBOS is one of the smaller experiments at RHIC. It consists of a silicon multiplicity array that provides good azimuthal and longitudinal coverage with respect to the beam axis. There is also a silicon spectrometer that provides particle identification and momentum measurements for about 1% of the produced particles. In addition there is an array of plastic scintillator detectors for triggering, as well as two time-of-flight walls. The PHOBOS detector is discussed in detail in Ch. 3.

1.3.2 BRAHMS

The BRAHMS (Broad RAnge Hadron Magnetic Spectrometers) detector is the other small experiment at the RHIC complex. It consists of two spectrometer arms, one in the midrapidity region and the other in the forward region. BRAHMS possesses the largest rapidity range for particle identification of all the RHIC experiments because both arms can be rotated along the polar angle with respect to the beam axis to provide additional rapidity coverage. The specialty of BRAHMS
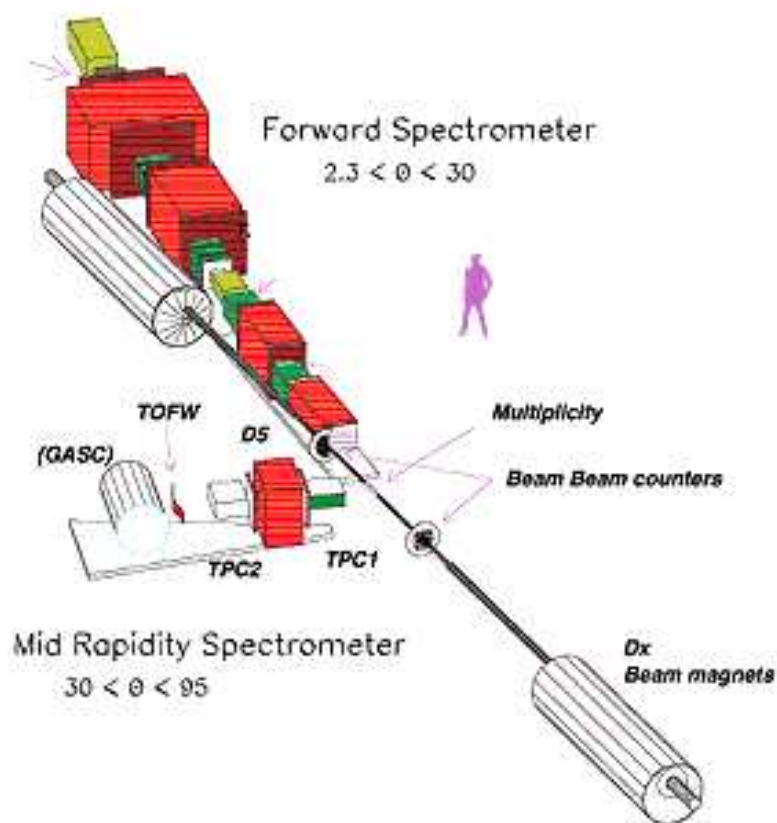
Figure 1.5: The BRAHMS detector. From reference [5].

is to use the spectrometer arms to measure wide ranging rapidity distributions of identified particles, specifically the net-proton content of the collision zone as a

function of rapidity. BRAHMS also has beam-beam counters, a multiplicity ar-
ray, and zero-degree calorimeters (ZDCs) which are common triggering detectors
for all four experiments. Fig. 1.5 shows the BRAHMS detector with the major
subdetectors labeled.

1.3.3 STAR

The Solenoid Tracker at RHIC (STAR) is one of the large experiments at RHIC.
The main detector is a 4π time-projection chamber (TPC) that sits in a magnetic
field and provides particle identification and tracking of the detected particles
in the central rapidity region. Two end cap forward TPCs provide tracking in
the forward rapidity region. STAR also contains a silicon vertex tracker, electro-
magnetic calorimeters, and time-of-flight detectors. Fig. 1.6 illustrates the STAR
detector and its components.
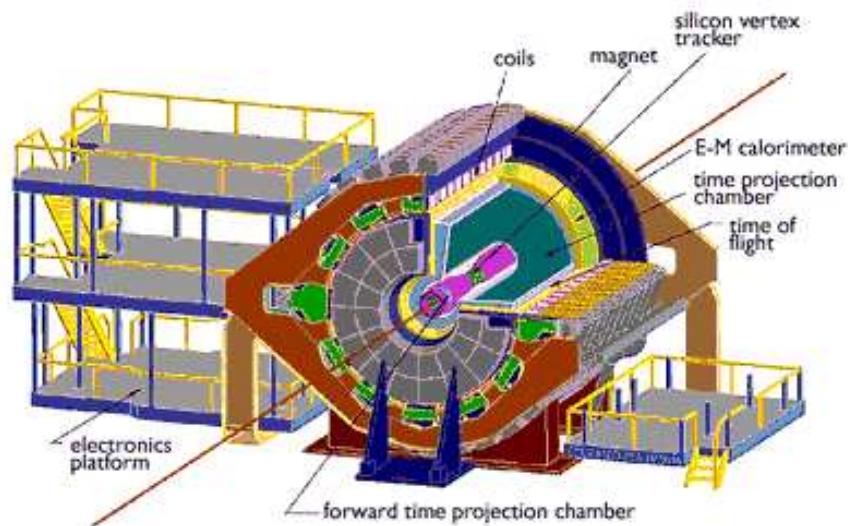
Figure 1.6: The STAR detector. From reference [5].

1.3.4   PHENIX

The Pioneering High Energy Nuclear Interaction eXperiment (PHENIX) is the other large experiment at RHIC. Fig. 1.7 shows the PHENIX detector and its major components. The detector is geared toward measuring direct probes of the collision such as photons and leptons that do not interact via the strong nuclear force. PHENIX consists of two arms in the central rapidity region that sit in a magnetic field and contain a drift chamber, pad chambers, ring imaging Cherenkov detector, time expansion chamber, time-of-flight detector, and electromagnetic calorimeter. Forward muon arms also sit in a magnetic field and contain muon tracking chambers and muon identifiers.
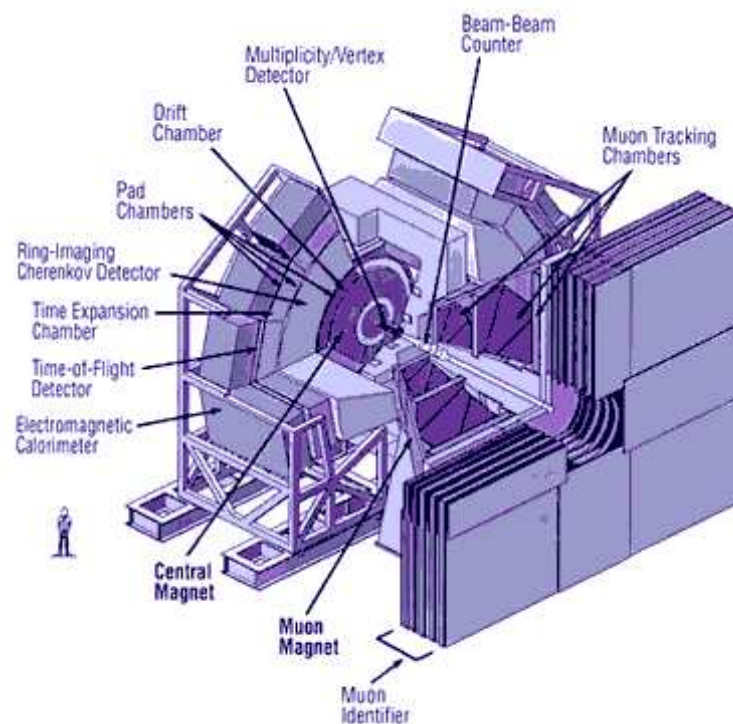
Figure 1.7: The PHENIX detector. From reference [5].

1.4   Properties of the Collision

When two nuclei collide at RHIC, they appear in the center-of-mass frame as extremely flat discs due to Lorentz contraction. The nuclei largely pass through each other, and about 75% of the total energy [6] is deposited into the vacuum where the collision occurs. This highly energized vacuum is where partons are first created. The partons interact with themselves, potentially in the QGP phase, until the system expands and cools, and hadronization occurs at the critical temperature. At this point the partons become bound inside hadrons, and inelastic collisions occur between particles. After a brief time ($\sim$5 fm/c), the matter cools enough that inelastic collisions cease, and the yield of each particle type is fixed. This is known as chemical freezeout. After further cooling, the particles cease elastic col-
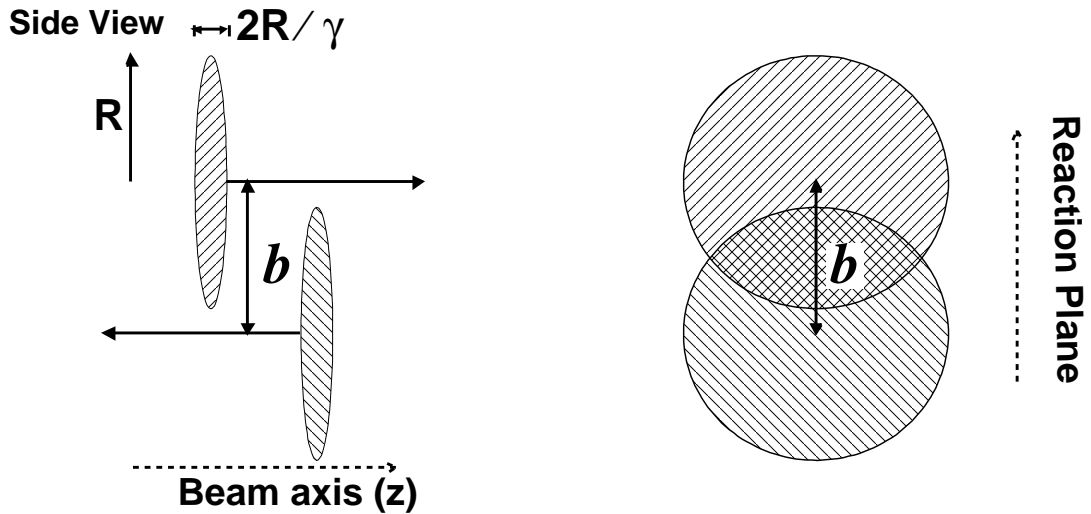
Figure 1.8: Diagram of the collision, from reference [6]. The left panel shows the contracted nuclei in a non-central collision. R is the radius of the nucleus and b is the impact parameter or distance between the centers of the nuclei. The nucleons that lie inside (outside) the overlapping region are called participants (spectators). The right panel shows the collision with the beam axis going into the page. The reaction plane is also labeled.

lisions at a point known as thermal freezeout and stream away from the collision point.

The geometry of the collision can be described using the impact parameter, b, or the distance between the centers of the nuclei. The impact parameter gives an indication of the centrality of the collision. A small impact parameter is deemed a central collision, while a collision with a large impact parameter is known as a peripheral collision. Since the impact parameter cannot be determined experimentally, the centrality of the collision is inferred through other methods. These are discussed in Ch. 3.

The nucleons that overlap and participate in the collision are called participants. The nucleons that fall outside the overlap regions are dubbed spectators. The plane defined by the direction of the impact parameter vector connecting the centers of the two nuclei and the collision axis is known as the reaction plane. Fig. 1.8 illustrates these collision properties.

The produced particles are studied in a variety of ways. One of the most important variables describing a particle is its rapidity, defined as

$$y = \frac{1}{2} \; ln \left(\frac{E + p_z}{E - p_z} \right),$$
(1.1)

where E is the total energy and p_z is the momentum component in the direction of the beam. Rapidity is useful because Lorentz transformations from one frame to another are simply additive in rapidity for particles that differ by velocity along the beam. For example, a variable plotted as a function of rapidity can be shifted to the frame of reference of one of the colliding nuclei by subtracting the beam

rapidity from the variable under study. Beam rapidity is given as

$$y_{beam} = \frac{1}{2} \, ln \left(\frac{E + p}{E - p} \right),$$

(1.2)

where E and p are the energy and momentum of the beam. The shape of the distribution does not change since it is merely shifted along the rapidity axis.

It is difficult to find experimentally the rapidity of a detected particle since it involves identifying the particle and finding its momentum. It is easier to determine the pseudorapidity, η, instead of rapidity:

$$\eta = -ln(tan(\theta/2)),$$

(1.3)

where θ is the polar angle with respect to the beam axis. Pseudorapidity is a close approximation to rapidity for particles whose velocity is close to the speed of light, where their total momentum is large compared to their mass. In RHIC collisions, the produced particles are mostly pions whose momentum are around a few hundred MeV/c, so pseudorapidity is a reasonable approximation to rapidity in most instances.

1.5   Experimental Observables and Possible Signatures for the QGP

There are many variables studied in heavy-ion collisions that give us a better understanding of the medium created. These include measurements that describe the bulk properties of the medium, such as charged particle multiplicity, trans-

verse momentum spectra, particle species ratios, and anisotropic flow. These help determine the degree of thermalization and energy density achieved in the medium.

Additionally, there are several proposed specific experimental signatures that could potentially indicate the creation of the QGP. One is the quenching of high transverse momentum (p_T) jet production. Jets formed from the initial hard scattering of nucleon constituents will lose significant amounts of energy as they traverse the dense colored medium, leading to a suppression of observed back-to-back azimuthal jets [7]. Another is the suppression of J/Ψ production. The J/Ψ is a meson composed of a charm and an anti-charm quark. In a QGP the J/Ψ will experience Debye screening of the color charge such that the formation of $c\bar{c}$ pairs will be suppressed [8]. In addition, it has been hypothesized that the formation of a QGP might lead to an enhancement of strange particle production [9] as well as fluctuations of measured variables as the medium crosses from the QGP to hadronic matter [10].

1.6 Flow as a Probe of Heavy-Ion Collisions

One of the most interesting properties of the collision that can be measured through experimental techniques is the anisotropic flow. Flow is defined in terms of azimuthal correlations of the produced particles with respect to the reaction plane. Flow is typically quantified by the Fourier coefficients of the azimuthal distribution of the produced particles. The first and second order coefficients are dubbed the directed and elliptic flow, respectively, and will be the focus of this thesis.

The flow signal is generated from the initial spatial anisotropy of the overlapping region of non-central collisions as shown in the right panel of Fig. 1.8. With significant interactions of the produced particles within this region, pressure gradients will form, resulting in particles streaming out in greater numbers and with a higher momentum in the direction of the reaction plane. Since the produced particles must interact with themselves to generate a signal, flow measurements provide information on the degree of thermalization of the source. Also, since the anisotropy becomes symmetric as the source expands due to the asymmetry in the pressure gradients, a flow signal necessarily provides information on the very early times of the collision when the energy density is largest. Given the measured flow signals at RHIC, the current estimate on the timescale for equilibration in the collision is less than 2 fm/c [11], so the pressure buildup occurs very early in the collision process.

1.7 Hydrodynamics and Flow

The magnitude of the flow signal can also help distinguish between a strongly interacting or weakly interacting system of quarks and gluons in the QGP state. Before RHIC was operational, much of the community expected a QGP composed of weakly interacting quarks and gluons, much like an ideal gas. Interestingly, RHIC results have shown that the system formed is very strongly interacting, much like an ideal fluid. At RHIC energies, the collective flow measurements in heavy-ion collisions at midrapidity are in good agreement with hydrodynamical models. Such hydrodynamical models can be used to calculate the final state distribution of particles, based on the initial source shape of the medium created.

The agreement between hydrodynamic calculations and experimental flow results also help determine the extent of the fluid behavior of the created medium. This means that the new state of matter behaves much like a fluid of partons that strongly interact with themselves. This is different from the pre-RHIC notion that the quark-gluon plasma will behave like an ideal gas with a rather small flow signal.

Early hydrodynamical models assumed longitudinal boost invariance and used two-dimensional calculations in the transverse plane to make predictions. This simplified the calculations significantly. The predictions are in good agreement with the measured flow in the midrapidity region for central collisions and low p_T particles [13, 14], but this approach does not work when studying the collisions away from midrapidity. The PHOBOS experiment produced the first elliptic flow results as a function of pseudorapidity at RHIC [15]. The results were unexpected. The elliptic flow showed an undeniable falloff as a function of η, which is in direct contrast to the longitudinal boost invariant assumption. These results have encouraged theorists to perform full 3D calculations in order to reproduce what is shown in the data [16]. Fig. 1.9 shows an early 3-dimensional hydrodynamic calculation and the first PHOBOS 130 GeV elliptic flow result. There is good agreement at midrapidity, but not at larger $|\eta|$. The behavior of elliptic flow as a function of pseudorapidity has also spurred theorists to think of reasons for the dropoff, such as incomplete thermalization away from midrapidity and the effects of viscosity in the matter created [17, 18].

As illustrated by these early results, PHOBOS possesses excellent capabilities to explore the longitudinal dependence of flow. Since then, RHIC has produced collision energies that span an order of magnitude for Au+Au. This provides
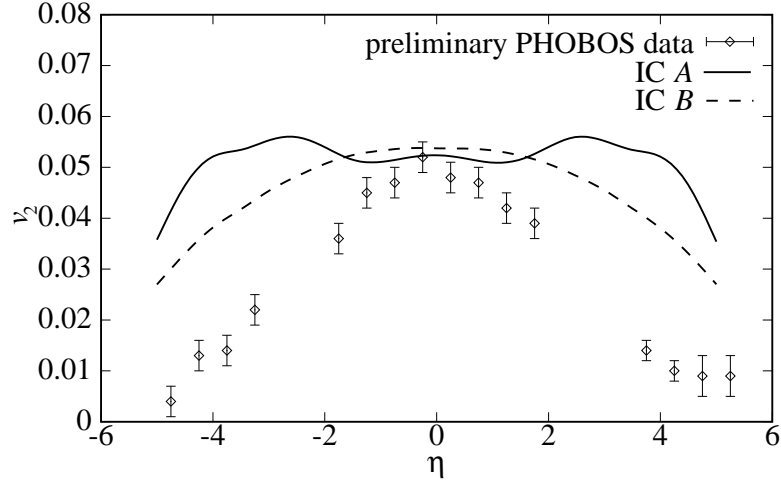
Figure 1.9: Three-dimensional hydrodynamical calculations of elliptic flow compared to an early PHOBOS result at 130 GeV. From reference [16].

the opportunity to understand the state of matter created away from midrapidity and at lower energies. Hydrodynamical calculations indicate that a very strongly interacting, fluid-like state of matter exists at midrapidity in 200 GeV Au+Au collisions, so it is interesting to study what is going on at higher $|\eta|$ and lower energy. A systematic study of the first and second flow harmonics as a function of energy and pseudorapidity provides an important constraint on the collision evolution over this energy range. In addition, it is important to see if the flow variables exhibit any longitudinal scaling as was exhibited in the pseudorapidity density of the produced charged particles [19]. This would further explore any differences in the particle production mechanisms as a function of energy and rapidity.

Chapter 2

Flow Theory and Analysis Techniques

2.1 How Flow Is Produced in Heavy-Ion Collisions

When two nuclei collide with non-zero impact parameter, the initial spatial aniso-
tropy of the overlapping region leads to a momentum anisotropy in the final state.
The pressure gradients, built up as a result of the initial overlap, are greatest in
the direction of the reaction plane, which is defined by the plane that contains the
collision axis and impact parameter direction. With significant reinteraction of
the produced particles in the collision, the produced particles will tend to stream
out in the direction of the reaction plane at RHIC collision energies.[1] This is
known as "in-plane" flow. Fig. 2.1 illustrates a typical heavy-ion collision when

---

[1]The azimuthally symmetric expansion of the collision system in the transverse plane is often
referred to as radial flow.

viewed in the transverse plane, with the reaction plane and a produced particle labelled.
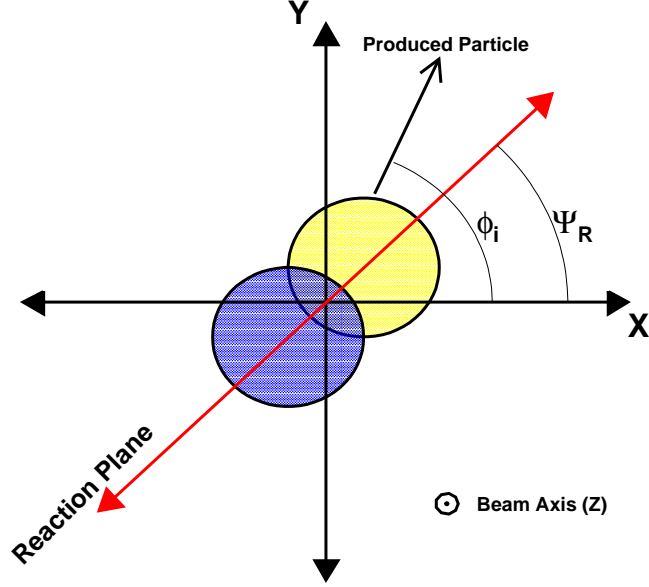
Figure 2.1: Schematic of a collision between two heavy ions. The reaction plane is shown, as well as the azimuthal coordinate, ϕ_i, of a produced particle.

2.2 Fourier Decomposition of Particle Production

Flow can be quantified in heavy-ion collisions by studying the Fourier decomposition of the azimuthal angular dependence of the particles produced. The formalism for this analysis is outlined in [20]. The particle distribution is given as

$$\frac{dN}{d(\phi - \Psi_R)} = \frac{1}{2\pi}(1 + \sum_{n=1}^{\infty} 2\mathrm{v}_n \cos[n(\phi - \Psi_R)]), \qquad (2.1)$$

where Ψ_R is the reaction plane angle, and ϕ is the azimuthal angle of the produced particles. The v_n coefficients are defined as

$$v_n = \langle cos\ n(\phi_i - \Psi_R) \rangle, \tag{2.2}$$

where the brackets denote averaging over all particles in all events.

The first harmonic coefficient, v_1, is known as the directed flow and reflects an overall shift in one direction of the produced particles in the transverse plane. Momentum is conserved, so this shift is in opposite directions on the two sides of midrapidity in the longitudinal direction. For the number distribution of the produced particles, the directed flow yields $\langle p_{x,i}/p_{T,i} \rangle$, where $p_{T,i}$ is the transverse momentum of the ith particle, and $p_{x,i}$ is the transverse momentum component of the ith particle in the reaction plane.[2]

The second harmonic coefficient, v_2, is known as the elliptic flow, since the second order particle distribution represents an ellipse. The number distribution is $\langle (p_{x,i}/p_{T,i})^2 - (p_{y,i}/p_{T,i})^2 \rangle$ for elliptic flow, where $p_{y,i}$ represents the transverse momentum component of the ith particle perpendicular to the reaction plane.

2.3   Measuring Fourier Harmonics with Event Planes

The most common way to measure the Fourier coefficients is with the event plane technique [20]. Since the reaction plane cannot be determined exactly through

---

[2]Given that each particle, i, has transverse momentum $p_{T,i}$ and makes an angle $\phi_i - \Psi_R$ with respect to the reaction plane, the directed flow averaged over all particles is $v_1 = \langle cos\ (\phi - \Psi_R) \rangle = \langle p_x/p_T \rangle$. The v_2 relation is similar.

experimental methods, an estimated reaction plane, known as the event plane, is used. Once the event plane is determined using the detected particles in an event, the flow is determined by correlating the azimuthal coordinates of the particles with this event plane and extracting the Fourier coefficients that best describe the pattern. In addition, a correction is made due to the finite resolution of the event plane with respect to the reaction plane.

The event plane is reconstructed from the nth order event flow vector [21], defined as

$$\overrightarrow{\mathbf{Q_n}} = \{X_n, Y_n\}, \tag{2.3}$$

where the index n refers to the nth component of the Fourier series. Given as a function of the azimuthal coordinates of the produced particles in the transverse plane of the collision, the flow vector components are:

$$\overrightarrow{\mathbf{X_n}} = Q_n cos(n\Psi_n) = \sum_i w_i cos(n\phi_i), \tag{2.4}$$

and

$$\overrightarrow{\mathbf{Y_n}} = Q_n sin(n\Psi_n) = \sum_i w_i sin(n\phi_i). \tag{2.5}$$

ϕ_i is the azimuthal angle of the ith hit and w_i is a weight assigned to the ith detector pixel. The weights make up for inefficiencies and azimuthal phase space variations in the detector. The weights are discussed in more detail in Ch. 4. The detector region where an event plane is determined is called a subevent.

Given these relations, the event plane angle, Ψ_n, can be found by solving

Eqs. 2.4 and 2.5 for Ψ_n from the components of the flow vector according to

$$\Psi_n = tan^{-1}\left(\frac{Y_n}{X_n}\right) = \frac{1}{n}tan^{-1}\left(\frac{\sum w_i sin(n\phi_i)}{\sum w_i cos(n\phi_i)}\right). \tag{2.6}$$

Notice that an event plane angle, Ψ_n, can be found for each harmonic, n, of the azimuthal distribution, and that the angular range of Ψ_n is $0 \leq \phi \leq 2\pi/n$. Each nth order event plane angle represents a similar angular estimate of the true reaction plane angle, but modulated by a phase of $2\pi/n$.

The observed flow signal, v_n^{obs}, using the nth harmonic event plane, Ψ_n, is then given as

$$v_n^{obs} = \langle cos\ n(\phi_i - \Psi_n)\rangle \tag{2.7}$$

where the brackets denote average over all hits in all events.

The observed flow value is corrected by the reaction plane resolution, $\langle cos\ n(\Psi_n - \Psi_R)\rangle$, to give the flow signal with respect to the real reaction plane

$$v_n = v_n^{obs}/\langle cos\ n(\Psi_n - \Psi_R)\rangle. \tag{2.8}$$

The reaction plane resolution is discussed in Section 2.5.

2.4 Determining Event Planes

In the PHOBOS hit-based flow analysis, hits from a particular subevent region are used to form a reconstructed event plane angle, and then the event plane is correlated with hits from another detector section to measure the flow signal. At least two subevents must be used in each event so that the hits under study do not

belong to the subevent with which they are correlated. Otherwise, the analysis suffers from autocorrelations that can induce a signal similar to flow. The two subevents are also correlated with each other to provide the reaction plane resolution correction. In order to determine a good estimate of the reaction plane resolution using this technique, the subevent windows must be of approximately equal multiplicity and cover similar pseudorapidity ranges. Generally, equal sections in the forward and backward pseudorapidity hemispheres are used as the subevents.

2.5 Reaction Plane Resolution

A correction to the observed flow signal is needed since the event plane angle will not point in the exact direction of the reaction plane due to finite resolution. The correction is found by calculating an event plane angle in two distinct subevent regions, a and b, in every event. The relation between the two event plane angles, Ψ_n^a and Ψ_n^b, and the reaction plane resolution, $\langle cos\, n(\Psi_n^{(a\ or\ b)} - \Psi_R)\rangle$, is then

$$\langle cos(n(\Psi_n^a - \Psi_n^b))\rangle = \langle cos(n(\Psi_n^a - \Psi_R))\rangle \langle cos(n(\Psi_n^b - \Psi_R))\rangle \qquad (2.9)$$

where the angled brackets denote averaging over all events, and any correlations not due to flow are assumed to be negligible. When the two distinct subevents are chosen such that they have similar multiplicity and flow levels, Eq. 2.9 gives the resolution for each subevent as

$$\langle cos(n(\Psi_n^a - \Psi_R))\rangle = \langle cos(n(\Psi_n^b - \Psi_R))\rangle = \sqrt{\langle cos(n(\Psi_n^a - \Psi_n^b))\rangle}. \qquad (2.10)$$

Using this result, the resolution-corrected flow given in Eq. 2.8 becomes

$$v_n = \frac{v_n^{obs}}{\sqrt{\langle cos\ n(\Psi_n^a - \Psi_n^b)\rangle}}. \tag{2.11}$$

2.6 Elliptic Flow Analysis

Given the previous discussion, in order to measure the elliptic flow parameter, v_2, one uses the n=2 case for Eq. 2.11, which simply becomes

$$v_2 = \frac{v_2^{obs}}{\sqrt{\langle cos\ 2(\Psi_2^a - \Psi_2^b)\rangle}}. \tag{2.12}$$

As mentioned before, two separate subevent regions, a and b, are used to find the event plane angles Ψ_2^a and Ψ_2^b. The observed flow signal, v_2^{obs}, from Eq. 2.7 is then $\langle cos\ 2(\phi_i - \Psi_2^a)\rangle$ for hits not in the "a" subevent, and $\langle cos\ 2(\phi_i - \Psi_2^b)\rangle$ for hits not in the "b" subevent. This is done to avoid autocorrelations. The actual subevents used for the results shown in this thesis are described in Ch. 5.

2.7 Directed Flow Analysis

In the directed flow analysis, finding first harmonic event planes in forward or backward subevents is particularly susceptible to non-flow correlations arising from momentum conservation [22]. To overcome this, the subevents are chosen in symmetric windows of pseudorapidity. That is to say, each subevent is made up of two detector sections that are symmetric about $\eta = 0$. For this reason, this analysis method is dubbed the "symmetric subevent" analysis. Thus, any fluctuation

in the negative half of the subevent is cancelled by an equal and opposite recoil in the positive half. Elliptic flow and all other even harmonics are not susceptible to the momentum conservation non-flow correlations. The resolution correction for an event plane made from a combined forward and backward subevent, Ψ_1^{a+b}, is given as

$$\langle cos(\Psi_1^{a+b} - \Psi_R) \rangle = \sqrt{2} \langle cos(\Psi_1^a - \Psi_R) \rangle = \sqrt{2 \langle cos(\Psi_1^a - \Psi_1^b) \rangle}. \qquad (2.13)$$

The actual subevents used for the results shown in this thesis are described in Ch. 6. For the half of the subevent in the negative η hemisphere, the ϕ coordinates are shifted by 180 degrees so that the event plane points in the same direction as that found in the positive half. This is accomplished by multiplying the weights in the negative hemisphere by a factor of -1. Otherwise, the contributions from both hemispheres would cancel out since they are pointing in back-to-back directions.

Though each subevent in the directed flow analysis is made up of parts that are symmetric with respect to $\eta = 0$, the two subevents (e.g., Ψ_1^{a+b} and Ψ_1^{c+d}) necessarily cover different ranges of pseudorapidity. This means the two subevents are no longer similar. So, rather than correlating one subevent against the other to determine the subevent resolution, the similar η-symmetric halves of each subevent are correlated with each other to determine the reaction plane resolution of each subevent separately (e.g., Ψ_1^a and Ψ_1^b, as shown in Eq. 2.13, or a similar correlation using Ψ_1^c and Ψ_1^d). Unfortunately, this means that the detector sections correlated against one another for the resolution correction are each asymmetric about $\eta = 0$ and are thus susceptible to a potential non-flow correlation arising from momentum conservation. Fortunately, this non-flow correlation does not appear to be

significant in the final directed flow results. This is indicated, in part, by the fact that the results do not have the discontinuity at $\eta=0$ that generally arises from a momentum conservation non-flow correlation, as well as the fact that the results are consistent with those determined using a different analysis that is thought to be immune to non-flow correlations. This additional analysis, called the mixed harmonic analysis, is described below.

The mixed harmonic flow analysis method seeks to minimize non-flow correlations by analyzing azimuthal correlations using both the first and second harmonic event planes. The rationale for this method begins with the fact that the directed flow signal is expected to be in the reaction plane. Since non-flow correlations will be found in equal amounts both in and out of the reaction plane, the non-flow correlations perpendicular to the reaction plane can be subtracted from the signal that is in the reaction plane to yield only the directed flow signal. Since elliptic flow is strong in the heavy-ion collisions at RHIC, the second harmonic event plane, Ψ_2, is used as a reasonable estimate of the reaction plane.

The mixed harmonic event plane analysis was first proposed in [23] and used on RHIC collisions by the STAR collaboration [24]. To obtain the equation for v_1, one first begins with the relation

$$
\begin{aligned}
\langle cos(\phi - \Psi_2)cos(\Psi_1 - \Psi_2) \quad &- \quad sin(\phi - \Psi_2)sin(\Psi_1 - \Psi_2)\rangle \\
&= \quad \langle cos((\phi - \Psi_2) + (\Psi_1 - \Psi_2)\rangle \\
&= \quad \langle cos(\phi + \Psi_1 - 2\Psi_2)\rangle. \qquad (2.14)
\end{aligned}
$$

Using the angle-sum trigonometric identity and ignoring the negligible sine terms

yields

$$
\begin{aligned}
\langle cos(\phi \quad + \quad \Psi_1 - 2\Psi_2)\rangle \\
&= \langle cos[(\phi - \Psi_R) + (\Psi_1 - \Psi_R) - 2(\Psi_2 - \Psi_R)]\rangle \\
&= \langle cos(\phi - \Psi_R)cos(\Psi_1 - \Psi_R)cos[2(\Psi_2 - \Psi_R)]\rangle \\
&= \langle cos(\phi - \Psi_R)\rangle\langle cos(\Psi_1 - \Psi_R)\rangle\langle cos[2(\Psi_2 - \Psi_R)]\rangle \\
&\equiv v_1 Res(\Psi_1)Res(\Psi_2).
\end{aligned}
\tag{2.15}
$$

The factorization in the fourth line of Eq. 2.15 is valid since the three cosine factors are statistically independent. The resolution of the second order event plane, $Res(\Psi_2)$, is given by Eq. 2.10. The first order event plane resolution, $Res(\Psi_1)$ is given by the following expressions:

$$
\begin{aligned}
\langle cos[2(\Psi_1 - \Psi_2)]\rangle &= \langle cos[2(\Psi_1 - \Psi_R) - 2(\Psi_2 - \Psi_R)]\rangle \\
&= \langle cos[2(\Psi_1 - \Psi_R)]cos[2(\Psi_2 - \Psi_R)]\rangle \\
&= \langle cos^2(\Psi_1 - \Psi_R)cos[2(\Psi_2 - \Psi_R)]\rangle \\
&= \langle cos(\Psi_1 - \Psi_R)\rangle^2\langle cos[2(\Psi_2 - \Psi_R)]\rangle \\
&= Res^2(\Psi_1)Res(\Psi_2),
\end{aligned}
\tag{2.16}
$$

or

$$
\sqrt{\langle cos[2(\Psi_1 - \Psi_2)]\rangle Res(\Psi_2)} = Res(\Psi_1)Res(\Psi_2).
\tag{2.17}
$$

Notice that the the negligible sine term in the identity $cos[2(\Psi_1 - \Psi_R)] = cos^2(\Psi_1 - \Psi_R) - sin^2(\Psi_1 - \Psi_R)$ is omitted between the second and third line of Eq. 2.16.

Combining Eqs. 2.15 and 2.17 gives

$$v_1\{\Psi_1, \Psi_2\} = \frac{\langle cos(\phi + \Psi_1 - 2\Psi_2)\rangle}{\sqrt{\langle cos[2(\Psi_1 - \Psi_2)]\rangle Res(\Psi_2)}}. \tag{2.18}$$

To optimize the analysis, the particle under study, ϕ^a, should be contained in a region (a) that is separate from the subevent regions where Ψ_1^b and Ψ_2^c are found. The region where Ψ_2 is found is chosen to be where v_2 is strong. Two subevent regions are needed to find both Ψ_1 and Ψ_2 in any given event to ensure that the particle under study does not belong to the Ψ_1 or Ψ_2 subevent and that the Ψ_1 and Ψ_2 subevents do not overlap. Two η-symmetric subevents are used to find Ψ_1, and two η-asymmetric subevents (as used in the elliptic flow analysis) are used to find Ψ_2. The actual measured directed flow takes the form

$$v_1\{\Psi_1, \Psi_2\} = \frac{\langle cos(\phi^a + \Psi_1^b - 2\Psi_2^c)\rangle}{\sqrt{\langle cos(\Psi_1^a + \Psi_1^b - 2\Psi_2^c)\rangle Res(\Psi_2^c)}}. \tag{2.19}$$

The detailed description of the mixed harmonic subevents is given in Ch. 6.

Chapter 3

The PHOBOS Detector

3.1   Detector Overview

The PHOBOS detector [25] is designed to provide a global view of the thousands of particles produced in each heavy-ion collision. The apparatus is made up of several different subsystems that each measure different aspects of the collision. The detector is shown in Fig. 3.1.

The PHOBOS interaction region features a beam pipe made of beryllium that is 12 m long and 76 mm in diameter. The beam pipe has a thickness of roughly 1 mm. The low-Z material minimizes the production of background particles as well as multiple scattering of the produced particles as they traverse the beam pipe.

The detector features several highly segmented silicon pad detectors [26]. The most significant of these detectors in terms of pseudorapidity coverage is the multiplicity array which consists of the Octagon and Ring subdetectors. The multiplicity detector measures the charged particle production event-by-event over
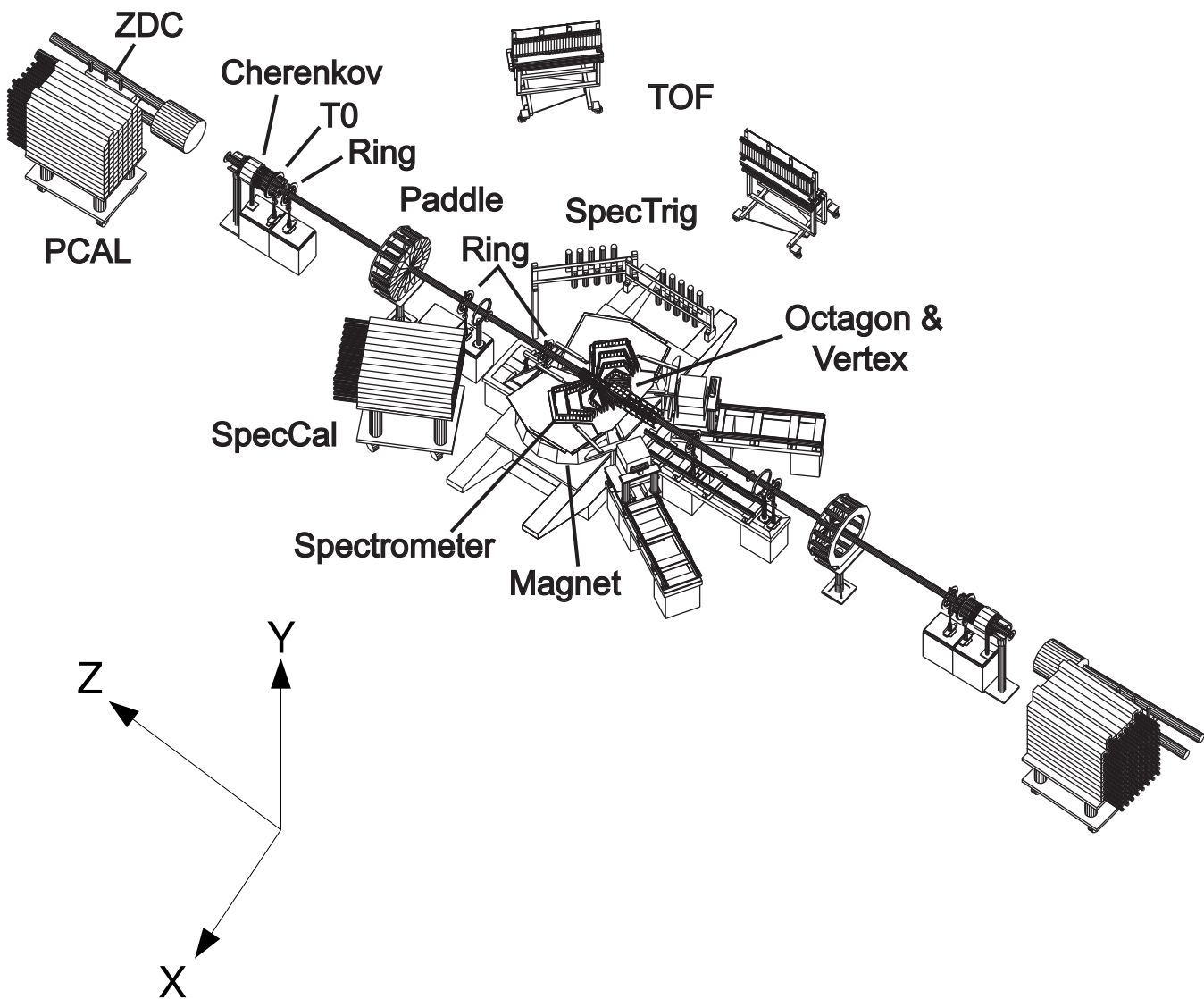
Figure 3.1: The PHOBOS detector as it appeared during the 2004 running period.

essentially the full solid angle in the range $|\eta| \leq 5.4$. The Vertex detector is another silicon based detector that allows for determination of the collision point. The two armed silicon Spectrometer sits in a magnetic field and provides momentum determination as well as particle identification for charged particles traversing that part of the detector. Two Time-of-Flight (ToF) walls also provide particle identification over a larger momentum range. The Spectrometer Triggers provide a trigger for high-momentum track candidates passing through both the Spectrometer and the ToF.

There are also several detectors dedicated to triggering on collision events. These include the paddle counters, Time-Zero (T0) detectors, Cherenkov detectors, and zero-degree calorimeters (ZDCs). In addition, the proton calorimeters and spectrometer calorimeter provide further information used to select interesting collision events.

The PHOBOS coordinate system is shown in Fig. 3.1 and defined with the origin at the nominal collision point in the center of the Octagon. The z axis runs along the beam axis, the y axis runs vertically out of the detector, and the x axis runs horizontally away from the ToF walls in order to maintain a right-handed coordinate system.

Also important to the Phobos coordinate system is the naming convention for rows and columns in the silicon detector pads. The column number of a pad changes as the pseudorapidity or z-coordinate is changed. The row number of a pad changes with the azimuthal coordinate around the collision axis.

3.2   Silicon Multiplicity Array

The PHOBOS silicon multiplicity array is designed to provide the number and angular distribution of charged particles emanating from the collision point over a broad range of pseudorapidity. The detectors are made up of silicon pads arranged in a single layer, located very close to the beam pipe. All support structures are made up of low Z materials in order to minimize scattering and background production of particles traversing the detectors.

3.2.1   Octagon

The Octagon is a single layer of silicon centered around the nominal collision point and spans $|z| < 55$ cm. It is shown in Fig. 3.2. It is made up of eight ladders of silicon that run parallel to the beam and surround the beam pipe in a barrel-shaped configuration. The diameter of the Octagon in the plane transverse to the beam is 90 mm between ladder faces. Each ladder contains up to 13 silicon sensors that run parallel to the beam pipe in the longitudinal direction.

Near the midrapidity region, sensors have been removed from the ladders facing the Spectrometer and the Vertex detectors to allow full acceptance of particles into these detectors with no additional scattering from the Octagon sensors. Fig. 3.3 shows the positions of the Spectrometer and Vertex detectors with respect to the Octagon. Each Octagon "hole" spans three Octagon sensor layers. Other than these holes, the Octagon has nearly full azimuthal coverage and provides a pseudorapidity coverage of $|\eta| \leq 3.2$. Each sensor is 84 mm long and 36 mm wide and is divided into 120 pads of 4 rows in the azimuthal direction and 30 columns in the z direction. The Octagon is mounted to a lightweight aluminum frame that
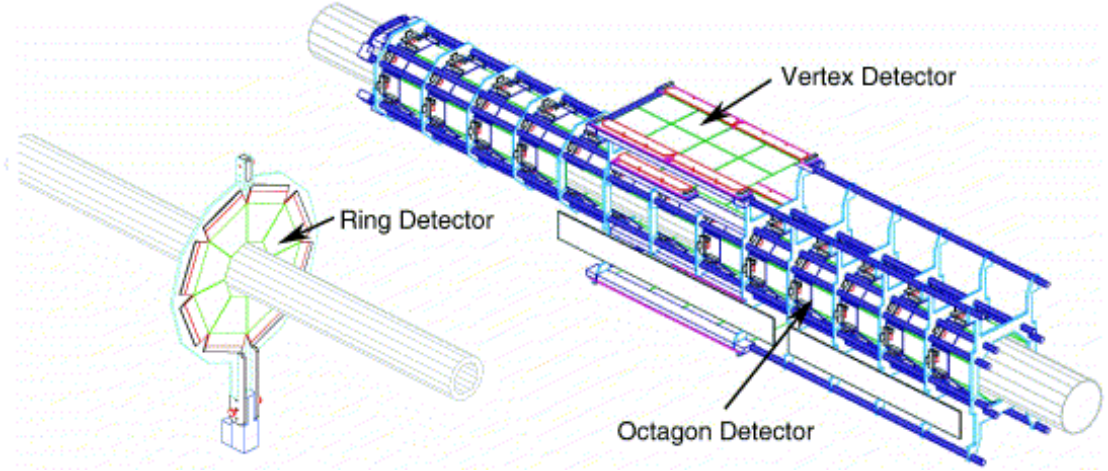
Figure 3.2: (Left) A single Ring detector. (Right) The Octagon and Vertex detectors shown with support structures around the beam pipe.

provides support and also transports chilled water through the system to cool the electronic readout chips that are affixed to each sensor.

3.2.2   Rings

There are six Ring detectors located at $z = \pm 1.13$, ± 2.35, and ± 5.05 m from the nominal collision point and extend the pseudorapidity coverage of the multiplicity array to $|\eta| \leq 5.4$. A single Ring module is shown in Fig. 3.2. Each Ring is made up of eight trapezoidal silicon sensors that surround the beam pipe, forming an octagonal shape. Each sensor is made up of 64 pads arranged in 8 rows in the azimuthal direction by 8 columns in the radial direction from the beam pipe. The pad sizes are chosen so that each pad covers the same area of $\Delta \eta \sim 0.1$ and $\Delta \phi \sim \pi/32$. The pad sizes closest to the beam pipe are roughly 3.8 mm by 5.1 mm, while those furthest from the beam pipe are roughly 10.2 mm by 10.2 mm. The inner diameter of each Ring is 100 mm and the outer diameter is 220 mm.
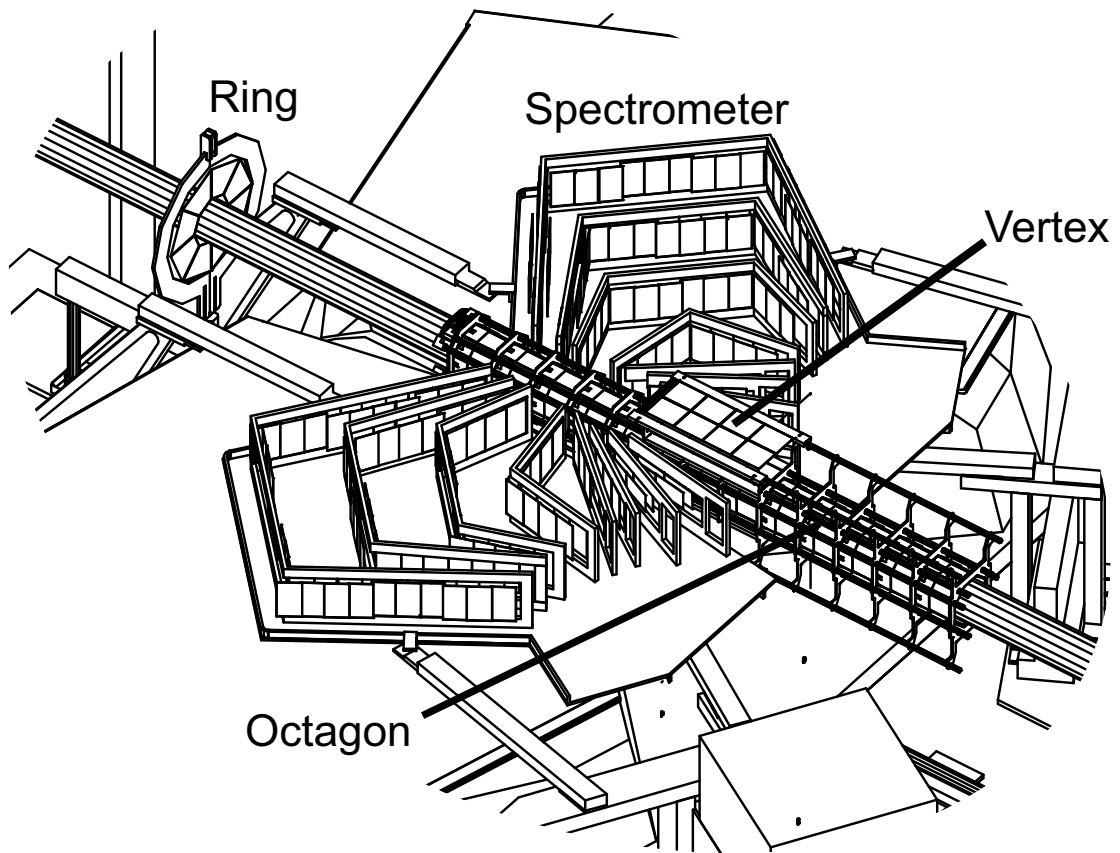
Figure 3.3: The central region of the PHOBOS detector, illustrating the relative positions of the Octagon, Vertex, and Spectrometer detectors.

Each module is mounted on a carbon fiber frame and also provides support to the printed circuit boards that carry signals from the modules to the readout cables.

3.2.3   Vertex Detector

The Vertex detector consists of four planes of silicon, two above and two below the collision point. It is shown on the right side of Fig. 3.2. The primary function of this detector is to determine the collision point by reconstructing two point particle tracks above and below the vertex position. The vertex resolution along

the z-axis is $\sigma_z \sim 200\mu m$ [27]. It also provides multiplicity measurements over its phase space range.

The inner layer of the Vertex detector is composed of two modules located at $y = \pm 56$ mm. Each is separated into four sensors that run longitudinally with the beamline, and each sensor is broken down into 512 pads composed of 4 rows in the azimuthal direction and 128 columns in the longitudinal direction. The pad sizes are 0.473 mm by 12.035 mm. The Outer Vertex planes are located at $y = \pm 188$ mm from the collision axis. Each plane contains eight sensors, four along the longitudinal direction and two in the azimuthal direction. Each sensor is divided into 256 pads, with two rows of pads in the azimuthal direction and 128 columns in the longitudinal direction. The outer Vertex pad sizes are 0.473 mm by 24.070 mm.

The pseudorapidity coverage of the Inner Vertex detectors is approximately $|\eta| < 1.54$, and the Outer Vertex detectors is $|\eta| < 0.92$ for collisions at z=0. The azimuthal coverage of both inner and outer layers is $\Delta\phi = 42.7$ degrees.

3.3   Spectrometer

The PHOBOS Spectrometer consists of two arms in the x-z plane located on opposite sides of the beamline. It is shown in Fig. 3.4. Each arm contains 16 planes of silicon sensors of various sizes. Each Spectrometer arm sits in a dipole magnetic field with a maximum field strength of 2 T. When the magnet is energized, one Spectrometer arm experiences a positive magnetic field, while the other experiences a negative field. The Spectrometers accept about 2% of the produced particles for a given event. Particle identification is done by measuring the dE/dx

energy loss of charged particles as they pass through the planes. The particles bend as they traverse the magnetic field, which allows for momentum determination using curved tracking algorithms. Pions and kaons can be identified up to 700 MeV/c, while the ability to distinguish protons from pions/kaons has been achieved for momenta up to 1.2 GeV/c.
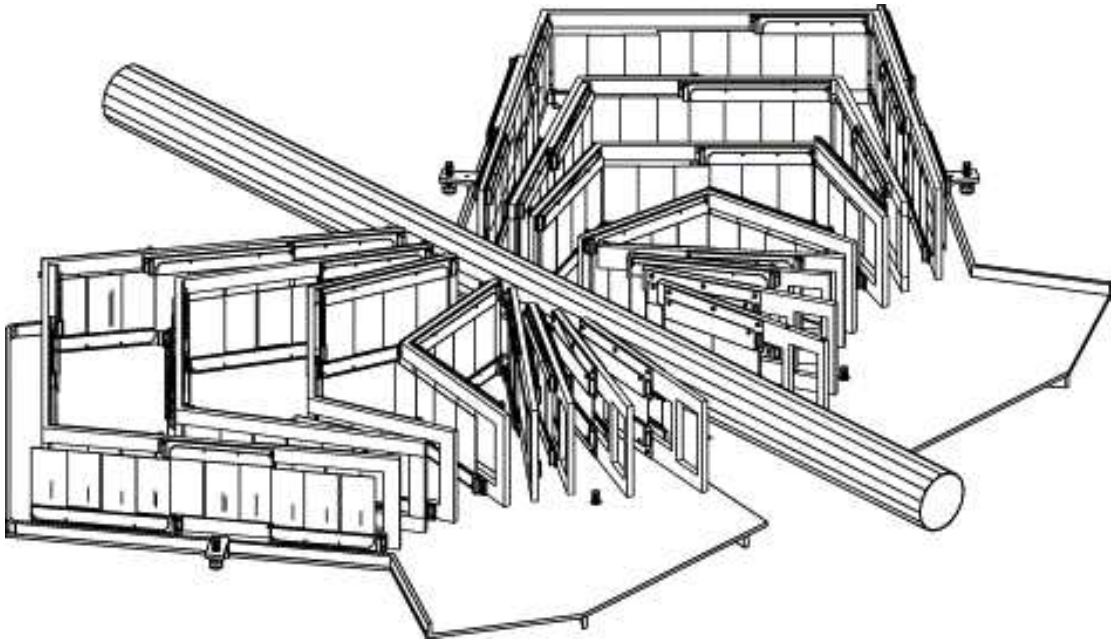
Figure 3.4: The PHOBOS Spectrometer and the beryllium beam pipe.

The first six planes of each Spectrometer arm sit in a region that is outside the strong magnetic field. The main purpose of this region is to provide starting tracks for curved tracking algorithms in the high magnetic field region, but it also allows for straight-line tracking in order to determine the collision point. In addition, the field free region is used for the mass determination of particles with very low transverse momentum (<100 MeV/c) that stop in the first five planes of silicon [28].

3.4 Silicon Sensor Design

Although the silicon pads of the various subdetectors vary in shape and size, they share a common basic design [26]. Fig. 3.5 shows the schematic diagram of a typical silicon pad. Each pad is nominally 300 μm thick and composed of a fully depleted, reversed biased p-n junction. When a charged particle passes through the pad, ionization leads to the creation of electron-hole pairs which register as a measurable current in the readout chips which are located at the edge of each sensor.
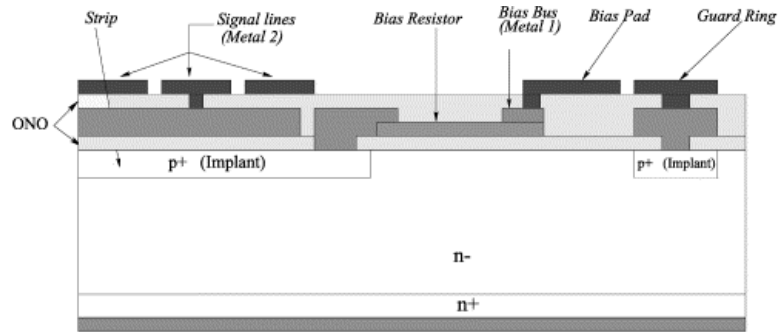
Figure 3.5: Schematic diagram of the cross section of a silicon detector pad. From reference [26].

Each sensor is a single sided, AC coupled detector that uses double-metal layers to route signals from the pads to the readout chips. The p+ implants in the sensor act as rectangular pads and provide two dimensional position information of charged particles. The implants are biased via 5 $M\Omega$ polysilicon resistors. The signals are AC coupled through a coupling capacitor consisting of a 0.2 μm oxide nitride oxide layer (ONO) and the first metal layer. An additional 1.2 μm ONO dielectric layer sits on top of the first metal layer which carry the second metal signal traces to the readout chips. The active area of the silicon wafer is

surrounded by a guard ring. A schematic of individual Octagon, Ring and Vertex sensors, illustrating their respective pad configurations, is shown in Fig. 3.6.
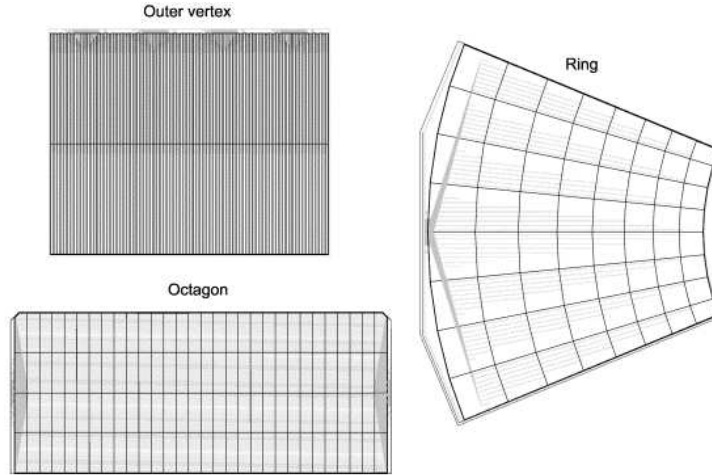
Figure 3.6: Schematic diagram of a Vertex, Ring, and Octagon sensor, illustrating the individual pads and the signal trace lines. From reference [26].

3.5 Magnet

The PHOBOS magnet is a room temperature magnet in a double dipole configuration. Fig. 3.7 shows a diagram of the magnet. A magnet dipole is located on either side of the beam pipe, and the vertical distance between pole tips is 158 mm. The pole pieces are cut to provide no field along the z-axis as well as in the first six planes of the Spectrometer. At full energy, the magnet produces a field of 2.18 T in the y direction. Fig. 3.8 shows strength of the field in the x-z plane. The field rises from zero to full strength at about 400 mm from the beam (z) axis, and then stays relatively constant inside the pole tips. The B_x and B_z components of the magnetic field are less than 0.05 T throughout this region. The field polarities on the two sides can can be reversed.
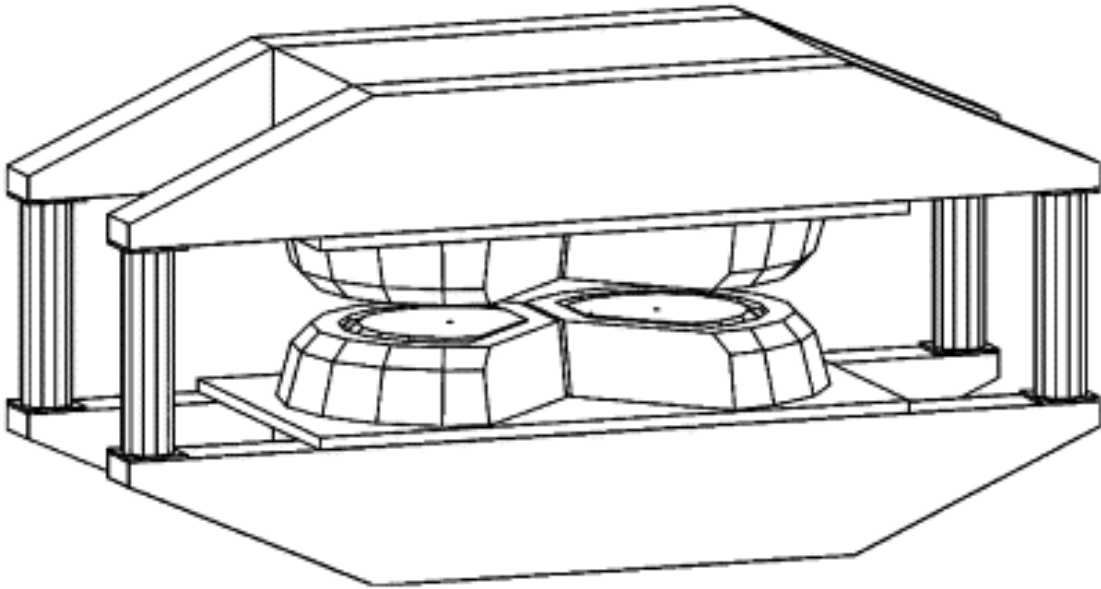
Figure 3.7: The PHOBOS Magnet.
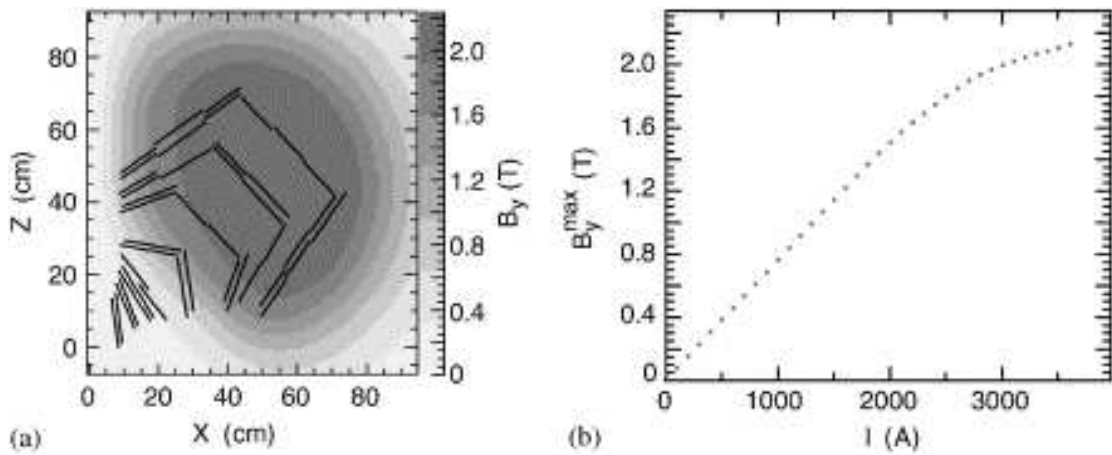
Figure 3.8: (Left) The y component of the magnetic field in one of the Spectrom-eter arms. (Right) Strength of the magnetic field versus current supplied to the magnet.

3.6   Paddle Counters

The paddle counters [29] serve as the primary triggering detector for PHOBOS. The setup consists of two arrays of 16 scintillating plastic detectors located at $z = \pm 3.32$ m from the nominal collision point and cover a pseudorapidity range of $3 < |\eta| < 4.5$. One of the arrays is illustrated in Fig. 3.9. When a particle passes through one of the paddles, it gives off scintillating light which registers as an energy signal in the phototube coupled to the scintillator. An energy signal above a certain threshold is counted as a "hit" in that module. The time difference between hits in the trigger arrays on the positive and negative sides in η allows for a cut such that only collisions in the central detector region are accepted. The paddle timing resolution is about 1 ns. The collision centrality can be determined by observing the number of paddles hit as well as the total energy deposited.
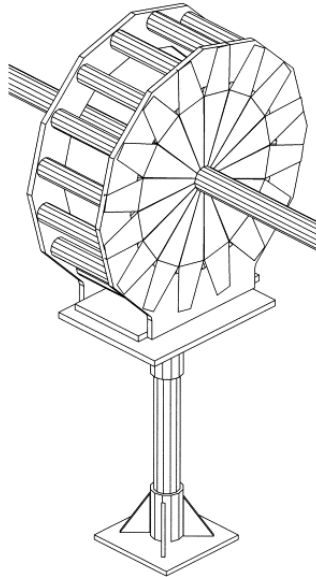
Figure 3.9: One of the PHOBOS paddle counters.

3.7   Zero-Degree Calorimeters

PHOBOS contains a set of Zero-Degree Calorimeters [30] which serve as an additional triggering device by detecting spectator neutrons. Each of the RHIC experiments possesses an identical set of ZDCs that serve as a common device to measure luminosity and centrality using free neutrons created from fragmentation of the colliding nuclei. The ZDCs are located at $z = \pm 18.5$ m just after the DX magnet where the RHIC beam branches back into two beam pipes, as shown in Fig. 3.10. The calorimeters are made of alternating layers of tungsten and optical
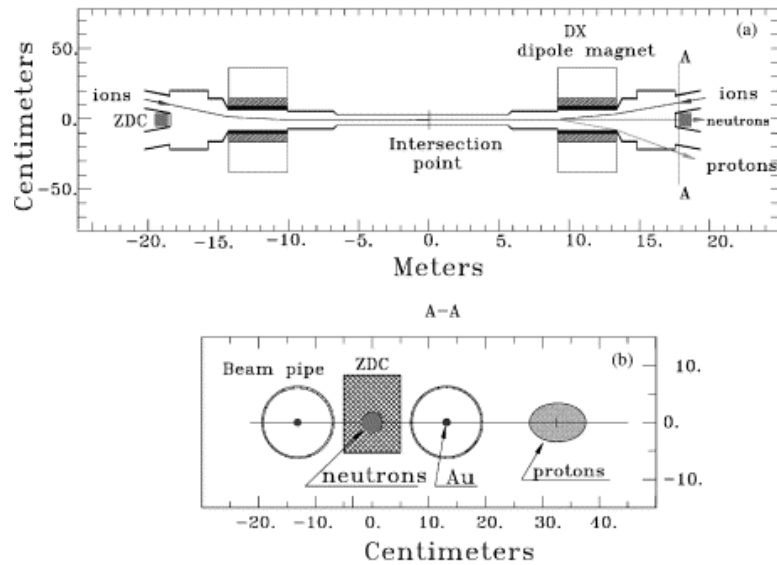
Figure 3.10: (Upper Panel) Position of the PHOBOS Zero-Degree Calorimeters with respect to the RHIC rings. (Lower Panel) Position of the Zero-Degree Calorimeter in the plane transverse to the beam pipe. The locations of neutrons and protons freed during the collision are also noted. From reference [30].

fibers to detect Cherenkov light. All fibers are bundled and fed into a photomultiplier tube. Three ZDC modules are placed in a row along the beamline on each side of the interaction region. The signal provided by the ZDCs is anticorrelated

with the signal from the paddle counters and will be shown in a later section. The
ZDCs also provide an independent event trigger for all experiments that can be
used during beam tuning in order to provide the greatest luminosity for all four
experiments simultaneously.

3.8   Time-of-Flight Walls

The Time-of-Flight walls consist of two arrays of 120 plastic scintillator slats that
lie beyond one of the Spectrometer arms. As the name indicates, these detectors
measure the time of flight for particles produced in the collision to hit the walls.
This roughly doubles the momentum acceptance for identified particles relative to
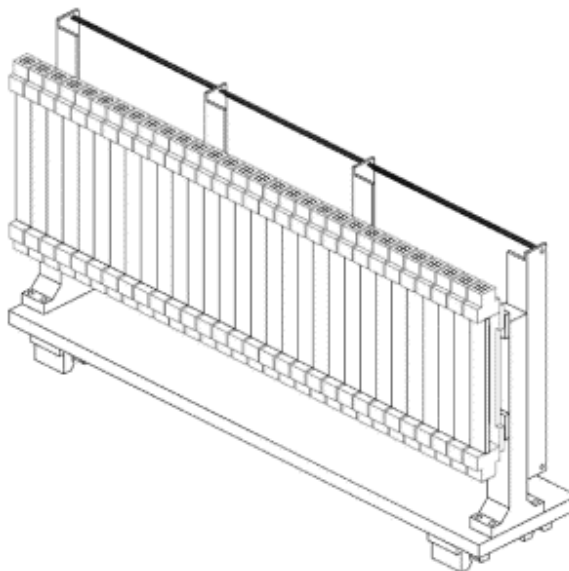
Figure 3.11: One of the PHOBOS Time-of-Flight walls.

the particle identification achieved using the Spectrometer alone. Each slat is 200
mm high and has a cross section of 8 mm x 8 mm. Fig. 3.11 illustrates one of the
ToF walls. The start time for the time of flight is provided by the T0 detectors.

3.9   Cherenkov Detectors

The Cherenkov detectors [31] are made up of 16 Lucite radiators, each coupled to a phototube. They are arranged around the beam pipe and located at $z = \pm 5.5$ m. The timing resolution of the Cherenkov detectors is around 270 ps, which is much better than the paddles. These detectors were used primarily in the first two running periods to provide an online vertex timing cut. However, they were eventually phased out in place of the T0 detectors which have much better resolution. Fig. 3.12 shows one of the Cherenkov detector arrays.
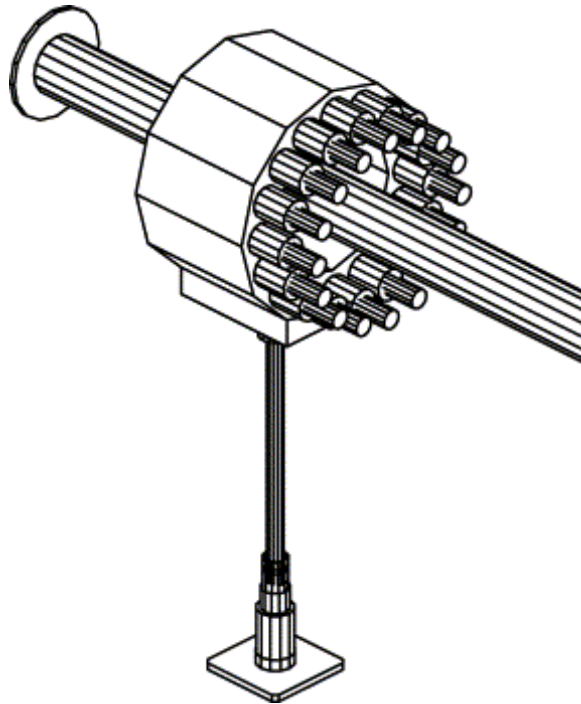
Figure 3.12: One of the PHOBOS Cherenkov radiator arrays.

3.10   Time-Zero Detectors

The Time-Zero (T0) detectors are an additional array of Cherenkov radiators that are arranged in a circle around the beamline on opposite sides of the nominal collision point. Each counter is composed of ten Cherenkov radiators that are each 25 mm thick and have a diameter of 50 mm.[1] Each radiator is coupled to a phototube and positioned 10 cm from the beam pipe. The time resolution is 110 ps. The arrays are positioned at $z = \pm5.2m$. The detectors are able to determine an online collision point that is optimized for the Spectrometer and multiplicity array and thus can be used as a trigger to accept more events in a useful detector region for analyses than those accepted from a paddle timing cut alone.

3.11   Spectrometer Triggers

Another horizontal arrangement of two rows of 10 scintillating slats are placed between the ToF wall and Spectrometer, as shown in Fig. 3.1. The purpose of the Spectrometer Trigger (SpecTrig) system is to provide a trigger for high-momentum tracks in smaller collision systems such as d+Au and p+p. Timing coincidences between the SpecTrig and ToF in conjunction with the vertex position given by the T0 detectors provide an online trigger selection for events with high-momentum tracks that pass through the Spectrometer and ToF subsystems.

---

[1]The T0 detectors were installed after the 130 GeV Au+Au data run. They were originally made up of four radiators on each side of the collision point during the 200 and 19.6 GeV Au+Au runs, and after this running period they were upgraded to ten radiators on each side.

3.12   Additional Calorimeters

Two Proton Calorimeters (PCals) are located adjacent to the ZDCs on the outer side of the RHIC rings, as shown in Fig. 3.1. The DX magnets bend individual spectator protons away from the beam (see Fig. 3.10), so the PCals are set in place to accept these protons and detect the subsequent shower. The detectors are composed of alternating lead and scintillator layers. Each module is 10 cm square and about 120 cm long, and stacked in a 12 row by 8 column configuration. These detectors are particularly useful in d+Au collisions. When the PCal signal is coupled with the ZDC signal on the side of the collision where the deuteron exits, events can be divided into d+Au, n+Au, and p+Au events based on what is observed in the ZDC and PCal.

Similar modules were also placed beyond the Spectrometer arm opposite the ToF side. The Spectrometer Calorimeter is shown in Fig. 3.1. It was installed before the 2004 run for the purpose of providing a trigger for very high-momentum tracks that enter the Spectrometer acceptance.

3.13   Collision Triggering

As previously mentioned, there are several different subsystems that provide triggering information. The paddle counters act as the primary event trigger. Requiring at least one or two paddle counters to register a hit on each side of the interaction region signifies a possible collision event and readies the data acquisition system to record the detector signals. A time-difference cut in the paddles restricts the longitudinal range of vertex positions so that they are roughly cen-

tered in the detector and eliminates beam-gas interactions. These interactions are events where beam ions scatter off gas molecules in the beam pipe, and the deflected ions pass through both sets of paddles. Beam-gas events show up as side peaks at $\pm 21ns$ on the time-difference plot, corresponding to the time it takes for a particle at nearly the speed of light to travel the 6.4 m distance between the two paddles. Fig. 3.13 shows the time-difference plot for the paddles.
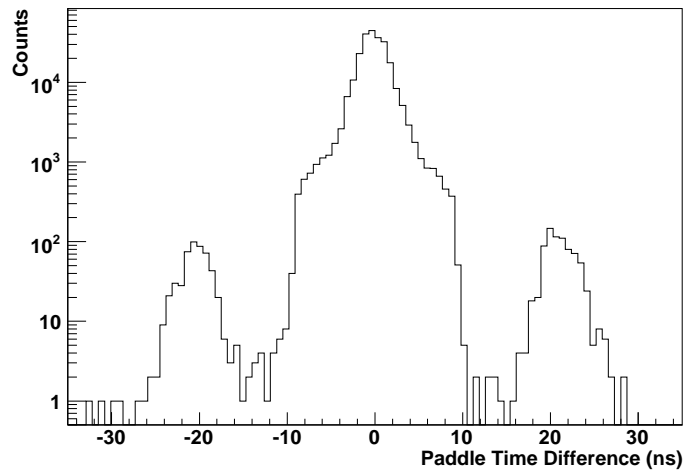
Figure 3.13: The paddle time difference for 200 GeV Au+Au collisions. The side peaks represent beam-gas events.

The T0 detectors possess better timing resolution than the paddles (110 ps compared to 1 ns), so they are used to more effectively select events centered in the Spectrometer and multiplicity detectors that are useful for analyses. The timing cut in the T0s restricts collisions within about $|z| < 200mm$. The collision point is more precisely determined offline using tracking in the Vertex and Spectrometer detectors.

3.14 Centrality Determination

Since the impact parameter, b, and the number of participants, N_{part}, cannot be directly measured, we must employ other methods to determine the collision centrality. Monte Carlo simulations show that there is a monotonic relationship between the number of participants and the paddle energy signal measured with PHOBOS. Fig. 3.14 illustrates the relationship between N_{part} and the mean paddle signal taken from Monte Carlo studies. Fig. 3.14 also shows the anticorrelation between the ZDC signal from the spectator neutrons and the Paddle signal from
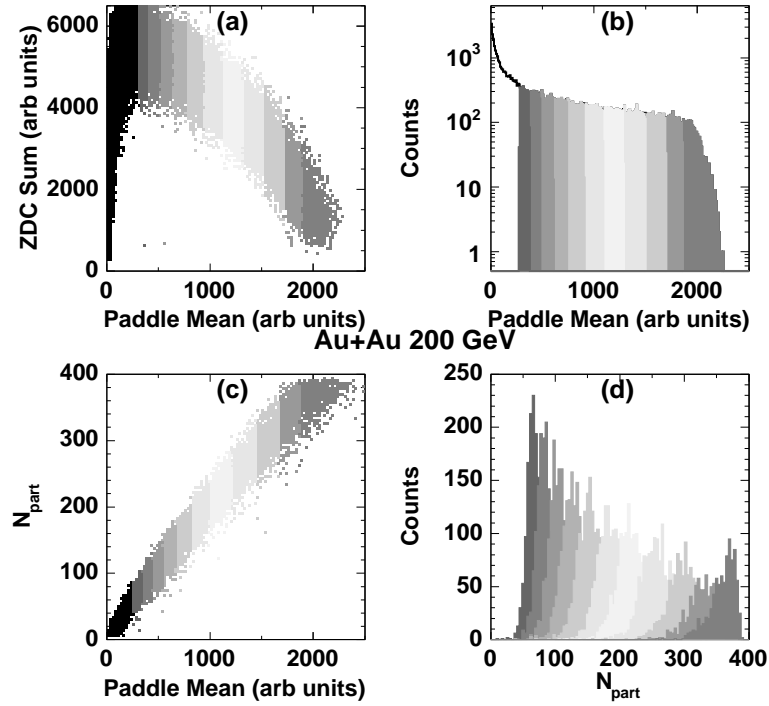
Figure 3.14: Centrality variable correlations [6]. (a) ZDC signal vs. Paddle signal from experimental Au+Au collisions at 200 GeV. The shaded bands represent centrality bins in percentile cross section cut on the paddle mean signal. (b) Paddle mean distribution from (a). (c) N_{part} vs. Paddle signal from an MC simulation. (d) The N_{part} distribution for the centrality bins. The average N_{part} in each bin can be extracted from this plot.

the charged particle multiplicity. The relationship between N_{part} and paddle mean allows actual events measured in PHOBOS to be categorized into centrality bins based on the paddle mean. These bins, shown as shaded bands in Fig. 3.14, represent consecutive percentage bins of the total inelastic cross section. Incorporating Glauber model calculations of the collision geometry within the simulation allow for the estimation of N_{part} for each cross section bin.

The paddle mean method of centrality determination works well for Au+Au collisions at $\sqrt{s_{NN}}$ =62.4, 130, and 200 GeV. However, at 19.6 GeV the number of particles produced in the pseudorapidity range of the paddles $(3.2 < |\eta| < 4.5)$ is very low, causing a reduction in the monotonicity between the paddle energy signal and N_{part} in this region. A new pseudorapidity range is chosen for 19.6 GeV based on the ratio of the beam rapidities between 200 and 19.6 GeV. Scaling the paddle pseudorapidity range by $y^{beam}_{19.6}/y^{beam}_{200}$=0.563 gives a new pseudorapidity range of $1.8 \leq |\eta| \leq 2.5$ which lies within the Octagon coverage. Hence, the multiplicity in the Octagon is used in place of the paddle signal to determine centrality at the lowest collision energy. Similar centrality determination methods using the Octagon for the higher collision energy data sets gives consistent results. [32]

3.15   Vertex Determination

A reliable determination of the collision point is crucial for data analysis. The signals registered in the detector must be referenced with respect to the vertex in order to determine the pseudorapidity and angular coordinates of the measured charged particles. As mentioned before, the timing signals from the paddles and T0 detectors provide the z coordinate of the vertex with an accuracy of a few

centimeters, but they do not provide the x or y coordinates. The silicon detectors are used in offline analysis to determine the x and y coordinates as well as a more precise z coordinate. The Vertex detector gives excellent z and y resolution for the vertex, but not in the x direction. The Spectrometer vertex finding algorithm using straight tracks in the first six planes of the magnetic field free region provides vertex resolution in all three directions. If the reconstructed tracks in the Vertex or Spectrometer detectors do not point back to a common collision point, then the vertex is marked as invalid, and the event is not used for analysis. Fig. 3.15 shows the x, y, and z distributions of the vertex reconstructed from the Spectrometer. Only collisions with a z vertex position within 10 cm of the nominal collision point were accepted for the results shown.
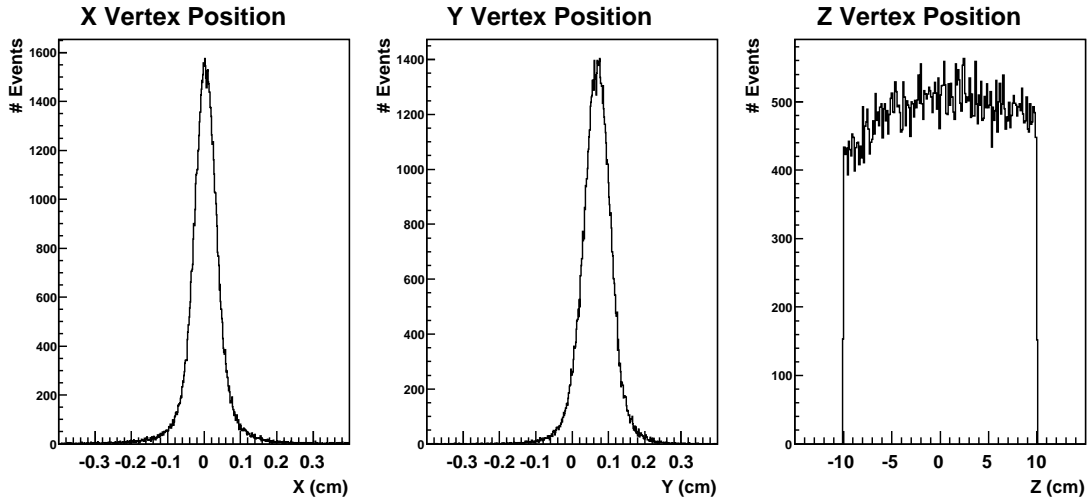
Figure 3.15: Reconstructed vertex position distributions for 200 GeV collisions in the 0-40% centrality range. Only collisions in the $z \leq 10$ cm region are shown.

3.16 Event Selection

Collision events must pass a selection to ensure only good quality events are used
for analysis. The selection includes the triggering conditions described above such
as a paddle time difference of less than 4 ns and at least two hits in each paddle
array, as well as a suitable ZDC signal. For very central events, there will not
be many neutrons impinging upon the ZDCs; however, the summed energy signal
in the paddles is very large and is used in place of the ZDC signal for event
selection. In addition, there must be a valid vertex reconstructed from the Vertex
and Spectrometer detectors, and the vertex must occur within a window of $|z| \leq 10$
cm of the nominal collision point.

The vertex position in the x-y plane, commonly known as the beam orbit, must
also be stable for the data analysis. Only data runs are used in the analysis where
the average x and y vertex position did not shift much during data taking. Events
located within a 2-σ range of the mean of the x and y distributions (as shown
in Fig. 3.15) are accepted and used in analysis. Any small offset in the beam
orbit from the nominal (0,0) position is reasonable and can be remedied through
acceptance weighting corrections, which are discussed in the next chapter.

3.17 Monte Carlo Simulations

Simulations of heavy-ion collisions in the PHOBOS detector are used to check de-
tector acceptance and analysis methods in addition to N_{part} determination. Colli-
sion events can be created using several different event generators. The one used
in conjunction with the analysis reported here is the Heavy Ion Jet Interaction

Generator (HIJING) [33]. The PHOBOS detector is simulated using the GEANT package [34]. The locations of the detector elements are taken from survey data and fed into GEANT, where particles produced with HIJING are simulated to pass through the detector. This production of events ensures simulated data that are as realistic as possible to the actual observed collisions in terms of the collision process and detector response.

Chapter 4

Basic Data Analysis

4.1 The Subevent Method in PHOBOS

The PHOBOS detector is useful for flow measurements in heavy-ion collisions due to the fine segmentation of the pads in the silicon multiplicity array. Charged particles traversing the silicon leave behind energy depositions due to ionization energy loss (dE/dx). Pads that receive a deposited energy greater than a certain threshold are recorded as "hits" and used in the analysis. Hits from one subevent region of the detector are used to calculate the event plane angle, as defined in Ch. 2. The event plane is correlated with hits from a different part of the detector to measure the flow signal. Since a charged particle yielding a hit can traverse the pad at any point, the coordinates of the hit are smeared within the physical η and ϕ boundaries of the hit pad in the offline analysis. Two subevents are used in the analysis of each event so that the flow can be determined in a section of the detector that is independent of the region where the event plane is determined. As mentioned in Ch. 2, the two subevent windows are required to cover similar

pseudorapidity ranges and be of equal multiplicity. This greatly simplifies the analysis by allowing the reaction plane resolution to be determined by correlating the two independent event plane angles.

4.2   Flow Analysis Method in PHOBOS

The longitudinal and azimuthal coverage of the Octagon is illustrated in Fig. 4.1. For clarity in describing the flow analysis method, it is best to assign a longitudinal sensor number to describe which annular sections of the Octagon along the z coordinate are being described. The first flow analysis from PHOBOS [15] was limited to the first five sensors of the Octagon detector in addition to the Rings. This part of the Octagon is free of Spectrometer and Vertex holes (as shown in Fig. 4.1), and is thus azimuthally symmetric. In honor of this symmetry, this part of the detector was dubbed the negative "SymOct" region and this particular flow analysis was called the SymOct analysis. In order to restrict the analysis to this region of the detector, the selected vertex range was $-38cm < z < -30cm$ and the subevent regions used to determine Ψ_2 were $-2 < \eta < -0.1$ and $0.1 < \eta < 2$. The drawback to these restrictions is that very few collisions occur in this region under normal triggering conditions. It is necessary, therefore, to either comb through a very large set of data and extract the collisions centered around z=-34 cm or conduct special data runs where the trigger window is centered around this region. Fig. 4.1 illustrates the SymOct region as well as the entire Octagon region with incomplete azimuthal symmetry.

In light of the statistical and acceptance limitations of the SymOct analysis, a new method was developed where collisions in the nominal collision zone
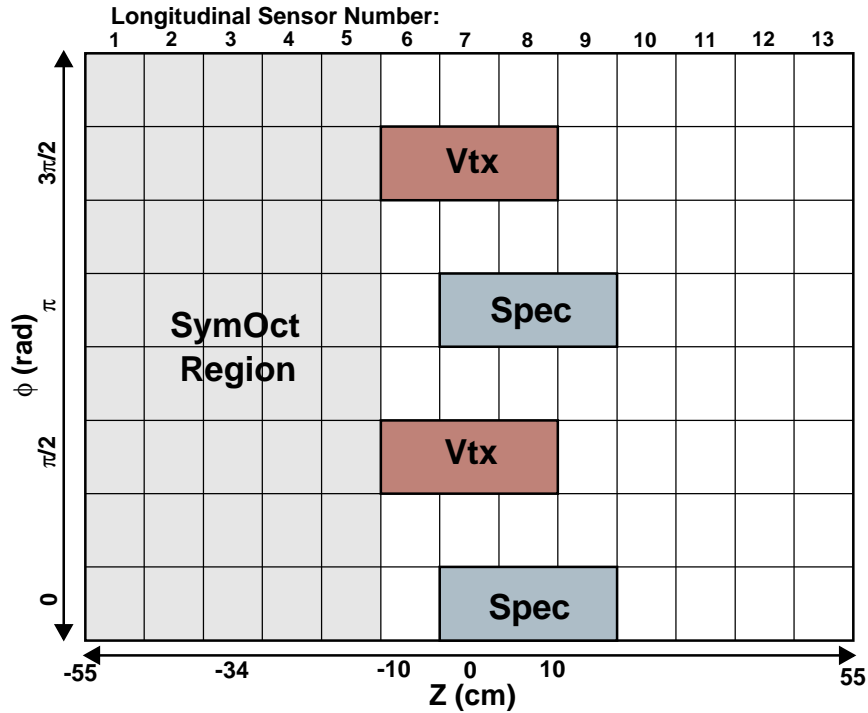
Figure 4.1: A schematic diagram of the unrolled Octagon detector, illustrating the 13 sensors along the horizontal (beam axis) direction as well as the 8 sensors in the vertical (azimuthal) direction. The blue and red boxes represent the Spectrometer and Vertex holes, respectively. The grey shaded region represents the SymOct region which was used in the first flow analysis.

($-10cm < z < 10cm$) could be used for a flow analysis. Because the collision range is centered around z=0 cm, this analysis is called the "MidZ" analysis method. The trigger window in this new analysis is the standard one with which the bulk of our data is taken. The potential drawback to using collisions in this region is that the Octagon does not provide full azimuthal coverage in this area. As mentioned in the previous chapter, holes exist in the Octagon to allow acceptance in the Vertex and Spectrometer detectors.

It is possible to use only the symmetric pieces of the Octagon in the forward and backward regions (sensor numbers 1-5 and 10-13, respectively) to find event

planes. However, given the vertex range these sections only cover a symmetric pseudorapidity region of $2.6 \leq |\eta| \leq 3$, which is a small window with a relatively low multiplicity as compared to the midrapidity region. Because of the small subevent size, the reaction plane resolution is very low in this region, and does not make for a robust flow analysis, although these subevents are used as a systematic check in the elliptic flow analysis.

For these reasons, special symmetrizing procedures in the Octagon hit map (dubbed "hole filling" and discussed below) were developed in order to smooth out the hit map such that the entire Octagon can be used in the analysis and therefore give results consistent with the "SymOct" method. In addition to providing higher statistics during long runs, this new analysis method yields more uniform coverage throughout η. One immediate advantage to the implementation of this method was that it allowed PHOBOS to obtain flow results for data sets such as at 19.6 GeV where the running period was small and lacked sufficient collisions in the SymOct region for a useful analysis.

4.3   Si Signal Processing

Charged particles that traverse a given detector pixel deposit energy that is directly proportional to the length of silicon traversed. Therefore, the energy of each hit is normalized to be equal to that expected for normal incidence. Also, using known values for the silicon thickness, the hits are normalized to a common pad thickness of 300 μm. In order to correct the data for variations in silicon sensor sensitivity, the minimum ionizing particle (MIP) peak for each sensor is scaled such that it is centered at 80 keV. Fig. 4.2 shows the deposited energy

spectra for Octagon sensors in a typical annular ring. Only those pads with a scaled normalized energy deposition greater than 50 keV are defined as a hit and used in the analysis.
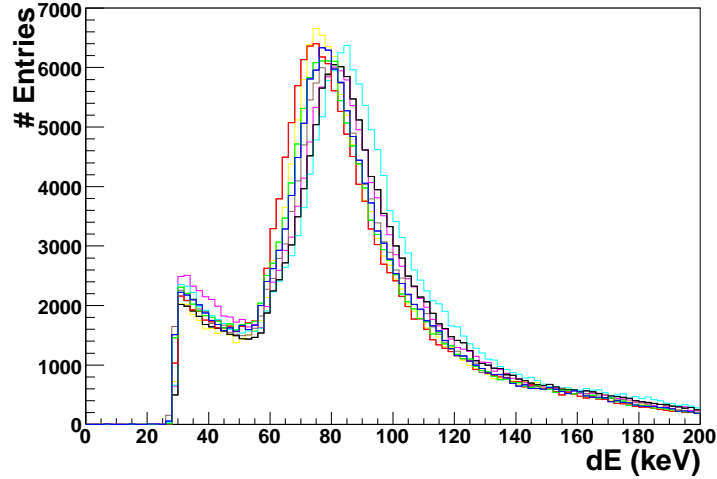
Figure 4.2: Deposited energy distribution for all eight Octagon sensors in the fourth longitudinal sensor set, over many events. The energies are angle corrected and normalized to a common sensor thickness. The sensors are then normalized such that the peak is at 80 keV.

4.4 Bad Channel Determination and Correction

This analysis requires a reasonably even azimuthal detector response in order to avoid biasing the results. One important step toward ensuring this even azimuthal response is to identify and remove pads with anomalous behavior. Such anomalous pads are called "bad" pads or bad channels. Fig. 4.3 shows the Octagon hit map taken over all events in the 62.4 GeV data set. The detector holes are visible as well as the bad channels, since they appear in contrast to the smooth color progression.
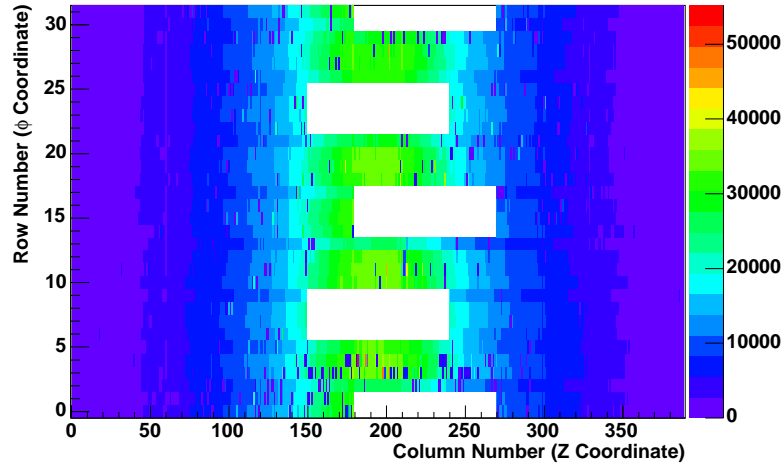
Figure 4.3: Raw Octagon hit map as a function of phi and beam axis position for the entire event sample at 62.4 GeV. The Vertex and Spectrometer detector holes are visible, as well as the bad channels.

Pixels in the total event hit map that receive either too few or too many hits with respect to neighboring pixels are flagged as bad. Bad channels are determined by mapping the hit distributions in a single Octagon or Ring column for the entire event sample. If any pixel receives more or less hits than 30% of the mean of that column, it is flagged as bad.

The removal of bad channels creates azimuthal asymmetries in the hit map that must be corrected in some fashion. In this analysis, a Poisson-based correction method is used to replace the bad channels in the hit map. In this technique, the fraction of hits from good channels in a detector bin is used to determine whether a bad channel in that bin should be counted as a hit for that event. A random number between zero and one is generated for each bad channel in a detector bin, and then that number is compared to the hit fraction from good channels. If the random number is less than the fraction, then that pixel is counted as a hit for

that event. The bad channels are corrected before the holes are filled, in order to not disturb the hole filling procedure.

4.5 Filling of Spectrometer Holes

Since the Octagon detector does not have sensors in the acceptance regions of the Spectrometer arms, a symmetrization procedure is performed. Incorporating hits from the first few layers of the Spectrometer into the Octagon hit map would only partially fill in the void in the Octagon because of the small pseudorapidity and azimuthal acceptance of the Spectrometer sensors in this region. A hole filling procedure has been devised in order to allow for the full use of the Octagon in this analysis.

In terms of Octagon detector size, the Spectrometer holes are three Octagon sensors wide in the collision axis (z) direction by one sensor high in the azimuthal direction, running from sensor numbers seven through nine, as shown in Fig. 4.1. In the flow analysis, the holes in the detector hit map are filled on an event-by-event basis with virtual Octagon hits. Fig. 4.4a shows a partial view of one of the Spectrometer holes and the Octagon detector pads immediately surrounding it. The virtual hits are created according to a linear extrapolation across the hole based on the hit densities in the neighboring Octagon sensors.

The Spectrometer hole filling process goes as follows. Fig. 4.4b-d steps through the process graphically for a typical event. It begins by determining the number of hits above and below a hole in a detector bin with a size of 5 columns by 2 rows (Fig 4.4b). Then, from this count the average number of hits per row directly above and below a hole is determined (also shown in Fig 4.4b). The slope
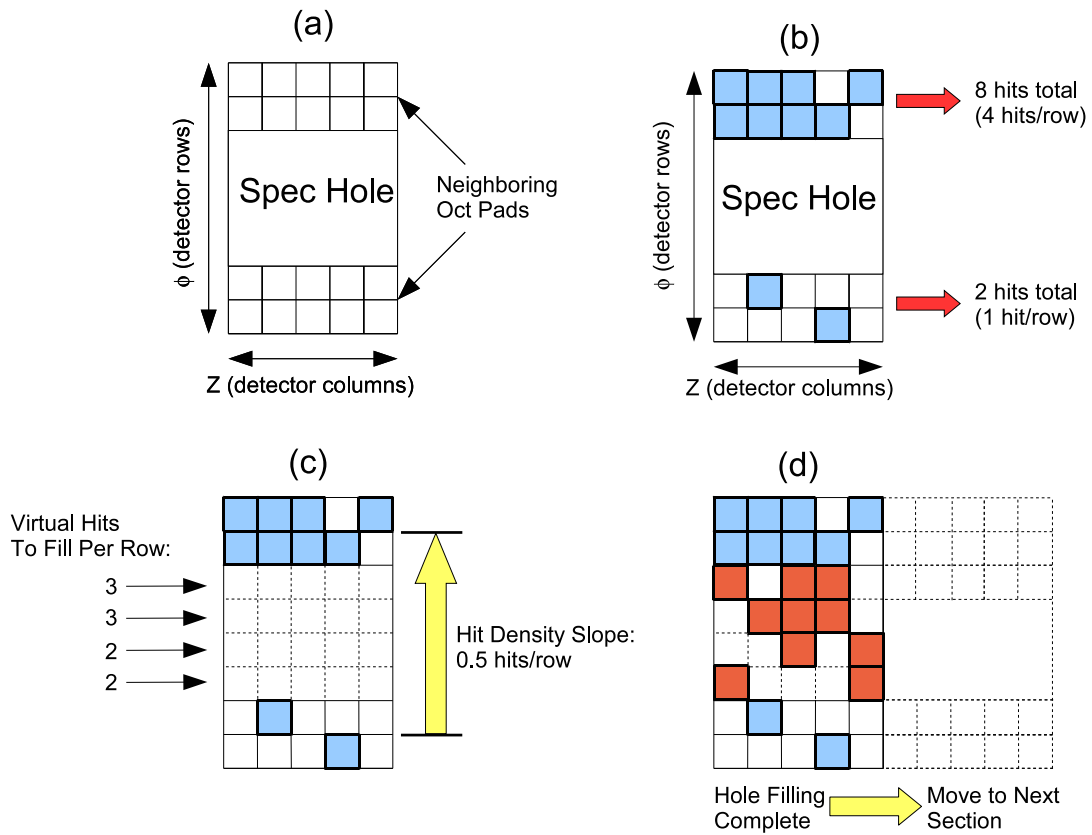
Figure 4.4: (a) Diagram of part of the Spectrometer hole region, along with the neighboring Octagon pads. (b) The neighboring hits are shown for a typical event. (c) The hit density slope is calculated, and from that the number of hits to fill in each row. (d) The virtual hits, shown in red, are filled in, and the process is repeated for the next detector section.

between the upper and lower average hit counts per row is calculated (Fig 4.4c). The number of hits to occupy each 5 column by 1 row detector section of the hole is determined based on the linear extrapolation from the value on one side of the hole to the other (Fig 4.4c). It should be noted that the number of hits to fill in each row determined from the linear extrapolation is rounded to the nearest integer. Next, each row is filled randomly across the 5 column section of the hole until the required number of filled hits is reached (Fig. 4.4d). A hit is assigned by

giving the (row, column) detector pixel a hit energy of 80 keV. The entire process is repeated for the next 5 column detector section (Fig. 4.4d). This procedure is followed until both holes in the detector hit map are filled.

4.6   Incorporation of Vertex Detector Hits

There exist holes similar in size to the Spectrometer holes in the positive and negative y directions (up and down at ± 90 degrees) that allow particles to enter the Vertex detector, along sensor numbers six through eight of the Octagon sensor map. The inner layer Vertex sensors have nearly the same phase space coverage as the missing Octagon sensors, so hits from the inner layer Vertex sensors are mapped into three virtual Octagon sensors. The Vertex inner layer sensors contain a total of 512 detector columns (compared to 90 for three Octagon sensors in the same area), so the virtual Octagon pixels are made up of merged hits from the Vertex detector. Fig. 4.5 shows the position of the inner layer Vertex sensors in relation to the Octagon.

The filling procedure for the Vertex holes goes as follows. The deposited energy for each Vertex inner layer pad is first normalized and angle corrected. The ϕ and η of each Vertex inner layer hit is also randomized within the pad boundaries, similar to what is done for Octagon hits. If the ϕ of a hit falls into the range of detection of the neighboring Octagon sensors, then it is discarded since the Octagon already provides that coverage. The correct row number within the Octagon hit map is determined according to the ϕ coordinate of the Vertex hit. The η of each hit is compared to the η of the Octagon hits in the neighboring sensors. The Octagon column number that most closely matches the η of the
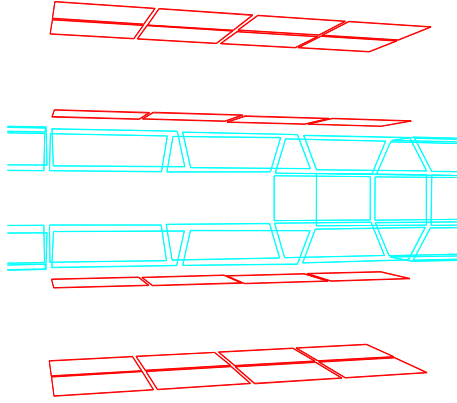
Figure 4.5: Zoomed-in view of the central Octagon sensors (blue), as well as the sensors in the inner and outer layers of the Vertex detector (red). The z axis runs horizontally and the y axis runs vertically.

Vertex hit is used as the new column number for the virtual Octagon hit. If a Vertex hit has been previously assigned to this row and column then the energy of the new hit is added to the existing hit energy.

In most events, there are pseudorapidity gaps between the end of the Vertex sensors and the next Octagon sensor in the z direction (sensor numbers 5 or 9, according to Fig. 4.1), depending on the vertex position. This is because the Vertex inner layer is sitting at a larger radial distance than the Octagon sensors. These gaps are filled with a linear extrapolation of the neighboring hit densities in the same way as the Spectrometer holes. Although the size of the gap varies due to the z vertex position, the gap size that is filled for a typical event is less than 10 Octagon detector columns.

The sensor gaps between the four Vertex sensors do not occur at the same position as the sensor gaps between the three Octagon sensors. For this reason,

when Vertex hits are near an Octagon sensor boundary, nearly all of them will be lumped into the η bin that corresponds to the first or last column of a given Octagon sensor boundary. This causes the two columns of the virtual Octagon layers immediately around a sensor boundary to be filled with more hits than the neighboring Octagon columns. Therefore, the two columns around the Octagon sensor boundaries are filled with hits using the Spectrometer hole filling technique.

Fig. 4.6 shows the Octagon hit map after the bad channel correction and hole filling procedures have been carried out.
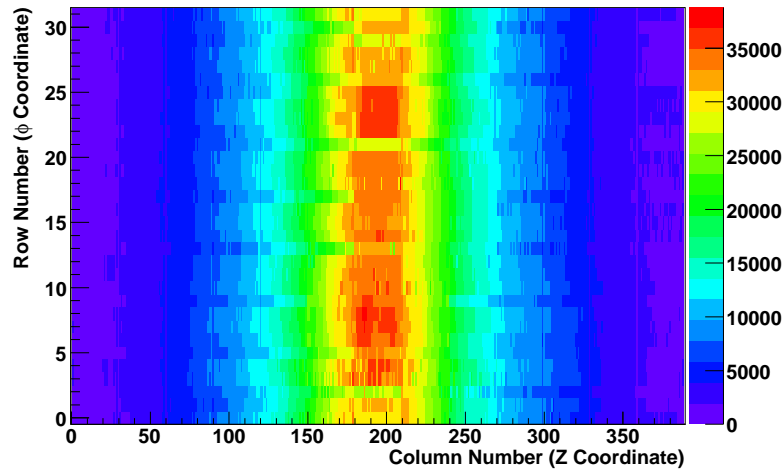
Figure 4.6: Octagon hit map after the bad channel corrections and hole filling procedure.

4.7 Weighting Matrix

The multiplicity detectors have an imperfect geometrical acceptance as well as gaps between sensor elements. Therefore, a weight is applied to each pad in the Octagon and Rings to correct for the phase space differences between pads. This

is done by taking the ratio of the average number of hits per pad in an annular detector section (i.e., a detector column) to the total hits for that pad according to

$$w^a(\eta, \phi) = \frac{\langle N_{hits,pad} \rangle_{col}}{N_{hits,pad}} \tag{4.1}$$

where the "a" superscript denotes acceptance weighting, and the angled brackets denote averaging over all pads in a given detector column. The weights are calculated using the total hit map taken over the entire event sample after the bad channel correction and hole filling procedures have been done, as shown in Fig. 4.6. The weights are then applied to the detector pads on an event-by-event basis. Typical acceptance weights are in the 0.8 to 1.2 range.
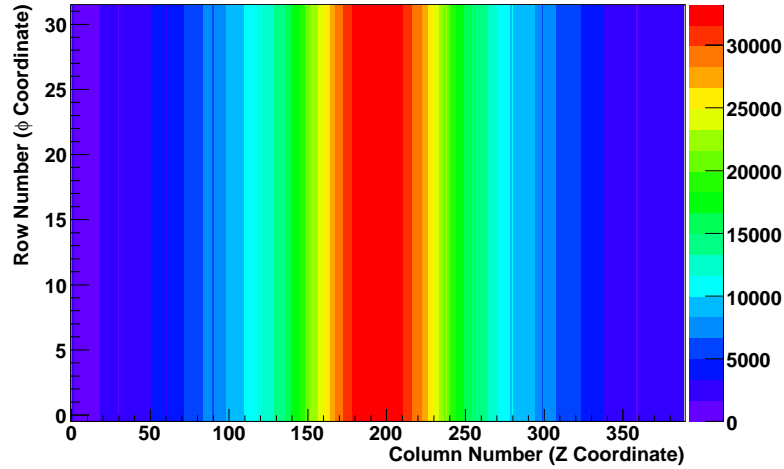
Figure 4.7: Fixed and filled Octagon hit map after the weighting matrix has been applied.

The annular ring is the same as a detector column, so the weights normalize the pixels in each slice of pseudorapidity over the entire azimuth. In the flow analysis, a weighting matrix is found for every 5 cm of Z vertex and two bins of

centrality. Fig. 4.7 shows the fixed and filled Octagon hit map after the weighting matrix has been applied. The smoothness of the total event hit map implies no major biases for the event-by-event flow analysis.

4.8 Occupancy Correction

An occupancy correction is also applied that accounts for instances where more than one charged particle track traverses a pad [35]. This correction is based on a Poisson statistical distribution and uses the number of hit (N_{occ}) pads and the number of pads without a hit (N_{unocc}) in a small section of the detector on an event-by-event basis, such that

$$Occ(\eta, \phi) = \frac{\mu}{1 - e^{-\mu}}, \tag{4.2}$$

where $\mu = ln(1 + N_{occ}/N_{unocc})$ is the average number of tracks per pad.

The default bin size in which to find the occupancy correction is 0.5 η by 5 detector rows in the Octagon, and 8 columns by 5 rows in the Rings. The bin is always centered around the pad under study. Alternate bin sizes are studied and accounted for in the systematic error determination of the final flow results. Fig. 4.8 shows a typical occupancy correction in the Octagon.

The occupancy and acceptance weights are combined and applied to each pixel in the event plane determination as follows:

$$w_i = w_i^a \ Occ(\eta_i, \phi_i). \tag{4.3}$$
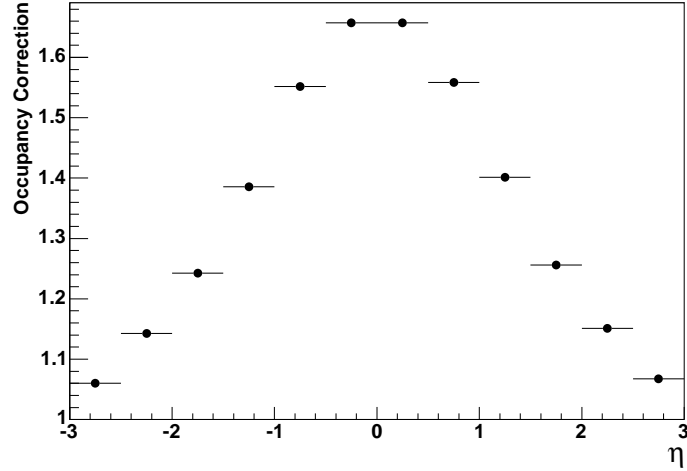
Figure 4.8: Occupancy correction in the Octagon as a function of pseudorapidity for the 6% most central collisions at 200 GeV. The occupancy correction is less for more peripheral events and lower energies.

4.9 MC Studies & Suppression Correction

Collision events are simulated using Monte Carlo simulations made with the HIJING event generator. Flow is injected into the collisions by slightly shifting the ϕ coordinate of each particle track [20] according to

$$\Delta\phi = \sum_n \frac{-2}{n} v_n \sin(n(\phi - \Psi_R)), \tag{4.4}$$

where v_n is the magnitude of the nth flow harmonic to be injected into the sample and Ψ_R is the true reaction plane. The ϕ angle of the tracks are randomized prior to shifting to eliminate all other azimuthal correlations that may be introduced by HIJING.

The simulated samples are analyzed in the same way as the data. The bad channel map found from the data is also used in the simulated events.

After analysis, the reconstructed flow signal from the MC event sample falls short of the true flow signal. This suppression is due to background particles from the beam pipe and other sources, including dilution of the flow signal due to the bad channel map and imperfections in the hole filling procedure. The ratio of the reconstructed to true flow level in the simulation is applied to the data in bins of pseudorapidity at each collision energy. This is the final correction to the data, and it is typically around 30%. The actual suppression values will be shown in the following chapters.

4.10 Systematic Error Determination

Many potential sources of systematic uncertainties are studied in this analysis. The 90% confidence level systematic errors are determined by varying a certain aspect of the analysis within reasonable limits from its baseline level and using that new value within the analysis to get a new final result. The deviation between the new result and the baseline result is taken as the systematic uncertainty. This is done over a wide range of sources, and then the deviations from all the sources are added in quadrature to give the final 90% confidence level systematic error. The systematic errors of directed and elliptic flow will be discussed in more detail in the following chapters.

4.11 Data Runs Used in the Analysis

The data runs used in this analysis are given for each collision energy in Table 4.1. Each data set was used to find both the directed and elliptic flow results that are reported in the following chapters.

Table 4.1: Data runs used in the analysis.

Collision Energy (GeV)	PHOBOS Runs Used	Total Number of Events
19.6	9199-9228	13826
62.4	14577-14583	102555
130	5008-5425	53626
200	8808-8809	49592

Chapter 5

Elliptic Flow

5.1 Event Plane Distributions and the Reaction Plane Resolution Correction

The subevent windows in the elliptic flow analysis are defined as $-3.0 \leq \eta \leq -0.1$ to find the negative event plane, Ψ_{2N}, and $0.1 \leq \eta \leq 3.0$ to find the positive event plane, Ψ_{2P}. For every event, hits in the positive η hemisphere are correlated with Ψ_{2N}, and hits in the negative η hemisphere are correlated with Ψ_{2P}.

Fig. 5.1 shows the azimuthal angle distributions of the negative and positive Ψ_2 event planes over the entire event sample at each energy in the 0-40% centrality range. A flat event plane distribution over the entire sample is indicative of an analysis that is free of azimuthal biases. Unfortunately, there is some structure in the event plane distributions, particularly at 19.6 GeV. Additional studies using Monte Carlo samples and reaction plane flattening methods have been done to ensure that the event plane structure does not affect the final result.
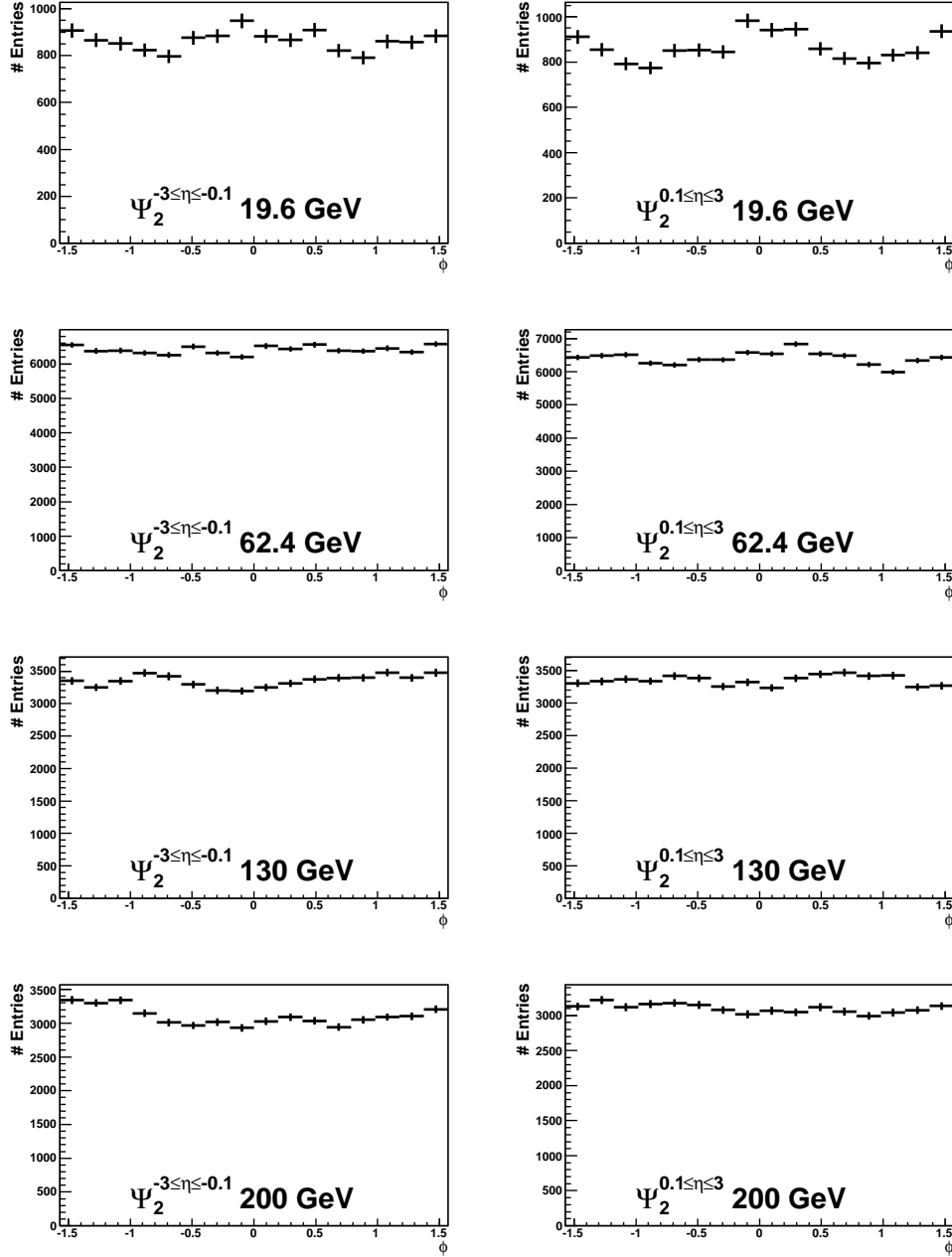
Figure 5.1: Reconstructed event plane angle distributions of Ψ_2 from the negative $(-3.0 \leq \eta \leq -0.1)$ and positive $(0.1 \leq \eta \leq 3.0)$ subevent windows. The distributions are shown in the 0-40% centrality range. The error bars represent the square root of the number of entries in each bin.

Fig. 5.2 gives the event plane correlation, $\langle cos\ 2(\Psi_{2N} - \Psi_{2P})\rangle$, between the positive and negative subevent windows. The correlation is found on an event-by-event basis and then averaged over the centrality bins shown. To apply the resolution correction to the data, v_2 is first found in a 2-dimensional matrix of centrality and pseudorapidity. Each bin is divided by the square root of the centrality-dependent event plane correlation. Then the resolution-corrected elliptic flow is averaged over the centrality bins to yield the resolution-corrected v_2 vs. η plot. The final step is to apply the suppression correction to this plot.
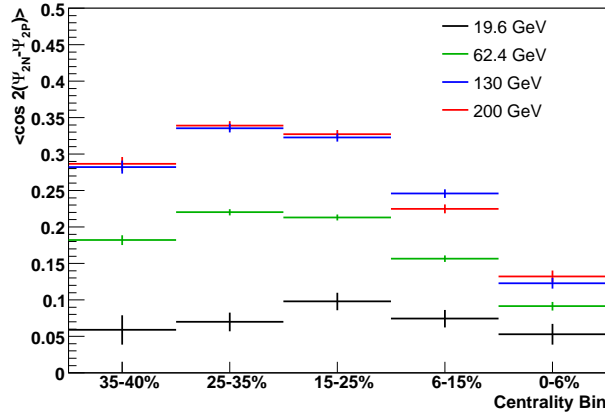
Figure 5.2: Event plane correlation, $\langle cos\ 2(\Psi_{2N} - \Psi_{2P})\rangle$, averaged over events as a function of centrality for each collision energy. The statistical errors are shown for each centrality bin.

5.2 Suppression Correction and Other Monte Carlo Studies

Monte Carlo simulations showed a residual suppression of the flow signal, mainly due to background particles that carry no flow information and the loss of sen-

sitivity due to imperfect bad channel correction and hole filling procedures. The suppression correction is found using a simulation that contains a 5% constant v_2 level over the entire pseudorapidity range. The Monte Carlo samples are produced with the same Spectrometer magnetic field setting as found in the data. Consequently, the 19.6, 62.4, and 200 GeV samples are generated with no magnetic field, while the 130 GeV sample contains a mix of magnetic field samples that proportionally match the data. The suppression correction is found by running the analysis over the MC sample in the same way as it was done with data. In addition, the bad channel map from the data is copied into the MC analysis at the same energy and corrected to give a more realistic suppression correction. The main contributor to the suppression is the percentage of bad channels for each data set. Those with more bad channels (19.6 and 200 GeV) had a larger suppression than those with fewer bad channels (62.4 and 130 GeV).

The suppression correction is found by dividing the resolution-corrected v_2 that is reconstructed from the sample by the true 5% input level in each bin of pseudorapidity. The correction is applied to the data by dividing the resolution-corrected v_2 from the data by the suppression correction in each η bin. This is the final step in producing the central value of the elliptic flow result in each pseudorapidity bin. Fig. 5.3 shows the suppression level for each energy.

The event plane distributions shown in Fig. 5.1 exhibit some structure, particularly at 19.6 GeV. An ideal analysis would yield flat distributions since the reaction plane orientation is random over the entire azimuth on an event-by-event basis. A flat distribution would show that the analysis is completely immune to azimuthal biases due to detector effects or other factors. Note, however, the reconstructed event planes show the same structure in both the data and Monte
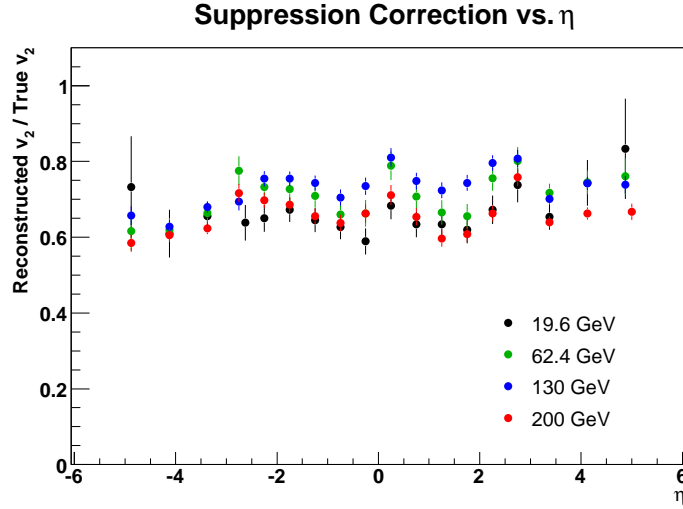
Figure 5.3: The suppression correction as a function of pseudorapidity, averaged over the 40% most central collisions at each energy.

Carlo samples. It is therefore likely that the suppression correction from the MC corrects for these effects. Fig. 5.4 shows a data and MC comparison for the event plane distributions at 19.6 GeV. Similar agreement between data and MC was found at all energies.
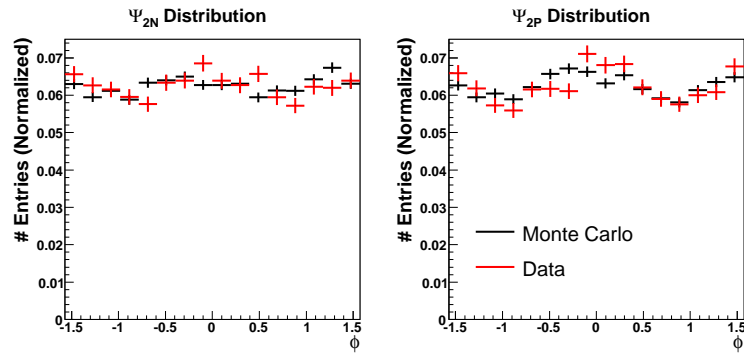
Figure 5.4: Comparison of data and Monte Carlo Ψ_2 event plane distributions at 19.6 GeV over the 0-40% centrality range. Both samples have been event normalized.

Other MC samples are studied to verify the analysis and establish the system-

atic errors. A centrality dependent, triangular-shaped v_2 is also used to find the
suppression correction and to confirm that a triangular shape can be reconstructed
with the analysis method. The input flow equation for this sample is

$$v_2(\eta) = b \times 0.01 \times (1 - |\eta|/6) \qquad (5.1)$$

where b is the impact parameter, which varies over a range of 0-30 fm. Fig. 5.5
shows the reconstructed flow signal compared to the true signal found in triangular
MC. Using this sample to find the suppression correction gives results that are
consistent with the flat 5% MC, as shown in the systematic error plots shown
below in Figs. 5.7- 5.10.

Triangular Monte Carlo Sample - 130 GeV
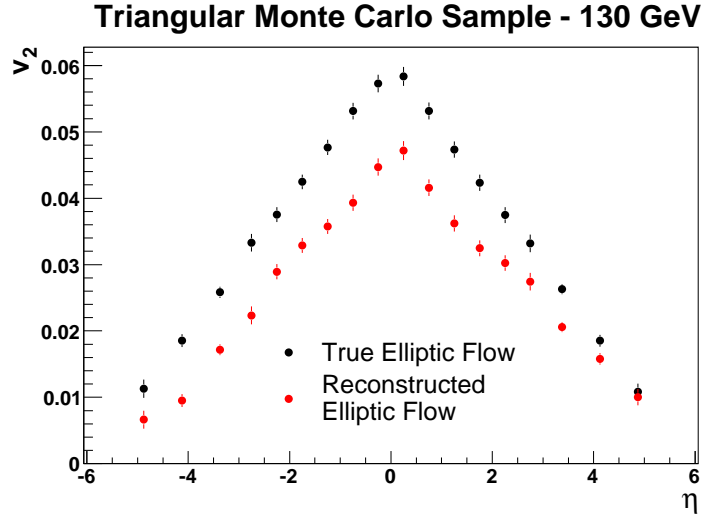
Figure 5.5: Reconstructed triangular MC averaged over the 0-40% centrality range
as a function of pseudorapidity at 130 GeV. The true input v_2, averaged over the
same centrality range, is overlaid. Only the resolution correction is applied to the
reconstructed signal.

Another MC sample contains no flow and is produced by simply randomizing
the azimuthal angle of the tracks of the produced particles. This sample is used

to verify that no spurious flow is produced in the analysis, particularly at high pseudorapidities where multiplicity is low and secondary production is high. Since a sample with no flow has no reaction plane sensitivity, the reconstructed v_2 is calculated with the true reaction plane angle in each event. Fig. 5.6 shows the reconstructed signal at 200 GeV using this method. The other energies yield similar results.
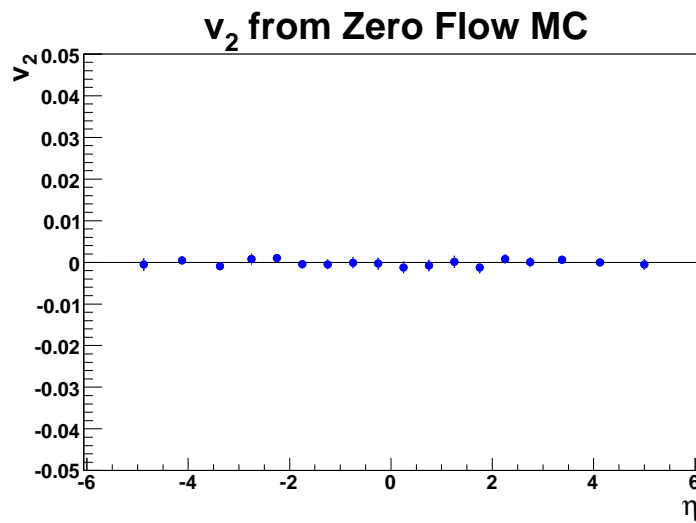
Figure 5.6: Reconstructed zero flow MC averaged over the 0-40% centrality range as a function of pseudorapidity at 200 GeV. v_2 is calculated using the true reaction plane, and the suppression correction from the 5% flat MC sample is applied. The statistical errors are mostly smaller than the data point size.

5.3   Systematic Errors

As mentioned in Ch. 4, the systematic errors are found by varying an analysis parameter with respect to the normal setting for many different parameters. The deviations from the baseline result are typically added together in quadrature to establish the upper and lower bounds of the systematic error in the final result. The spirit of this calculation is to produce a conservative 90% confidence level systematic error that is shown in addition to the 1σ statistical error bars. Some parameters only contribute in one direction to the upper or lower systematic error bound if it is obvious that the variation will only contribute to the deviation in one direction. Most parameters contribute equally to the upper and lower bound.

The parameter under study is varied in both the data sample as well as the MC suppression sample for all four energies, in order to get a new v_2 to compare to the baseline signal. Table 5.1 outlines the systematic contributions, and how they are varied with respect to the baseline analysis.

Table 5.1: Outline of systematic sources studied. (Continued on next page.)

Parameter	Baseline Setting	How Varied and Used
Hit Energy Definition	50 keV	Take the avg. of the absolute values of 40 and 60 keV.
Subevent definition	Use subevents $0.1 \leq |eta| \leq 3.0$	$0.5 \leq \eta \leq 3.0$, $1.0 \leq \eta \leq 3.0$, and $2.6 \leq \eta \leq 3.0$ (for 62.4, 130, and 200 GeV). Average the 0.5-3 and 1-3 subevent deviations, then add 1/2 of the σ of the v_2 from 2.6-3 (for 19.6 GeV, 2.6-3 resolution is poor, so just avg. 0.5-3 and 1-3 subevents).
Beam Orbit Cut	Use events within 2σ of $\langle x \rangle$ and $\langle y \rangle$ vertex positions	Take the maximum between the 1.5 and 3σ average and the deviation from the standard event selection with no beam orbit cut sample.
Suppression Correction	Determine from 5% flat v_2 MC	Determine from triangular v_2 MC. The contribution from each N Ring is averaged together and applied to each point (same with P Rings), Octagon: just use each point.
Common Mode Noise Flag in Oct Sensors	Ignore Flag	Correct sensors that are flagged using bad channel correction method.
Bad Channel Correction	Use Standard Method From Ch. 4	Use Method From [15].
Weighting Matrix	Standard bin	W.M. found in 2 bins of centrality and 10 cm Z vertex bins.

Parameter	Baseline Setting	How Varied and Used
Occupancy Correction	Standard bin	Use Oct bin: 0.5 η by 9 rows, and Ring bin: 4 cols by 9 rows.
Spectrometer Hole Filling	Standard bin	Use bin: 30 cols by 2 rows, 5 cols by 4 rows.
v_2 symmetry in η reflection	N/A	Reflect v_2 about $\eta = 0$
Non-flow background parameter	N/A	Add a factor of 6% of each v_2 value in the Octagon ($|\eta| \leq 3$), 8% in the Rings at $|\eta| \approx 3.4$, 11% in the Rings at $|\eta| \approx 4.2$, 15% in the Rings at $|\eta| \approx 4.9$.
Smoothing parameter due to incorrect dN/dη shape in MC	N/A	Add a factor of $v_2 - \sqrt{(v_2)^2 - X^2}$ at each point, where X is 0 for N Rings, 0.001325 for negative Oct, 0.002175 for positive Oct, 0.001567 for P Rings. (The calculation leads to only a negligible contribution to the systematic error).

Figs. 5.7- 5.10 show the reconstructed elliptic flow signal for each systematic parameter studied. The deviations from the baseline are added together in quadrature to give the systematic error boxes that are shown for each energy. All sources contribute equally to the upper and lower bounds of the box, except for the η reflection symmetry requirement, which only contributes in the direction that it deviates from the baseline result. The width of each systematic box corresponds to the width of the pseudorapidity bin for each data point.
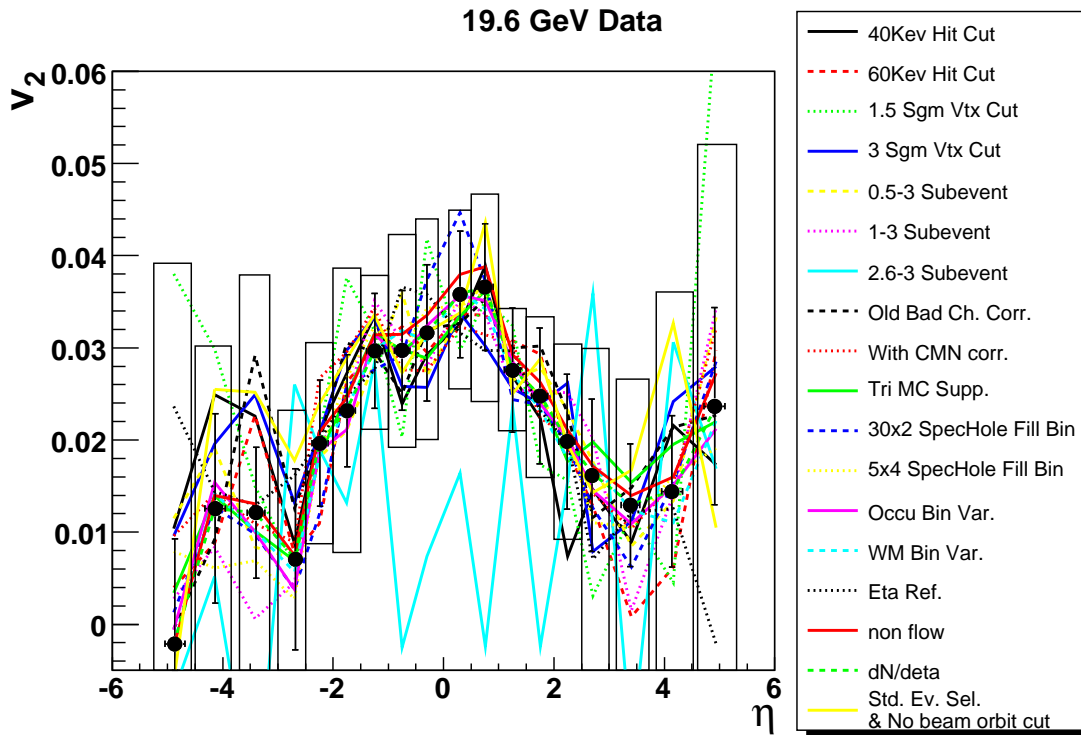
Figure 5.7: Sources of systematic errors at 19.6 GeV. The various lines represent a calculated v_2 where an analysis parameter has been varied with respect to the baseline analysis. All the deviations are added together in quadrature to give the systematic error box for each point. The 2.6-3 subevent systematic is not used, since the multiplicity in this subevent is too small at 19.6 GeV to give a reasonable result.
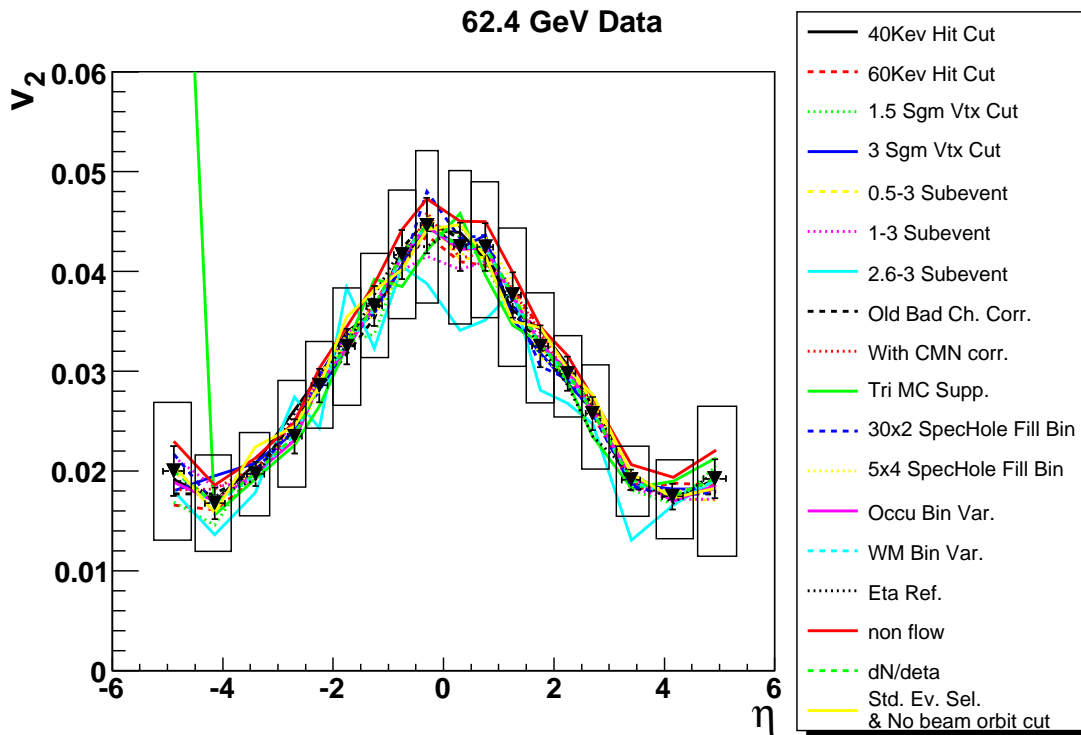
Figure 5.8: Sources of systematic errors at 62.4 GeV as well as the calculated systematic error boxes for each point. The triangular MC deviation at the most negative η point is omitted from the systematic calculation since it is a spurious result, and the average of the deviations from the two neighboring points are used in its place.
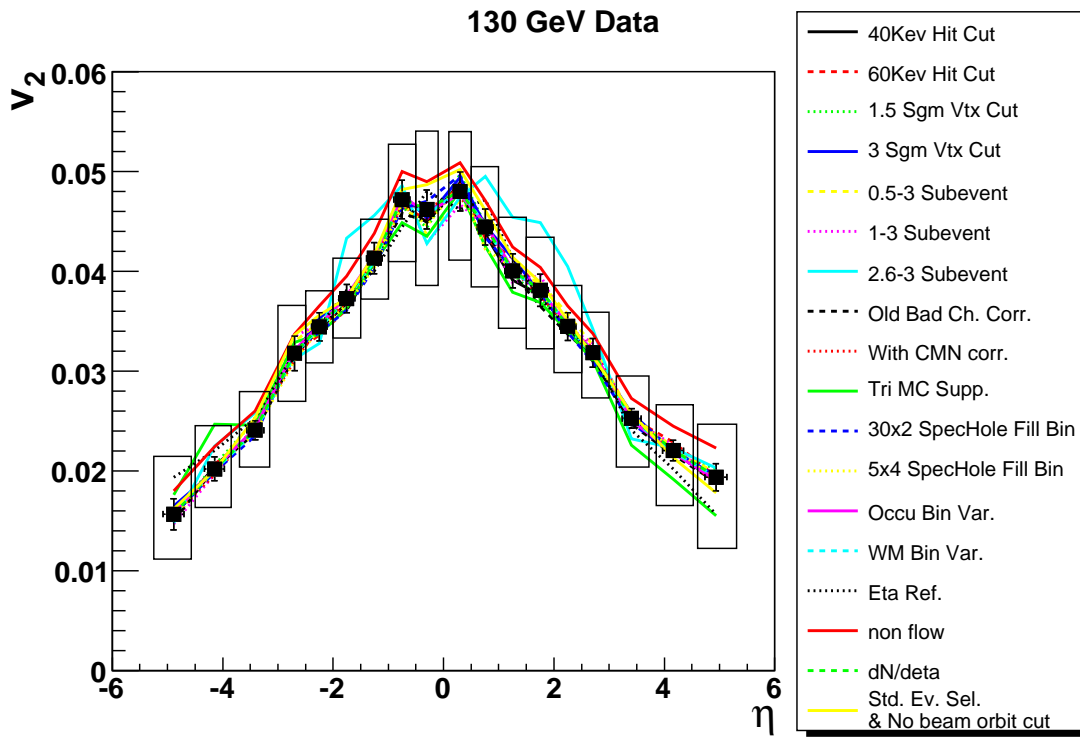
Figure 5.9: Sources of systematic errors at 130 GeV as well as the calculated systematic error boxes for each point.
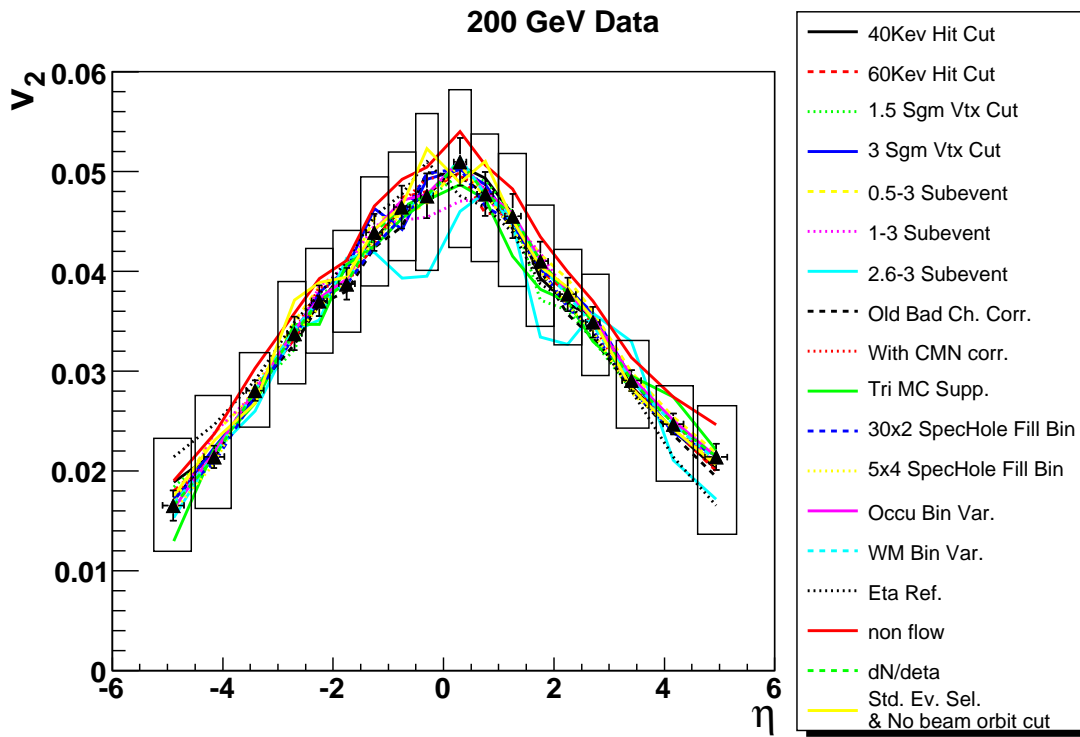
Figure 5.10: Sources of systematic errors at 200 GeV as well as the calculated systematic error boxes for each point.

5.4 Reaction Plane Flattening Procedure and Comparison to Baseline Results

An additional study is done to gauge the effect of how a non-flat event plane distribution affects the final v_2 result. A reaction plane flattening algorithm is applied according to [36] in order to make the event plane distribution completely flat. Here, a correction is applied to the each event plane on an event-by-event basis such that

$$\Psi_2^{'} = \Psi_2 + \Delta\Psi_2, \tag{5.2}$$

where the correction factor $\Delta\Psi_2$ is defined as

$$\Delta\Psi_2 = \Sigma_n[A_N cos(n\Psi_2) + B_N sin(n\Psi_2)]. \tag{5.3}$$

Requiring the corrected event plane distribution to be flat means that the nth Fourier moment vanishes. The coefficients A_n and B_n can be evaluated from the original distribution

$$B_n = \frac{2}{n}\langle cos(n\Psi_2)\rangle, \tag{5.4}$$

$$A_n = -\frac{2}{n}\langle sin(n\Psi_2)\rangle, \tag{5.5}$$

where the angular brackets denote averaging over all events.

The corrected event plane angle is then

$$\Psi_2^{'} = \Psi_2 + \Sigma_n \frac{2}{n}[-\langle sin(n\Psi_2)\rangle cos(n\Psi_2) + \langle cos(n\Psi_2)\rangle sin(n\Psi_2)]. \qquad (5.6)$$

Fig. 5.11 illustrates the event plane distributions at 19.6 GeV before and after the correction is applied. The event planes shown were corrected up to $n = 64$. Even with the extremely flat event plane distributions, the resolution correction is
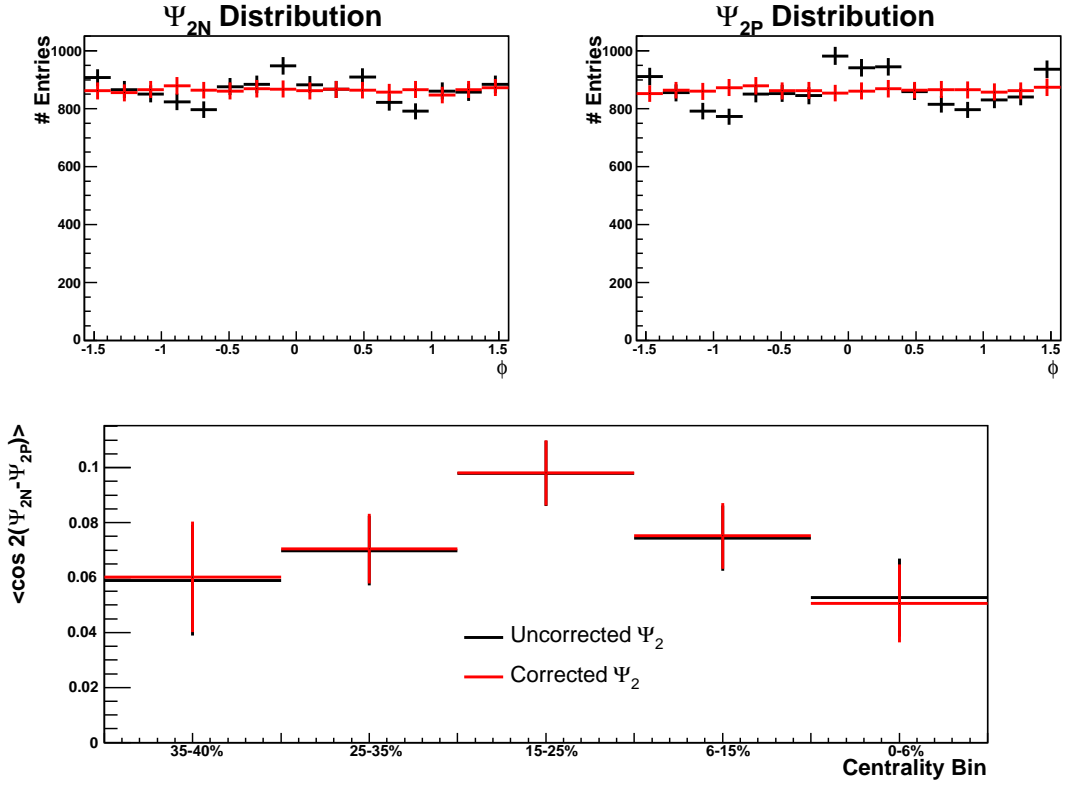
Figure 5.11: Comparison of corrected and uncorrected event plane distributions at 19.6 GeV for the 40% most central collisions. The event plane correlation is also shown for the corrected and uncorrected cases.

nearly unchanged, which is also shown in Fig. 5.11. The difference in the elliptic flow before and after the correction is also barely discernible, as shown in Fig. 5.12.

The results of the flattening study are shown here at 19.6 GeV since the event plane distributions exhibited the most structure at this energy and, presumably, would lead to the most biased analysis. Similar results are obtained at the other energies. This agreement adds confidence that the suppression correction takes out any biases in the data since the data and MC event planes contain the same structure, as was shown in Fig. 5.4.

Since finding the correction parameters for the flattening algorithm requires an additional pass through the data, and the difference in the final result is minimal, the event plane flattening algorithm described here is not used to get the baseline results.
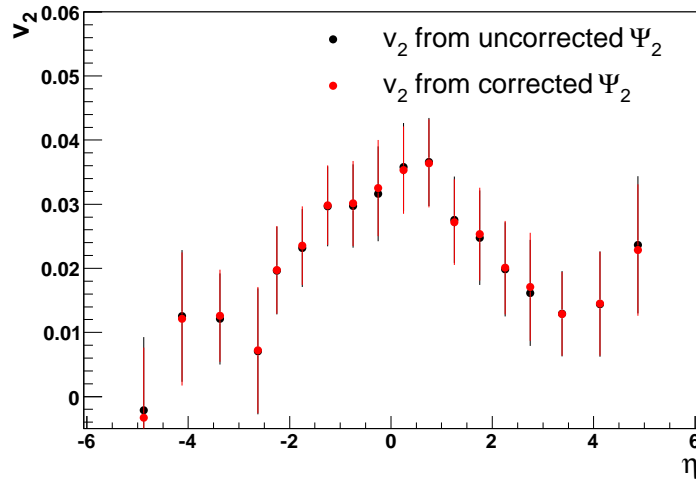
Figure 5.12: v_2 vs. pseudorapidity at 19.6 GeV for the 40% most central collisions, calculated with corrected and uncorrected event planes.

5.5   Pseudorapidity Dependence of Elliptic Flow

The pseudorapidity dependence of the elliptic flow for charged particles at the four collision energies is shown in Fig. 5.13 [37]. The results are shown for the 40% most central collisions.
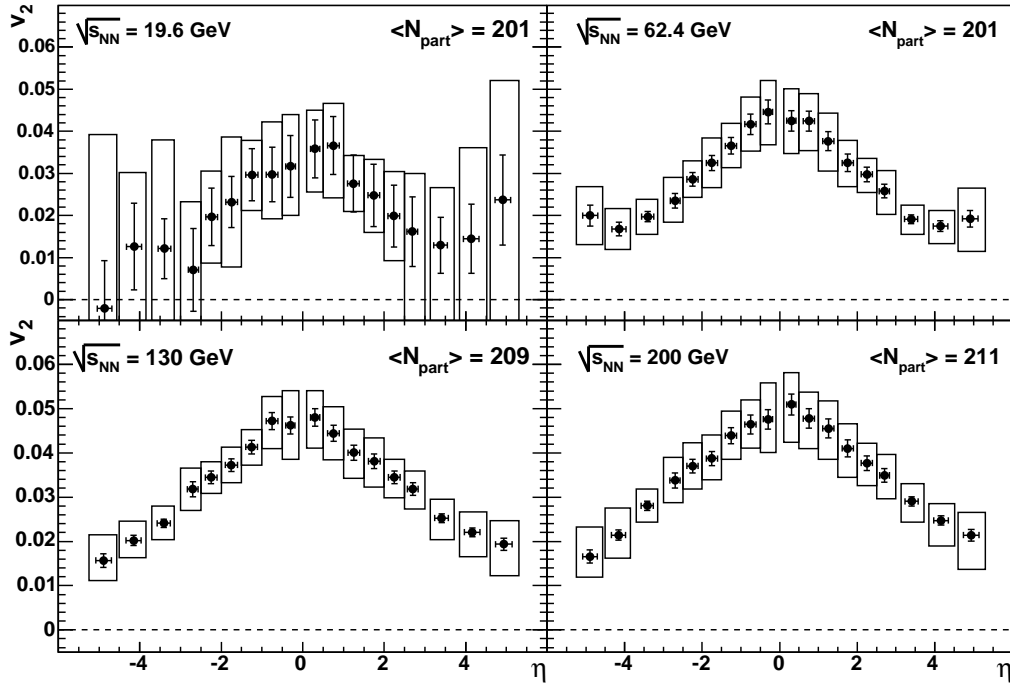
Figure 5.13: v_2 vs. pseudorapidity averaged over all charged particles in the 0-40% centrality range. The average number of participants, $\langle N_{part} \rangle$, is shown for each energy. The lines represent the 1σ statistical errors, and the boxes represent the 90% confidence level systematic errors.

The vertical lines represent the 1σ statistical errors. The errors are somewhat correlated point-to-point since neighboring points are calculated using a common event plane and reaction plane resolution parameter. The boxes represent the 90% confidence level systematic error boxes. The average number of participants for each energy is shown as well.

The 19.6 GeV sample is made up of a relatively small number of events and also contains a smaller multiplicity in each event. This, in turn, limits the statistical power of the result. Furthermore, the systematic errors are large because it is difficult to separate systematic and statistical effects.

All four energies exhibit a roughly triangular-shaped v_2 that peaks at midrapidity. The results are consistent with previous results in the common pseudorapidity and energy ranges [15, 24]. Fig. 5.14 gives the comparison between these results and earlier results shown by the PHOBOS and STAR collaborations. The PHOBOS results in Fig. 5.14 were produced with the SymOct analysis.
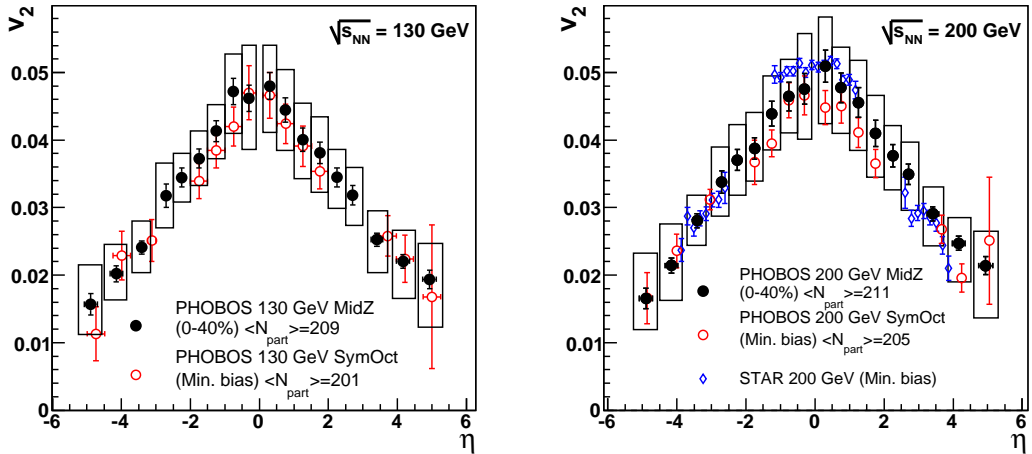
Figure 5.14: (Left panel) v_2 comparison to a previous PHOBOS result at 130 GeV [15]. (Right panel) v_2 comparison to previous PHOBOS and STAR results at 200 GeV [24].

At 19.6 and 62.4 GeV, the v_2 appears to level off or even rise at high $|\eta|$. This could be due to the large directed flow at high $|\eta|$ or the presence of spectator matter. At the higher energies, the directed flow is smaller and the spectator matter is pushed farther out in pseudorapidity.

5.6 Hydrodynamic Comparisons to Elliptic Flow Results

As mentioned in Ch. 1, comparisons of RHIC data to hydrodynamic calculations have been key in understanding the state of matter created. Early hydrodynamic calculations predicted the observed elliptic flow at midrapidity of 130 and 200 GeV collisions (as shown, e.g., in Fig. 1.9), but not away from midrapidity. Recently, theorists have employed a hybrid model that includes ideal hydrodynamics during the early stages of the collision and a later hadronic stage with dissipative effects to explain the falloff of v_2 with pseudorapidity [18]. Results from this model give better qualitative agreement to flow measurements than previous models and seem to show that "late viscosity" in the dissipative hadronic phase of the collision could explain the difference between ideal hydrodynamic calculations and the observed data.

An alternate model, known as the Buda-Lund hydrodynamic model [38] uses a three dimensional hydrodynamic calculation based on an expanding ellipsoidal source. The model ultimately produces a formula describing the pseudorapidity dependence of elliptic flow that can be fit to the data at each collision energy. The results are shown in Fig. 5.15 along with the PHOBOS data from Fig. 5.13. The Buda-Lund model gives good agreement with the PHOBOS elliptic flow results, indicating that the perfect fluid may extend well beyond midrapidity and down to lower collision energies.
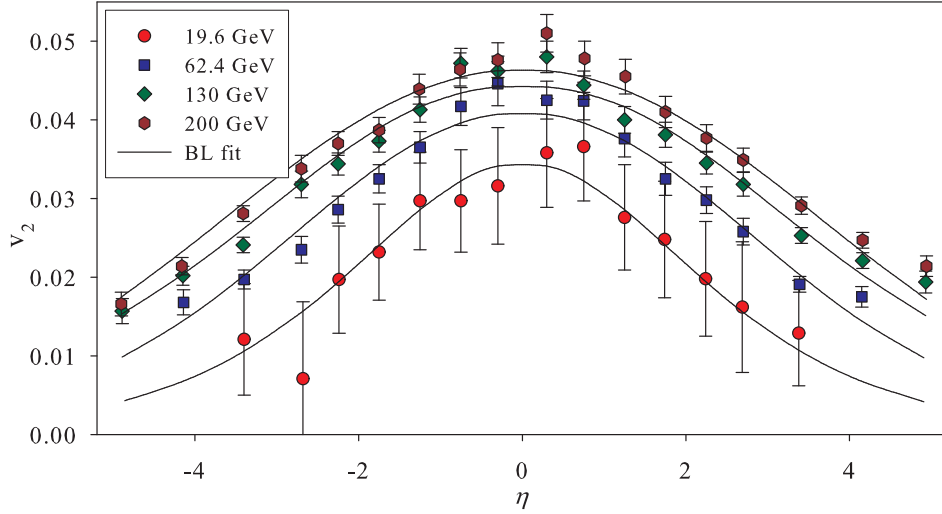
Figure 5.15: Comparison of the PHOBOS elliptic flow results from Fig. 5.13 compared to a calculation from the Buda-Lund hydrodynamic model. From reference [38].

5.7   Energy Dependence of Elliptic Flow

Fig. 5.16 shows v_2 as a function of collision energy. The v_2 values are averaged within the $|\eta| < 1$, $1 < |\eta| < 2$, $2 < |\eta| < 3$, and $3 < |\eta| < 4.5$ bins of pseudorapidity. The lines represent fits to the data. It is evident that v_2 exhibits a linear dependence with the logarithm of the beam energy.

5.8   Extended Longitudinal Scaling of Elliptic Flow

It is interesting to look at the energy dependence of the flow signal as a function of pseudorapidity by removing the differing beam boosts from the problem. This is done by shifting to the approximate frame of reference of one of the colliding nuclei. This comparison of v_2 across energies as a function of pseudorapidity is reminiscent
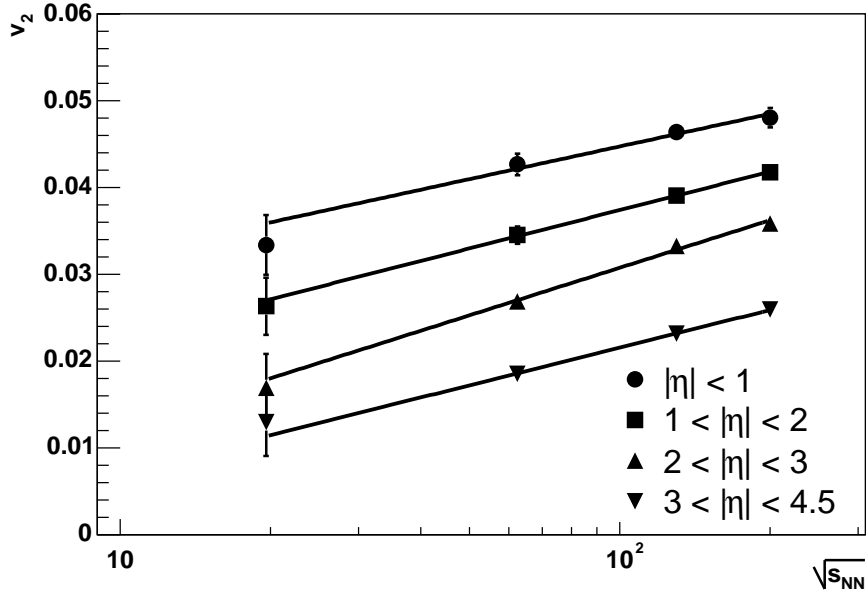
Figure 5.16: v_2 vs. $\sqrt{s_{NN}}$ averaged within the $|\eta| < 1$, $1 < |\eta| < 2$, $2 < |\eta| < 3$, and $3 < |\eta| < 4.5$ bins of pseudorapidity. The lines represent fits to the data.

of the concept of limiting fragmentation for particle multiplicity. The hypothesis of limiting fragmentation [39] states that particle production, when studied in the rest frame of one of the colliding nuclei, will reach a limiting distribution regardless of the energy of the projectile nucleus. Limiting fragmentation results were first shown at RHIC energies by BRAHMS [40] and later by PHOBOS [19] for the charged-particle multiplicity.

Fig. 5.17 shows the elliptic flow plotted as a function of $\eta + y_{beam}$ (top panel) and $\eta - y_{beam}$ (bottom), where y_{beam} is calculated according to Eq. 1.2. This effectively shows the pseudorapidity distribution of v_2 in the reference frame of one of the nuclei and then the other. For clarity, only the statistical errors are shown. The highest $|\eta|$ points at 19.6 GeV have been left off this plot and the following figure since they lack significance due to large systematic errors.
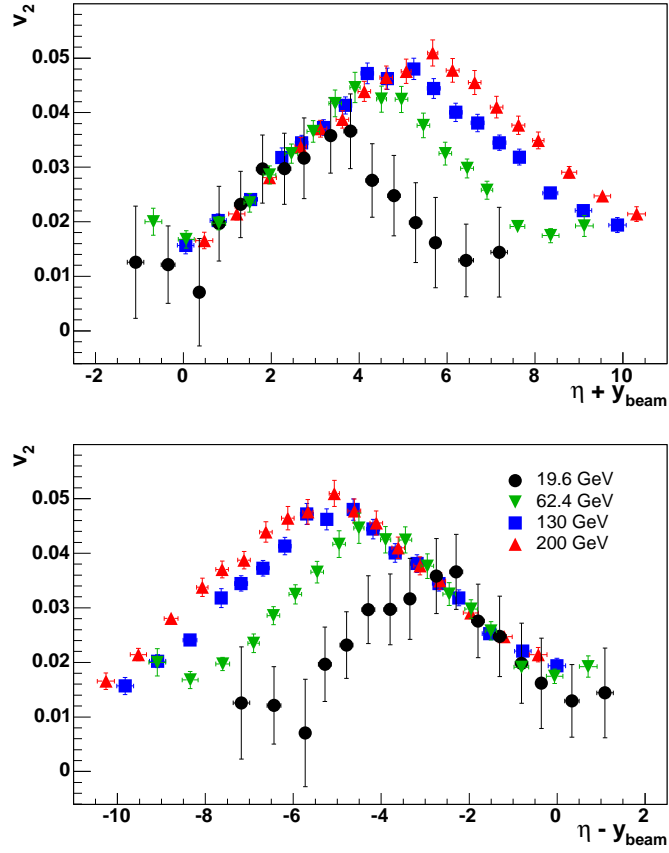
Figure 5.17: v_2 vs. $\eta + y_{beam}$ (top panel) and $\eta - y_{beam}$ (bottom panel) in the 0-40% centrality region. The systematic errors have been left off for clarity.

The results show that limiting fragmentation holds for elliptic flow in a region well beyond what is commonly know as the fragmentation region. For this reason, the PHOBOS collaboration has chosen to call this phenomenon extended longitudinal scaling.

Because rapidity is Lorentz invariant, it would be best to use rapidity (y) rather than pseudorapidity (η) in order to investigate the extended longitudinal scaling of elliptic flow. Unfortunately, this is not possible with the PHOBOS multiplicity array. Our estimates show that the differences between working in η

instead of y are small ($< 20\%$ at 19.6 GeV and $< 10\%$ at 200 GeV) and does not change the qualitative feature of the shapes. These estimates are based on a data-driven model of dN/dy, $\langle p_T \rangle$, and $v_2(p_T)$ from RHIC and CERN Super Proton Synchrotron data [41]. A similar conclusion has been reached by others [42].

Fig. 5.18 shows the elliptic flow, as given in Fig. 5.13, plotted as a function of $\eta' = |\eta| - y_{beam}$, where the data points have been folded about midrapidity and averaged together before being shifted by y_{beam}. The four curves scale through the entire region of η' overlap, all the way through midrapidity. The observed linear scaling implies the triangular shape of v_2 in Fig. 5.13 as well as the linear evolution of $v_2(ln\sqrt{s_{NN}})$ shown in Fig. 5.16.
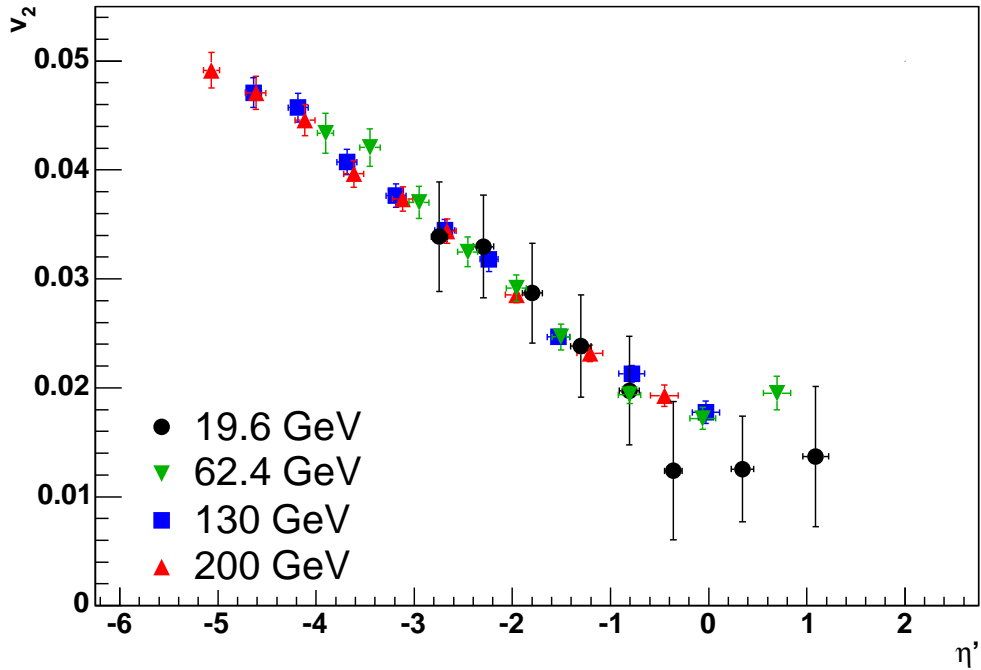
Figure 5.18: v_2 vs. $\eta' = |\eta| - y_{beam}$ shown for all four energies in the 0-40% centrality region.

Chapter 6

Directed Flow

6.1 Problems with the Standard Event Plane Technique: Momentum Conservation Correlations

The measurement of the directed flow parameter, v_1, at RHIC energies involves several subtle difficulties not present in measurements of elliptic flow. Over most of the rapidity range at these collision energies, the directed flow signal is much smaller than the elliptic flow signal. In fact, the directed flow signal is constrained to be zero at midrapidity. Though that constraint only exists at mid-rapidity, the signal at higher energies is fairly flat and small in a broad region of η near midrapidity. This means the high-multiplicity midrapidity region does not make a useful subevent with which to find an event plane. The directed flow signal is strongest in the high-$|\eta|$ regions, so the best place to find an event plane is in the Rings region. However, measuring directed flow by using an event plane analysis

similar to the procedure used for elliptic flow produces non-flow correlations, as shown below.

Fig. 6.1 shows the directed flow measured from a standard event plane analysis where event planes are found in the negative and positive Ring regions (Ψ_{1N}, $-5 \leq \eta \leq -3$ and Ψ_{1P}, $3 \leq \eta \leq 5$). Hits in the negative (positive) pseudorapidity regions are correlated with the Ψ_{1P} (Ψ_{1N}) event plane. The reaction plane resolution correction is found according to Eq. 2.10, and the suppression correction is found from a Monte Carlo sample that contains a constant -3% v_1 for $\eta < 0$ and 3% for $\eta > 0$. This "flat" (or more correctly, step function) MC sample is analogous to the constant 5% v_2 sample that is used to find the suppression in the elliptic flow analysis.

A break at midrapidity is observed at 62.4, 130, and 200 GeV, with the discontinuity being greatest at 200 GeV. The gap is a result of non-flow correlations due to momentum conservation. Since the event planes are found in subevents that reside in the forward and backward η hemispheres, any fluctuation in the $\langle p_T \rangle$ in one hemisphere is also found as a recoil in the other. This produces the back-to-back correlation observed in Fig. 6.1.

There is no discontinuity at 19.6 GeV, presumably because the directed flow signal is much larger at high pseudorapidities where the event plane is found (greater than 10%, shown below) than what is found in the same η range at the other energies. Thus, at 19.6 GeV the large directed flow signal dominates any non-flow correlations, and the increased sensitivity to finding the reaction plane in this η region causes the reconstructed event planes to be less susceptible to momentum conservation effects.
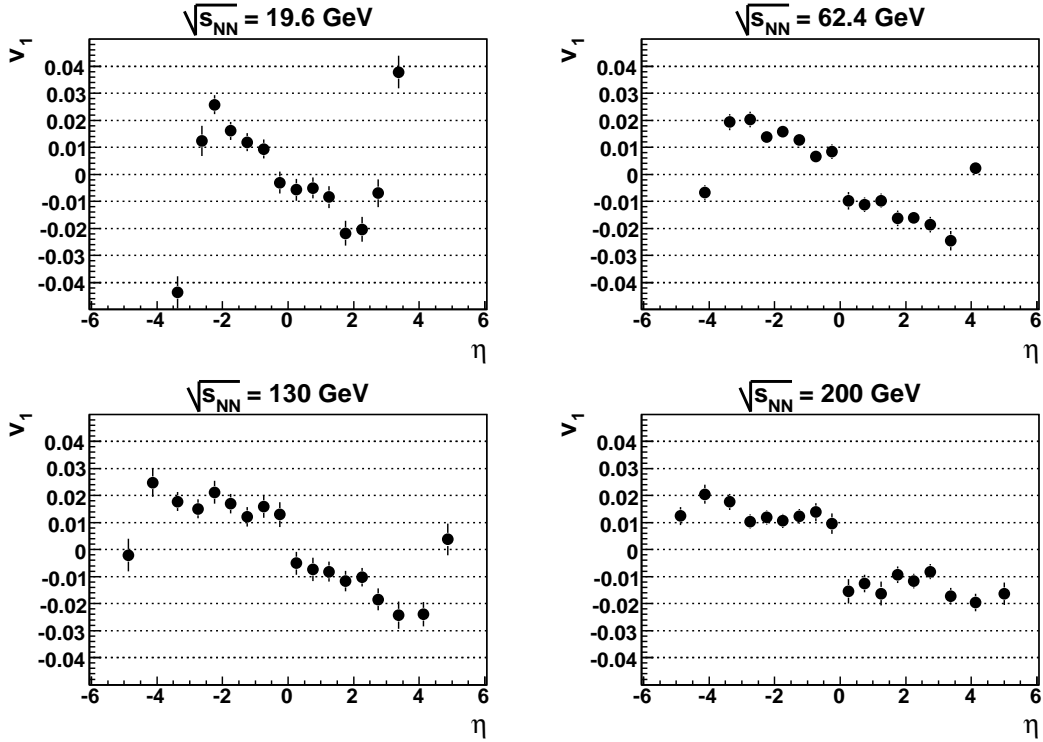
Figure 6.1: Directed flow measured from positive and negative Ring subevents and shown for all four collision energies in the 0-40% centrality range. The vertical scale is fixed at $\pm 5\%$ to illustrate the discontinuity at midrapidity, so the v_1 values at high-η are off the scale at 19.6 and 62.4 GeV.

A similar break at midrapidity was also observed [22] by the NA49 collaboration for Pb+Pb collisions at 17.2 GeV. The fixed target experiment at the SPS calculated directed flow using a similar event plane analysis [44], where the subevents were found in the forward rapidity region. However, it should be noted that the subevents used by NA49, when compared to those used by PHOBOS, are in a region closer to midrapidity ($1.1 \leq y \leq 3.1$) where the directed flow is smaller. They were able to remove the correlation by applying a p_T-based correction [22]. The results from NA49 with and without the correction are shown in Fig. 6.2. It should be noted that unlike PHOBOS at 19.6 GeV, the smaller
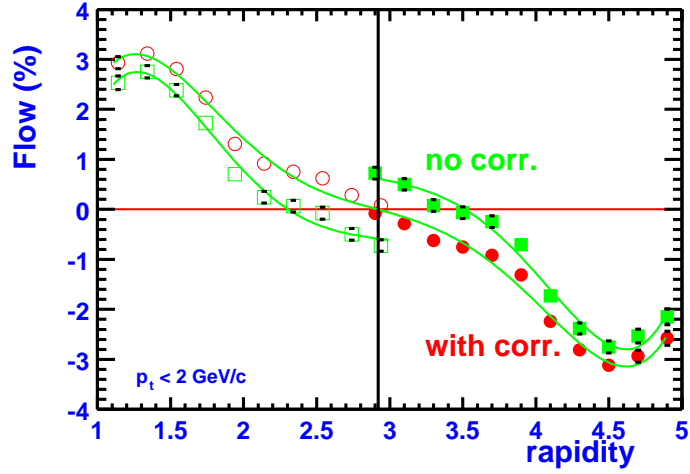
Figure 6.2: Directed flow for charged pions as a function of rapidity at $\sqrt{s_{NN}} = 17.2$ GeV, as measured by the NA49 collaboration [23]. The results are shown with and without the correction for momentum conservation. The open points have been reflected about midrapidity.

rapidity coverage of NA49 does not allow for a choice of subevents in the rapidity range where directed flow is large. Conversely, the PHOBOS detector only allows for p_T determination of detected particles in the Spectrometer detector, so it is not possible to perform a similar correction to the data.

6.2 Symmetric Subevent Method

A new method is used to circumvent the momentum conservation correlations, as outlined in Section 2.7. In this method, a subevent is chosen such that it is centered about midrapidity and contains equal pieces in the forward and backward regions. Any fluctuation in the forward half of the subevent is cancelled out by the recoil in the backward half. The event plane is then free from non-flow correlations. Since the subevent is centered about midrapidity and contains equal halves in the forward and backward η regions, it is dubbed a "symmetric" subevent.
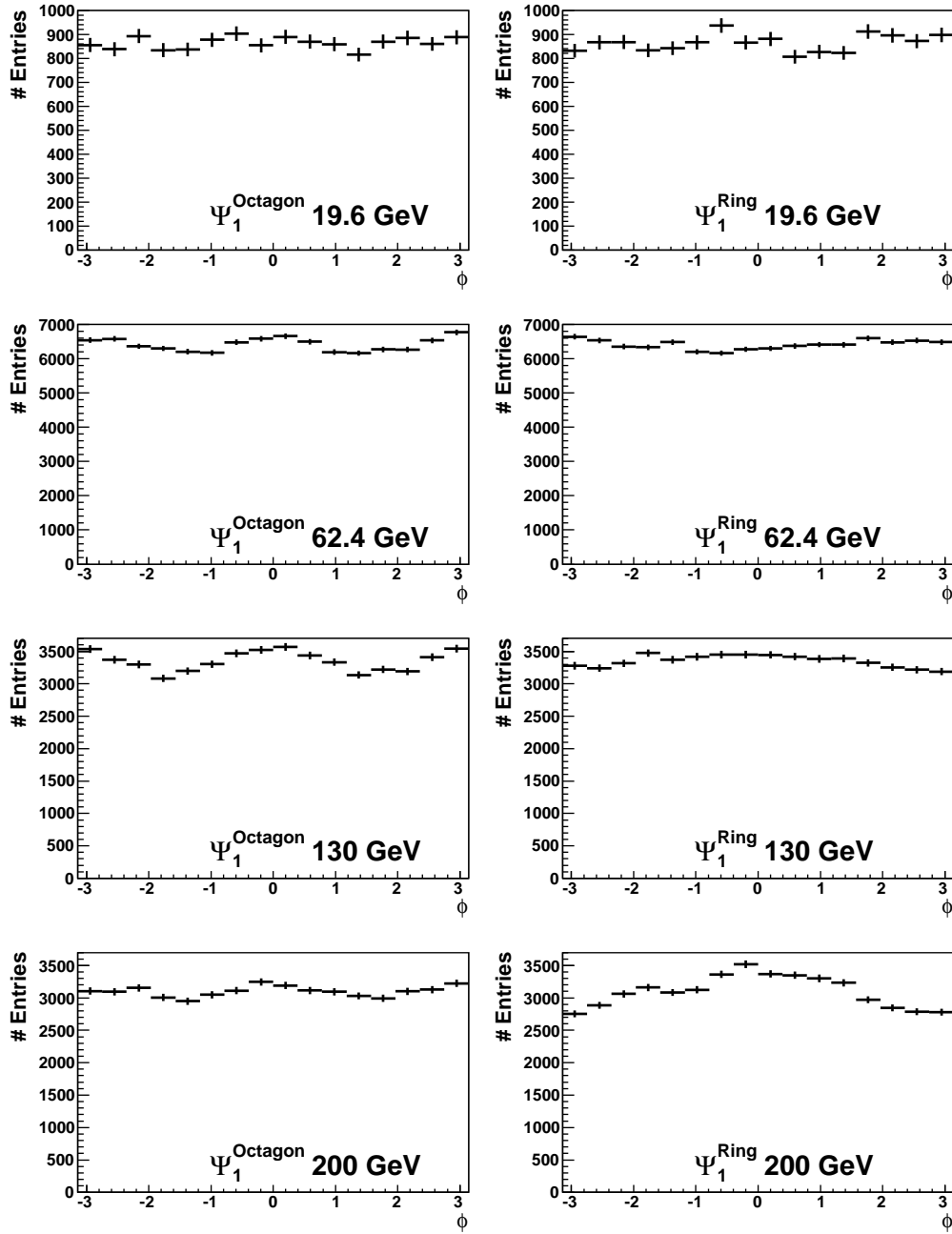
Figure 6.3: Ψ_1 event plane distributions from the Octagon $(1.5 \leq |\eta| \leq 3)$ and Ring $(3 \leq |\eta| \leq 5)$ subevent regions at each collision energy, for the 40% most central events. The error bars represent the square root of the number of entries in each bin.

Two symmetric subevents are needed to measure flow in the entire pseudorapidity region in order to avoid auto-correlations. The subevents in this analysis are in the Octagon, $1.5 \leq |\eta| \leq 3$, and Rings, $3 \leq |\eta| \leq 5$. Fig. 6.3 shows the Ψ_1 event plane distributions in these subevent regions.

The reaction plane resolution is found according to Eq. 2.13. The resolution is a function of event planes found in the negative (Ψ_{1N}) and positive (Ψ_{1P}) η halves of each symmetric subevent. Fig. 6.4 shows the event plane correlation, $\langle cos(\Psi_{1N} - \Psi_{1P}) \rangle$, as a function of centrality for each collision energy.
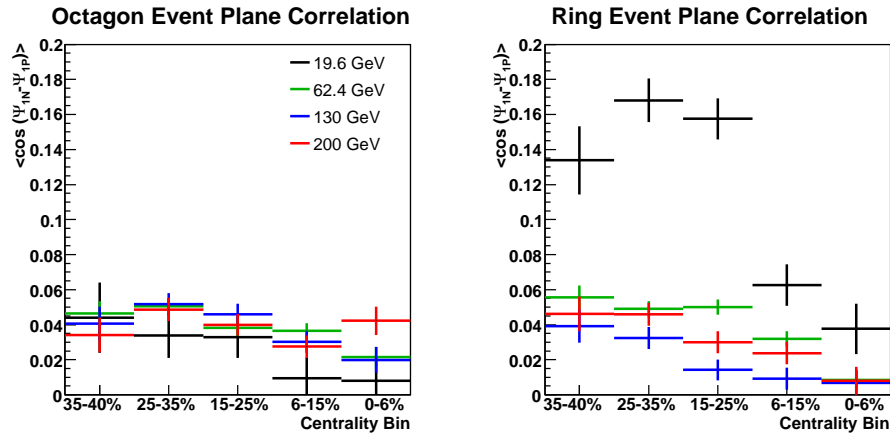
Figure 6.4: Event plane correlations from the Octagon and Ring event planes as a function of centrality for the four collision energies.

It is possible that the non-flow correlation due to momentum conservation could bias the resolution correction since it involves a correlation between event planes that are found in the forward and backward η hemispheres. The results in Fig. 6.4 and in the final v_1 do not appear to show any such correlation, at least not in a form that leads to a discontinuity at mid-rapidity. In addition, the mixed harmonic analysis described in the next section gives consistent results and lends confidence to the symmetric subevent result.

The suppression correction is found using the step function Monte Carlo sample described above. Fig. 6.5 shows the η-dependent suppression correction for each energy.

Figure 6.5: The suppression correction as a function of pseudorapidity for the 40% most central collisions at all four collision energies.

As was found in the elliptic flow analysis, the Ψ_1 event plane distributions found in the data match what is reconstructed in MC. Fig. 6.6 shows the event plane distributions from data and MC at 130 GeV. The similar structures found in both lead us to believe the suppression correction. Similar agreement was found at all energies.

It should be noted that in Fig. 6.6, the event plane structure in the positive octagon subevent ($1.5 \leq \eta \leq 3$) could be an effect of the Spectrometer hole filling procedure, since the pseudorapidity coverage of the Spectrometer holes is mainly in the forward region and located at $\phi = 0$ and $\pm\pi$. The virtual hits could dominate the event plane angle reconstruction since the actual directed flow signal is very small in the Octagon region. However, any effect this event plane distribution

has on the final result appears to be small, given the good agreement between the baseline analysis and one that has undergone the reaction plane flattening procedure, as shown in Section 6.5.
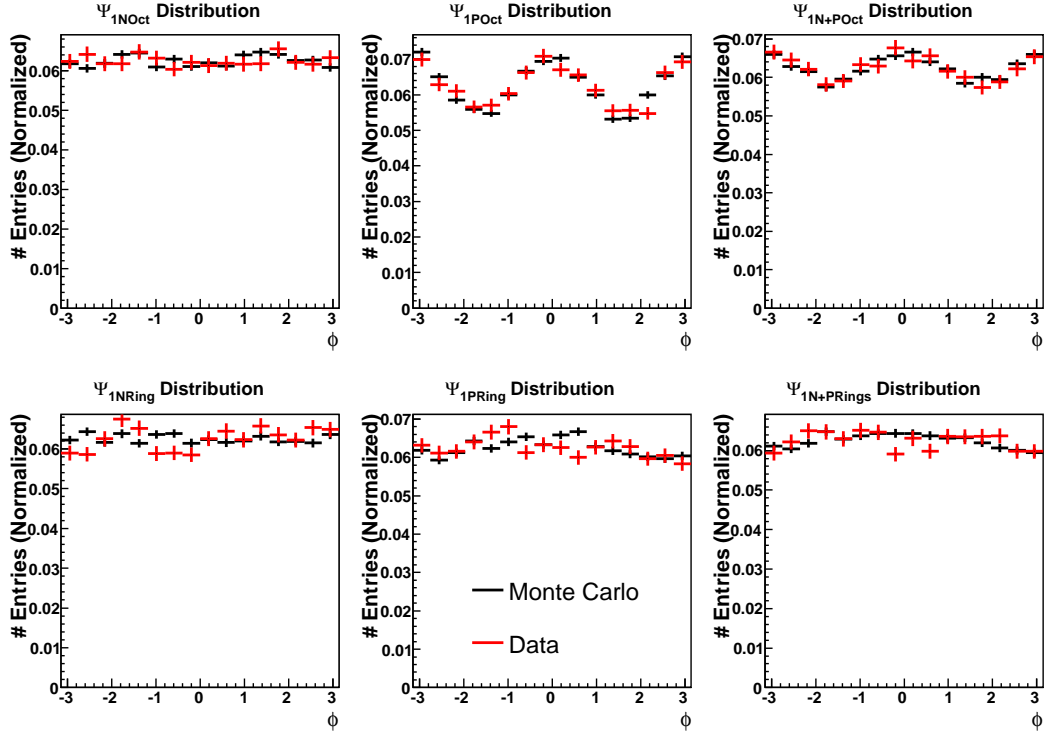
Figure 6.6: The Ψ_1 event plane distributions found in the data and Monte Carlo samples at 130 GeV. Both samples have been event normalized and are shown for the 40% most central events.

6.3 Mixed Harmonic Method

As outlined in Section 2.7, the mixed harmonic analysis uses the symmetric subevent Ψ_1 information in conjunction with the Ψ_2 event plane to eliminate non-flow correlations from the directed flow measurement. The event plane distributions for those used in this analysis are found in Fig. 5.1 and Fig. 6.3. Event-

by-event, hits in the negative η Rings (Octagon) region are correlated with the Ψ_1 from the Octagon (Rings) symmetric subevent and the Ψ_2 from the positive Octagon event plane to get the initial v_1 measurement. Likewise, hits in the positive η Rings (Octagon) region are correlated with the Ψ_1 from the Octagon (Rings) symmetric subevent and the Ψ_2 from the negative Octagon event plane.

Fig. 6.7 shows the event plane correlation from mixed harmonics, $\langle cos(\Psi_{1Oct} + \Psi_{1Ring} - 2\Psi_2)\rangle$, as a function of centrality for each energy. This value is multiplied
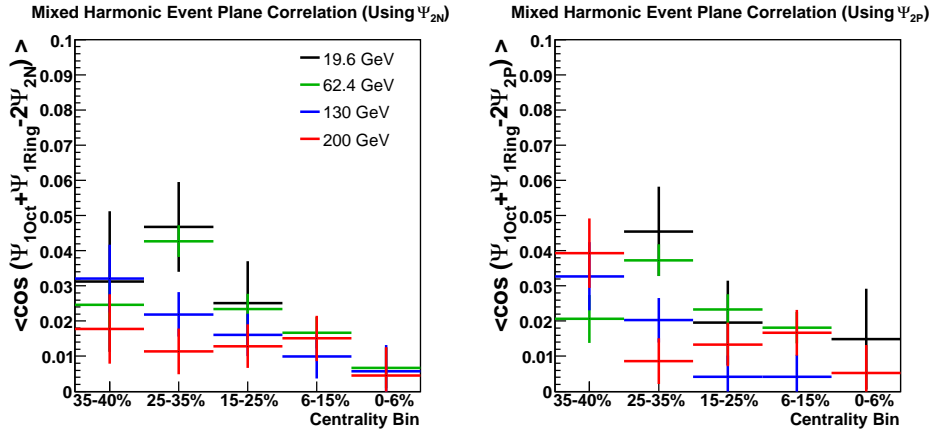
Figure 6.7: Mixed harmonic event plane correlation, $\langle cos(\Psi_{1Oct} + \Psi_{1Ring} - 2\Psi_2)\rangle$, as a function of centrality for the four energies. In the left panel (right) the Ψ_1 event planes are correlated with Ψ_{2N} (Ψ_{2P}).

by the Ψ_2 reaction plane resolution (from Eq. 2.10), and then the square root is taken to give the final resolution correction for the mixed harmonic analysis, as shown in Eq. 2.19. Since the Ψ_{2N} and Ψ_{2P} event planes are used depending on the location of the hit under study, both event plane correlations are shown. The final results are only shown in centrality regions where a positive correlation is given for both cases. This occurs in the 15-35% centrality range for 19.6 GeV and 6-40% for the other three energies.

The suppression correction for the mixed harmonic analysis is determined using a Monte Carlo sample that contains a 5% v_2 signal that is constant in η and a $\pm3\%$ v_1 signal. Fig. 6.8 shows the suppression correction derived from the sample at each energy.
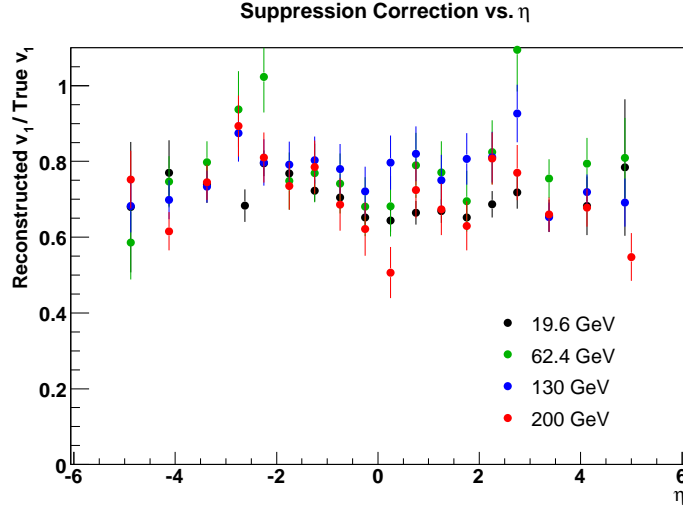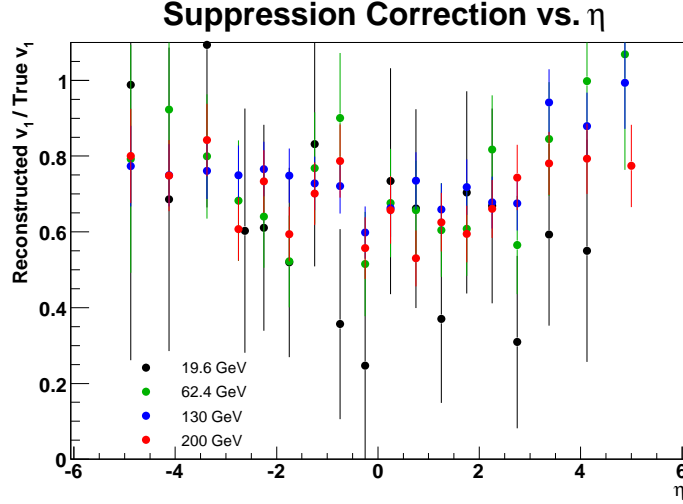

Figure 6.8: Suppression correction as a function of pseudorapidity for the 40% most central collisions at all four collision energies using the Mixed Harmonic analysis.

6.4 Systematic Errors

The systematic errors for the symmetric subevent analysis are calculated at each energy in similar fashion to the elliptic flow analysis. Nearly all sources studied in the elliptic flow analysis are used, and a few more are added in order to achieve a more accurate calculation. Table 6.1 gives the systematic sources studied in the directed flow analysis.

Table 6.1: Outline of systematic sources studied for the symmetric subevent analysis. (Continued on next page.)

Parameter	Baseline Setting	How Varied and Used
Hit Energy Definition	50 keV	Take the avg. of the absolute values of 40 and 60 keV.
Subevent definition	$1.5 \leq |\eta| \leq 3.0$ and $3 \leq |\eta| \leq 5$	Use $1.5 \leq |\eta| \leq 2.5$ and $3.5 \leq |\eta| \leq 5$.
Beam Orbit Cut	Use events within 2σ of the $\langle x \rangle$ and $\langle y \rangle$ vertex positions	Take the maximum between the 1.5 and 3σ average and the deviation from the standard event selection with no beam orbit cut sample.
Common Mode Noise Flag in Oct Sensors	Ignore Flag	Correct sensors that are flagged using the bad channel correction method.
Bad Channel Correction	Use Standard Method	Use Method From [15].
Weighting Matrix	Standard bin	Find a W.M. in 2 bins of cent. and 10 cm z vertex bins.
Occupancy Correction	Standard bin	Use Oct bin: 0.5 η by 9 rows, Ring bin: 4 cols by 9 rows.
Spectrometer Hole Filling	Standard bin	Use bins of 30 cols by 2 rows and 5 cols by 4 rows, average them together.
v_1 symmetry in η reflection	N/A	Multiply v_1 by -1 and reflect about $\eta = 0$.

Parameter	Baseline Setting	How Varied and Used
Mixed Harmonic Result	N/A	Use a 7th order polynomial fit without the even orders, and use that fit line as the deviation from the baseline result.
Zero Flow/Non-flow MC	N/A	Use zero flow MC where the calculation is done with the true reaction plane. If the measured non-zero v_1 is statistically meaningful, i.e. $|v_1| > \sigma(v_1)$, take the deviation as $|v_{1,data} - \sqrt{|v_{1,data}^2 - v_{1,ZeroMC}^2)|}|$ and use it in the lower bound syst. calc.
Extra step for 19.6 GeV only	N/A	For the standard event selection systematic, the deviation for the most positive point is taken as the average of the std. ev. sel. for the most positive and negative points. Likewise the deviation for the second most positive point is taken as the average of second most positive and negative points.
Safety Parameter	N/A	After the sources from the previous steps are added in quadrature, if the upper or lower bound of any syst. error box is less than 0.005 from the point, then the new upper or lower extent of the box becomes 0.005. This smooths the extent of the boxes from point to point.

All sources are added together in quadrature. Most sources are treated sym-
metrically. That is to say, they are assumed to contribute equally to the upper and
lower bound of the box. The sources that only contribute in one direction to the
systematic error box are the η reflection check, mixed harmonic comparison, zero
flow MC, and the safety parameter. As was the case in the elliptic flow analysis,
the width of each systematic box is the width of the pseudorapidity bin for each
data point.

Figs. 6.9- 6.12 show the systematic contributions from each source at the four
collision energies, as well as the calculated systematic error boxes.

Figure 6.9: Sources of systematic errors at 19.6 GeV for the symmetric subevent
analysis, as well as the calculated systematic error boxes for each point.
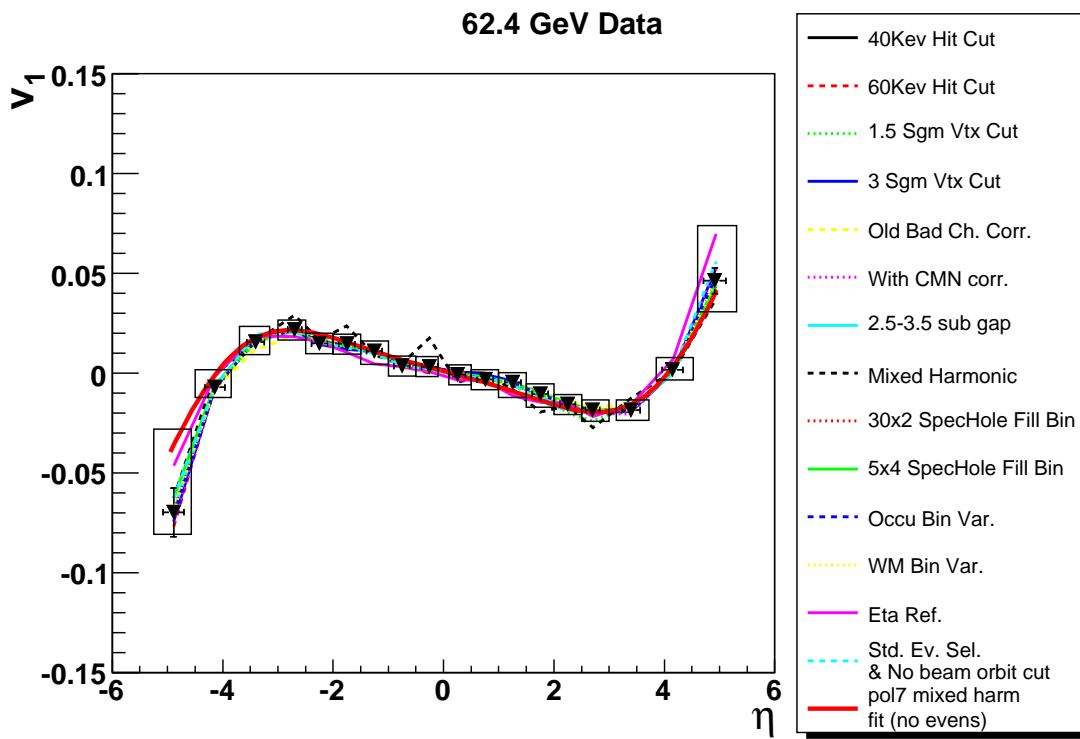
Figure 6.10: Sources of systematic errors at 62.4 GeV for the symmetric subevent analysis, as well as the calculated systematic error boxes for each point.
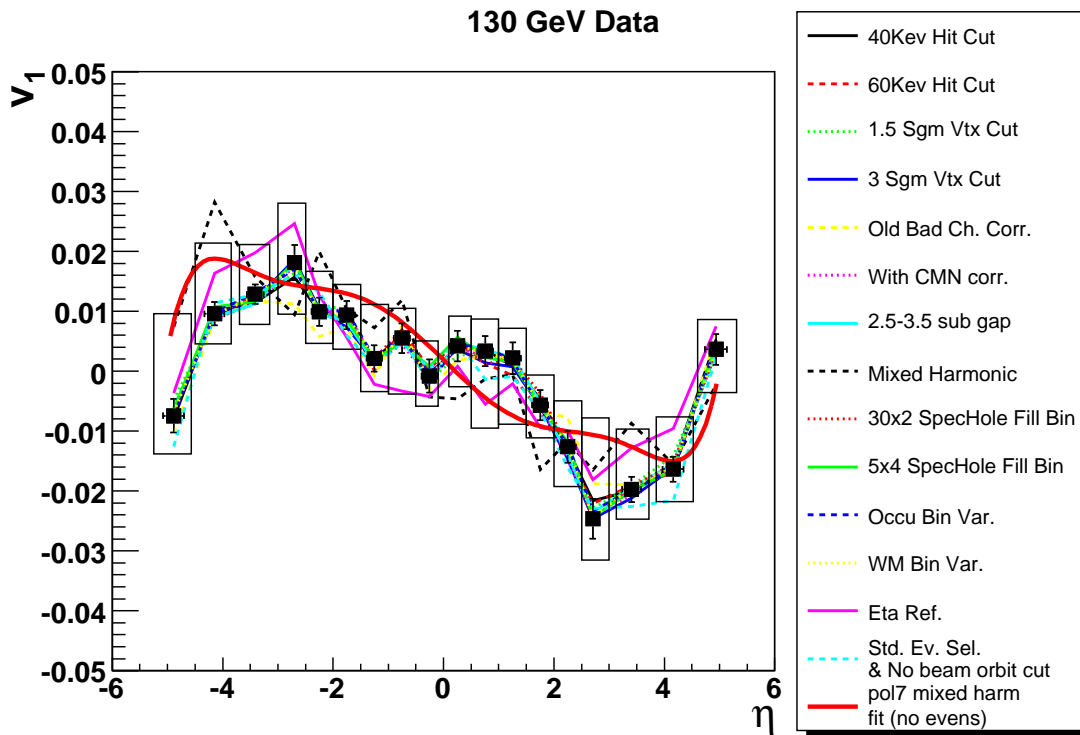
Figure 6.11: Sources of systematic errors at 130 GeV for the symmetric subevent analysis, as well as the calculated systematic error boxes for each point.
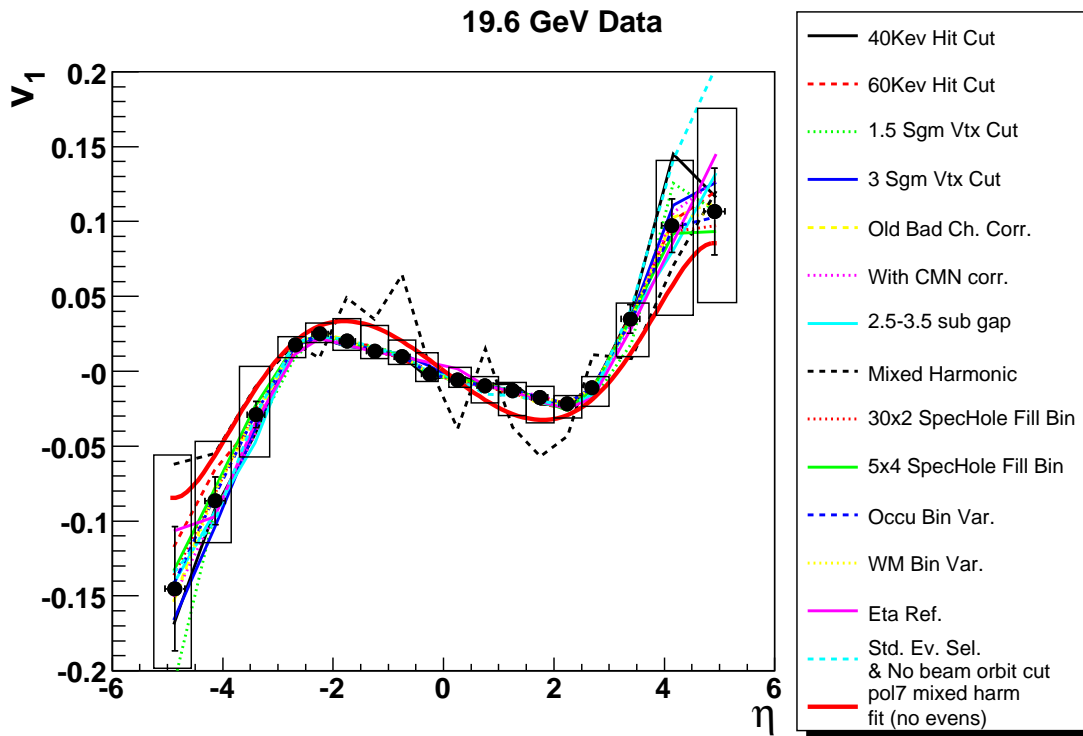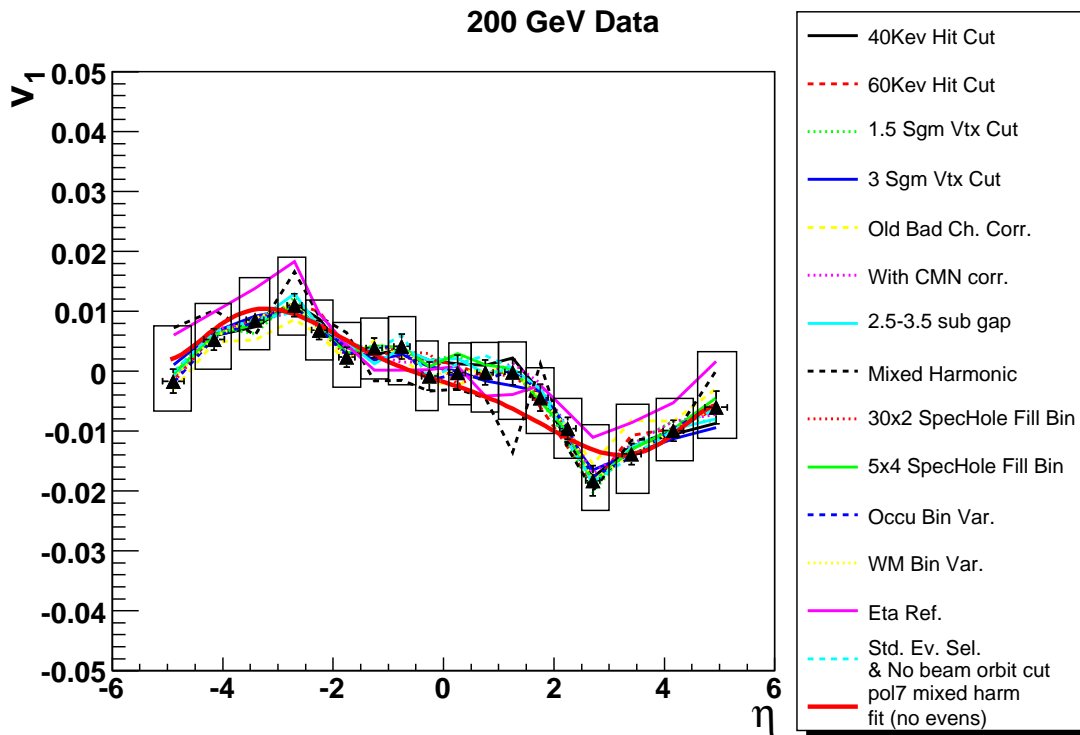
Figure 6.12: Sources of systematic errors at 200 GeV for the symmetric subevent analysis, as well as the calculated systematic error boxes for each point.

6.5 Reaction Plane Flattening Procedure and Comparison to Baseline Results

In order to gauge the effect of non-flat event planes on the directed flow analysis, the reaction plane flattening algorithm that was used on elliptic flow is also used in the directed flow analysis. Fig. 6.13 shows the Octagon event plane distributions as well as the event plane correlation at 200 GeV before and after the correction for the symmetric subevent analysis.
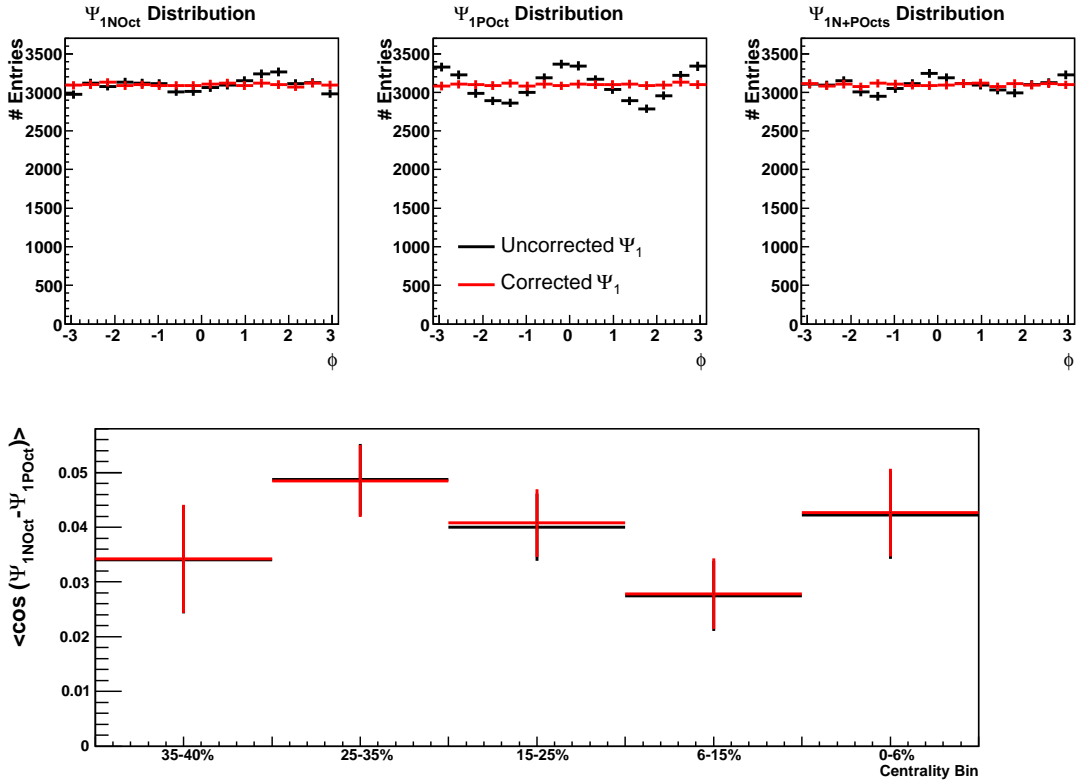
Figure 6.13: Corrected and uncorrected Octagon event planes used in the symmetric subevent analysis at 200 GeV. The event plane correlation is also shown with and without the correction.

Fig. 6.14 shows the Ring event plane distributions as well as the event plane correlation at 200 GeV before and after the correction.
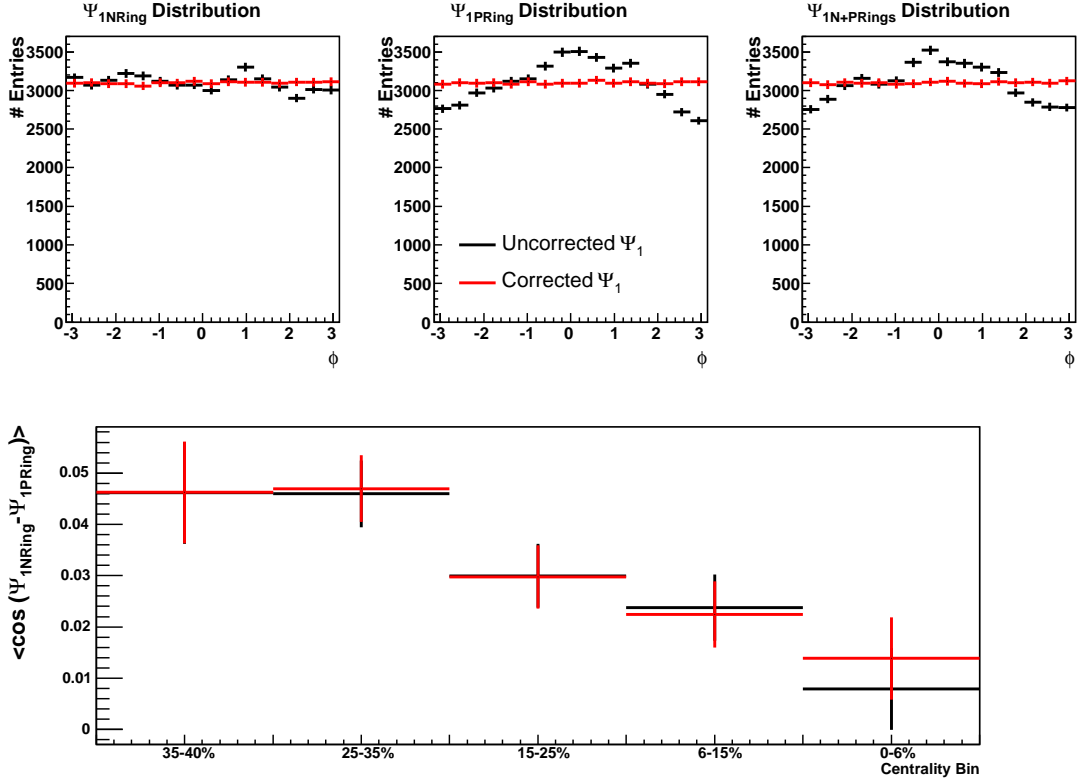
Figure 6.14: Corrected and uncorrected Ring event planes used in the symmetric subevent analysis at 200 GeV. The event plane correlation is also shown with and without the correction.

Fig. 6.15 shows the reconstructed v_1 with and without the reaction plane flattening. Even with the observed event plane structure, especially in the positive halves of the Octagon and Ring event planes, the directed flow is largely unchanged. The same is observed at the other energies.
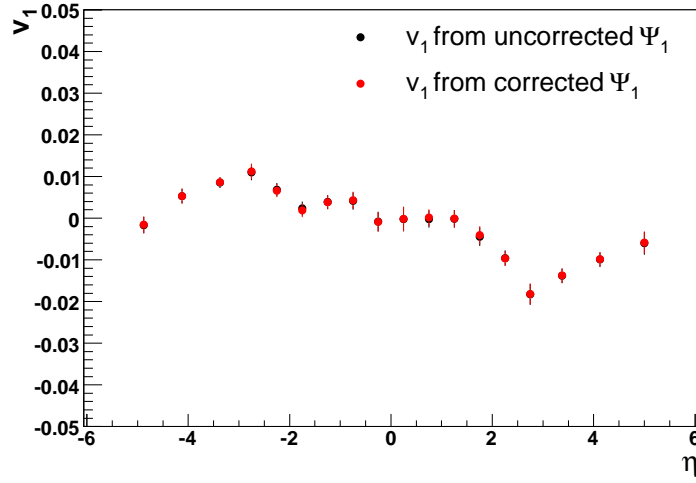
Figure 6.15: Directed flow at 200 GeV from the symmetric subevent analysis, measured with and without the event plane flattening algorithm.

6.6 Pseudorapidity Dependence of Directed Flow

Fig. 6.16 shows the pseudorapidity dependence of directed flow found with the symmetric subevent analysis at all energies [43]. The results are shown for all charged particles in the 0-40% centrality range. Note that the upper and lower panels are shown with different vertical scales. The vertical lines represent the 1σ statistical errors, and the boxes represent the 90% confidence level systematic errors. The average number of participants, $\langle N_{part} \rangle$, is also shown for each collision energy.

Historically, v_1 has been defined to be positive (negative) at high positive (negative) η where spectator matter is thought to dominate the signal [44]. We have preserved that convention here, although it is important to note that the spectator region falls outside of our acceptance at the higher energies. Consequently,
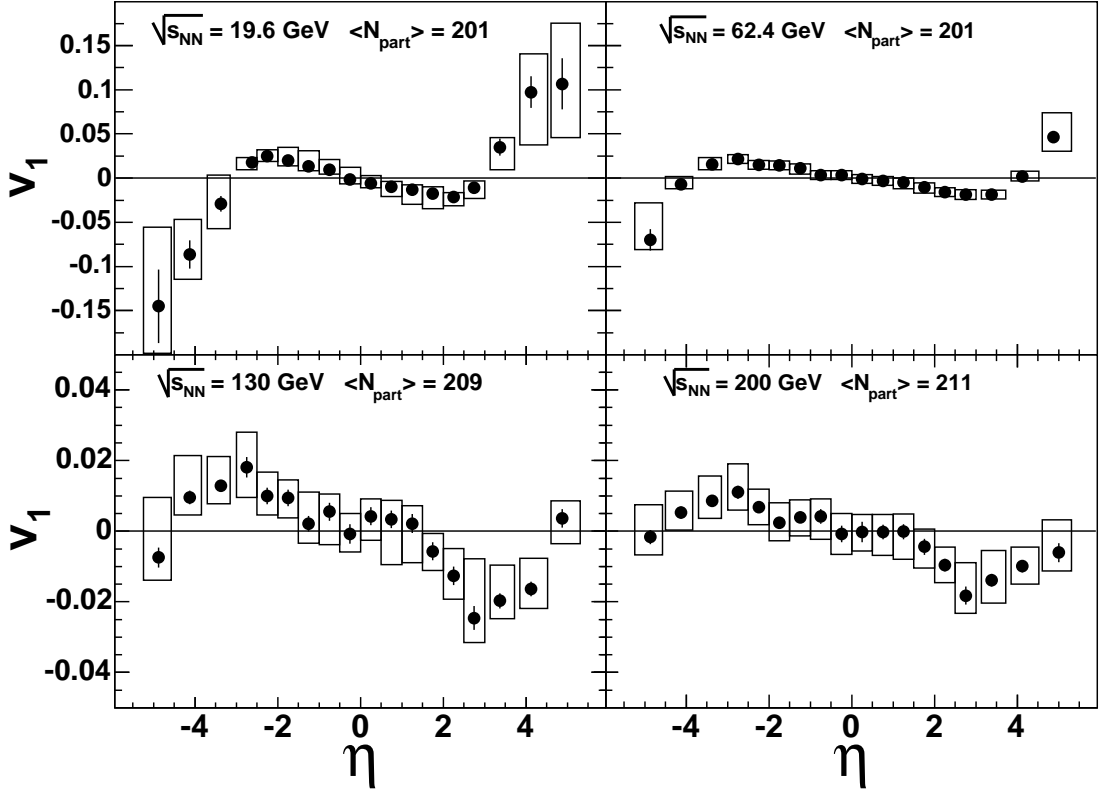
Figure 6.16: Directed flow of charged particles from the symmetric subevent analysis in Au+Au collisions as a function of η, averaged over centrality (0–40%), shown separately for four beam energies. Note the different vertical axis scales between the upper and lower panels. The boxes represent systematic uncertainties at 90% C.L., and $\langle N_{part} \rangle$ gives the average number of participants for each data sample.

the regions of η used to find the direction of Ψ_1 have varying spectator content as the collision energy increases. Thus, it is necessary to invert the sign of v_1 at 130 and 200 GeV in order to preserve the sign convention from the lower energies and make a direct comparison of the shapes as a function of energy, as shown in Fig. 6.16.

The results in Fig. 6.16 show the evolution of v_1 as the collision energy increases. All four energies exhibit a v_1 signal passing smoothly through zero at $\eta = 0$ as expected, indicating that there are no momentum conservation biases in

the data. The v_1 becomes more negative with η at each energy, until a "turnover"
point is reached, and the v_1 from both 19.6 and 62.4 GeV becomes positive at very
high pseudorapidities. This turnover at all energies and the large signal seen at
high $|\eta|$ for the lower energies are features uniquely observed by PHOBOS. These
effects may be due to protons and nuclear fragments taking over from pions as
the dominant contributors to the directed flow signal at high $|\eta|$.
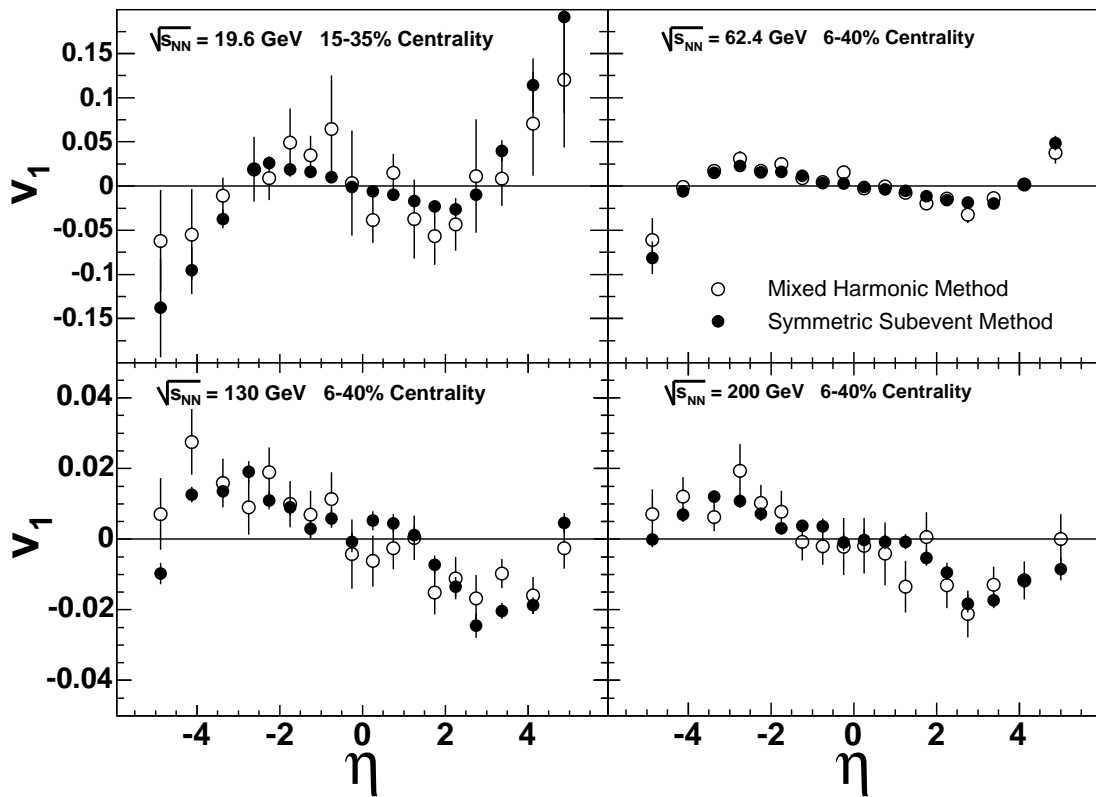
Figure 6.17: Measured directed flow as a function of η in Au+Au collisions using
the mixed harmonic event plane method (open points) overlaid with the standard
symmetric η subevent method (closed points). Note the different vertical axis
scales between the upper and lower panels. The centrality ranges shown for both
methods are those which give good mixed harmonic reaction plane sensitivity. For
clarity only the statistical errors are shown.

Fig. 6.17 shows the directed flow result found from the mixed harmonic analysis

as a function of pseudorapidity compared to the symmetric subevent result. The centrality ranges shown are those which give good mixed harmonic reaction plane sensitivity. The systematic error boxes from the symmetric subevent method have been left off for clarity. In both methods, the statistical errors exhibit a point-to-point correlation due to shared event plane and event plane resolution determination. The mixed harmonic method gives results which are consistent with the symmetric subevent method at 62.4, 130, and 200 GeV. At 19.6 GeV the mixed harmonic analysis results are in reasonable agreement with the symmetric subevent method, though the analyzing power of the mixed harmonic method is diminished at this energy due to the weak elliptic flow signal, as well as a very small event sample.

The agreement between these methods implies that the reaction plane determined by elliptic flow is the same as that determined by directed flow, within errors. This in turn means that the flow and the reaction plane that we see in Au+Au collisions is dominated by a global flow of the particles with minimal effects from "non-flow correlations". Furthermore, since the v_2 reaction plane is dominated by η near zero and v_1 by high $|\eta|$, this result indicates that the reaction plane orientation is consistent over the entire pseudorapidity range.

The results at 62.4 and 200 GeV are in qualitative agreement with results from STAR [24, 45]. Both experiments show $v_1 \sim 0$ for an extended region about midrapidity at 200 GeV, while $|v_1|$ increases as $|\eta|$ increases. Fig. 6.18 shows the STAR result [24] compared to PHOBOS at 200 GeV. The PHOBOS results are shown in the 10-50% centrality range to most closely match the STAR result shown in the 20-60% range. The PHOBOS trigger becomes inefficient beyond the 50% most central collisions.
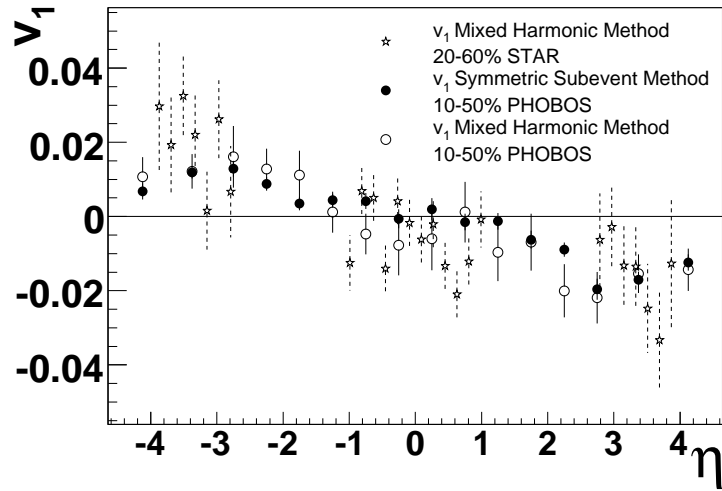
Figure 6.18: Directed flow results from PHOBOS compared to STAR at 200 GeV.

The PHOBOS and STAR comparison at 62.4 GeV is shown in Fig. 6.19. The STAR data is taken from [46] and averaged together over several centrality bins to show a single result in the 10-50% range. At 62.4 GeV, PHOBOS observes a turnover of the v_1 signal that occurs at smaller pseudorapidity than what is reported in the STAR data. This difference in the position of the turnover point may be due to a change in particle yields below STAR's transverse momentum acceptance cut. PHOBOS has the ability to record particles with transverse momenta down to about 35 MeV/c (140 MeV/c) for pions (protons) at $\eta = 0$ and 4 MeV/c (10 MeV/c) for $\eta \sim 4$–5, while STAR has a constant cutoff of $p_T \sim 150$ MeV/c.
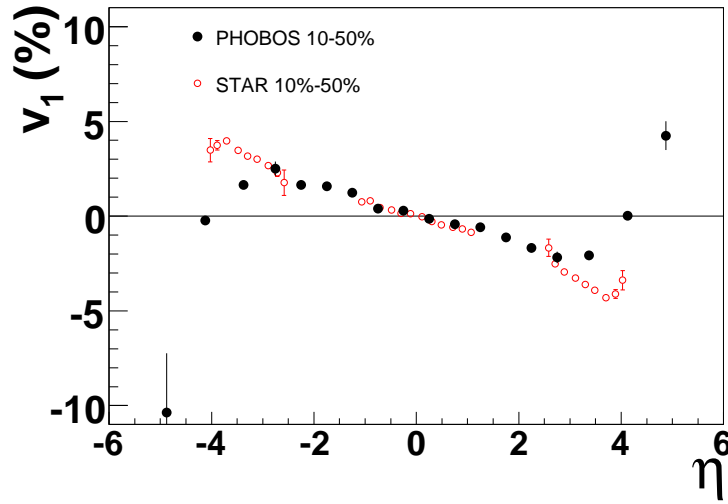
Figure 6.19: Directed flow results from the PHOBOS symmetric subevent method compared to STAR at 62.4 GeV.

6.7   Extended Longitudinal Scaling of Directed Flow

Fig. 6.20 shows the directed flow where data points from the positive and negative η regions have been averaged together and plotted as a function of $\eta' = |\eta| - y_{beam}$. Since the directed flow curves are odd functions, the negative η region is multiplied by -1 before the averaging is performed to avoid cancellation. Within the systematic errors (shown in Fig. 6.16), it appears that all curves scale throughout the entire region of η' overlap, showing that, within errors, the directed flow exhibits the longitudinal scaling behavior already observed in the elliptic flow and charged particle multiplicity [19]. This confirms and expands on an earlier observation of this scaling in the directed flow between RHIC and CERN's Super Proton Synchrotron results [45].
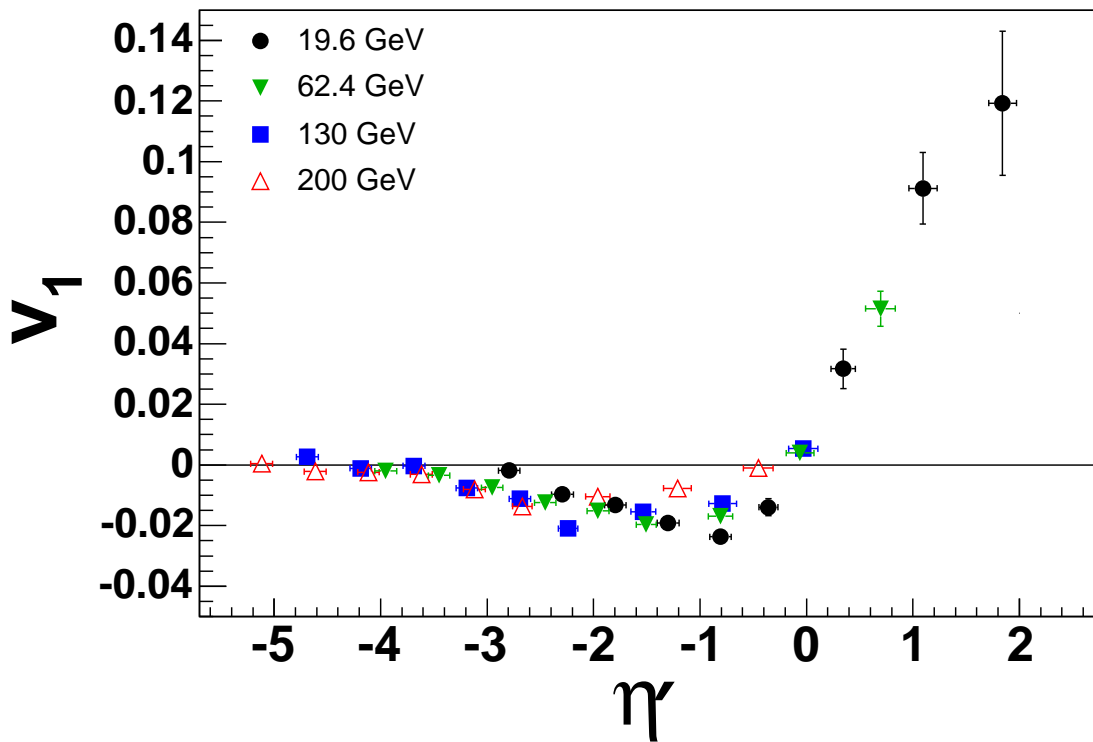
Figure 6.20: Directed flow, averaged over centrality (0–40%), as a function of $\eta' = |\eta| - y_{beam}$ for four beam energies. The error bars represent the 1σ statistical errors only.

Chapter 7

Summary and Conclusions

7.1 Flow Analysis Method

This thesis describes the design and implementation of a flow analysis for the PHOBOS experiment. This analysis improved upon previous flow analysis methods by using the entire PHOBOS multiplicity array over a collision vertex range that is centrally located in the PHOBOS detector where the bulk of the data is taken and is useful for other analyses. Azimuthal asymmetries in the detector sections used in the analysis are corrected such that they give no bias in the final results. The results shown are a systematic study of directed and elliptic flow as a function of pseudorapidity at all four major Au+Au collision energies using a single experiment and a single analysis, something that has not been done before at RHIC.

7.2 Elliptic Flow Results

The elliptic flow parameter, v_2, is shown as a function of pseudorapidity for Au+Au collisions at energies of $\sqrt{s_{NN}}$=19.6, 62.4, 130, and 200 GeV. The results at all four energies show a roughly triangular shape that peaks near midrapidity and quickly falls off as a function of pseudorapidity. The magnitude of v_2, when averaged in bins of pseudorapidity, grows with collision energy. The results from this analysis agree well with previous elliptic flow results at common collision energy and pseudorapidity coverage.

These results agree with previously obtained hydrodynamic calculations at midrapidity for the higher energies, indicating that the medium created behaves much like an ideal fluid. The falloff of v_2 with η is less understood by current calculations. The reason for the falloff is possibly due to non-ideal hydrodynamic effects such as incomplete thermalization and/or viscosity effects in the medium away from midrapidity [18]. However, more recent hydrodynamic calculations from the Buda-Lund model fit the reported data well, indicating that the "perfect fluid" may exist well beyond midrapidity and at lower energies [38].

The shape of v_2 evolves smoothly throughout the collision energies studied. By plotting v_2 as a function of $\eta - y_{beam}$, the elliptic flow results are approximately shifted into the rest frame of one of the colliding nuclei. The results show a remarkable extended longitudinal scaling over all energy ranges throughout the entire η range studied. This energy independence indicates no sharp changes in the character of the particle production over an order of magnitude in energy.

7.3   Directed Flow Results

Analogous directed flow results are shown as a function of pseudorapidity over the same collision energy range. These are the only directed flow measurements produced by PHOBOS to date. Two separate analysis methods are used which give good agreement. This indicates that the directed flow results are free of non-flow correlations. In addition, the results give qualitative agreement with STAR results at 62.4 and 200 GeV.

Directed flow shows a smooth change of shape over the collision energies, similar to what was observed in elliptic flow. At each energy, the v_1 signal is small at midrapidity and grows with increasing $|\eta|$. At very high $|\eta|$, a turnover of v_1 is observed, possibly due to protons dominating the flow signal in this range. In addition, extended longitudinal scaling of v_1 when plotted as a function of $\eta - y_{beam}$ is observed throughout the entire pseudorapidity range.

Bibliography

[1] D.H. Perkins, *Intro to High Energy Physics, 4th Ed.*, (Cambridge University Press, 2000).

[2] F. Karsch, Nucl. Phys. A **698**, 199c (2002).

[3] K. Rajagopal, Acta Phys.Polon. B**31**, 3021 (2000), [hep-ph/0009058].

[4] H. Hahn *et al.*, Nucl. Instrum. Meth. A **499**, 245 (2003).

[5] Pictures courtesy of Brookhaven National Laboratory's Relativistic Heavy Ion Collider Website: http://www.bnl.gov/RHIC/.

[6] B.B. Back *et al.*, Nucl. Phys. A **757**, 28 (2005).

[7] C. Adler *et al.*, Phys. Rev. Lett. **90**, 082302 (2003).

[8] T. Matsui and H. Satz, Phys. Lett. B **178**, 416 (1986).

[9] E. Andersen *et al.*, Phys. Lett. B **433**, 209 (1998).

[10] J. Adams *et al.*, Phys. Rev. C **68**, 044905 (2003).

[11] P.F. Kolb, U. Heinz (Eds.), Quark-Gluon Plasma 3, World Scientific, Singapore, 2003, [nucl-th/0305084].

[12] U. Heinz, in *Proceedings of the Extreme QCD Workshop*, University of Wales, 2005, [nucl-th/0512051].

[13] K.H. Ackermann *et al.*, Phys. Rev. Lett. **86**, 402 (2001).

[14] B.B. Back *et al.*, Phys. Rev. C **72**, 051901 (2005).

[15] B.B. Back *et al.*, Phys. Rev. Lett. **89**, 222301 (2002).

[16] T. Hirano, Phys. Rev. C **65**, 011901 (2001).

[17] P.F. Kolb and U. Heinz, J.Phys. G **30**, S1229 (2004), [nucl-th/0403044].

[18] T. Hirano, *et al.*, Phys. Lett. B **636**, 299 (2006), [nucl-th/0511046].

[19] B.B. Back *et al.*, Phys. Rev. Lett. **91**, 052303 (2003).

[20] A.M. Poskanzer and S.A. Voloshin, Phys. Rev. C **58**, 1671 (1998).

[21] P. Danielewicz and G. Odyniec, Phys. Lett. **157B**, 146 (1985).

[22] N. Borghini, P.M. Dinh, J.-Y. Ollitrault, A.M. Poskanzer and S.A. Voloshin, Phys. Rev. C **66**, 014901 (2002).

[23] N. Borghini, P.M. Dinh, and J.-Y. Ollitrault, Phys. Rev. C **66**, 014905 (2002).

[24] J. Adams *et al.*, Phys. Rev. C **72**, 014904 (2005).

[25] B.B. Back *et al.*, Nucl. Inst. Meth. A **499**, 603 (2003).

[26] R. Nouicer *et al.*, Nucl. Inst. Meth. A **461**, 143 (2001).

[27] B.B. Back *et al.*, Nucl. Phys. A **698**, 416c (2002).

[28] B.B. Back *et al.*, Phys. Rev. C **70**, 051901(R) (2004).

[29] R. Bindel *et al.*, Nucl. Inst. Meth. A **474**, 38 (2001).

[30] C. Adler *et al.*, Nucl. Inst. Meth. A **470**, 488 (2001).

[31] R. Bindel *et al.*, Nucl. Inst. Meth. A **488**, 94 (2002).

[32] B.B. Back *et al.*, Phys. Rev. C **70**, 021902R (2004).

[33] X. N. Wang and M. Gyulassy, Phys. Rev. D **44**, 35013516 (1991).

[34] GEANT 3.211, CERN Program Library.

[35] B.B. Back *et al.*, Phys. Rev. Lett. **87**, 102303 (2001).

[36] J. Barrette *et al.*, Phys. Rev. C **56**, 3254 (1997).

[37] B.B. Back *et al.*, Phys. Rev. Lett. **94**, 122303 (2005).

[38] M. Csanad, T. Csorgo, R.A. Lacey, B. Lorstad, in *Proceedings of the 22nd Winter Workshop on Nuclear Dynamics, La Jolla, California, 2006*, [nucl-th/0605044].

[39] J. Benecke, T.T. Chou, C-N. Yang, E. Yen, Phys. Rev. **188**, 2159 (1969).

[40] I.G. Bearden *et al.*, Phys. Rev. Lett. **88**, 202301 (2002).

[41] P. Walters and S. Manly, private communication.

[42] P. Kolb, in *Proceedings of the 17th Winter Workshop on Nuclear Dynamics, Park City, Utah, 2001*, Heavy Ion Phys. **15** 279-289 (2002).

[43] B.B. Back *et al.*, Phys. Rev. Lett. **97**, 012301 (2006).

[44] C. Alt *et al.*, Phys. Rev. C **68**, 034903 (2003).

[45] J. Adams *et al.*, Phys. Rev. C **73**, 034903 (2006).

[46] A.H. Tang for the STAR Collaboration, J.Phys. G **31** (2005) S35-S40